ON THE ACTIVE SITES AND MECHANISMS OF COBALT AND MANGANESE WATER OXIDATION CATALYSTS

By

PAUL F. SMITH

A Dissertation submitted to the

Graduate School-New Brunswick

Rutgers, The State University of New Jersey

In partial fulfillment of the requirements

For the degree of

Doctor of Philosophy

Graduate Program in Chemistry and Chemical Biology

Written under the direction of

G. Charles Dismukes

And approved by

_____

_____

_____

_____

New Brunswick, NJ

OCTOBER, 2015

ABSTRACT OF THE DISSERTATION

On the Active Sites and Mechanisms of Cobalt and Manganese Water Oxidation Catalysts

BY PAUL F. SMITH

Dissertation Director:

G. Charles Dismukes

The “holy grail” of renewable, sustainable energy is artificial replication of the only natural process capable of storing sun energy into chemical bonds: Photosynthesis. The oxidation of water to molecular O_2 is the thermodynamic bottleneck to this process. As such, viable catalysts for water oxidation are warranted. These materials ideally 1) are constructed of abundant elements (e.g., first row transition metals) and thus affordable, 2) operate efficiently and effectively with little applied bias (overpotential), and 3) maintain high activity for useful lifetimes.

In Chapter 1, Nature’s $CaMn_4O_5$ “heterocubane” catalyst is introduced. Principles of this structure which must translate into artificial catalysts are discussed: O-O bond formation, sacrificing oxidizing strength for long lifetimes, and effective storage of oxidizing equivalents via proton-coupled electron transfer (expanded in Chapter 5).

In Chapters 2-3, this thesis addresses the reactivity of cobalt based catalysts. Crystalline and amorphous cobalt oxides are well-known oxygen evolving catalysts, but up to three different mechanisms are proposed to occur on their surfaces. While the “cubane”

topology is stressed as biomimetic, these mechanisms commonly only feature a single metal active site- seemingly negating the cubane topology as necessary for catalysis. The results in these chapters- via studies on discrete Co_2O_2, Co_3O_3 and Co_4O_4 clusters- demonstrate that the cubane topology optimally stabilizes the Co^{4+} oxidation state via delocalization across all metal centers. This stored oxidizing equivalent reacts with terminally bound OH^- sites and facilitates oxidation fully to O_2.

In Chapter 4, this thesis addresses the reactivity of manganese-based catalysts. Paradoxical observations are known: Nature's effectiveness at utilizing Mn have predominantly translated into poor artificial Mn catalysts. While partially explained by the ~30 possible structures of Mn-oxides (many of which are minerals), promising results have correlated activity with stabilization of Mn^{3+}, as opposed to Mn^{4+}. The studies shown here rationalize these paradoxes by comparing structural polytypes of Mn^{3+}, clearly demonstrating that corner-sharing, labile Mn^{3+} centers capable of facile water binding correlate with catalytic activity as found in both layered and tunnel Mn oxides. Conversely, Mn of any oxidation state in strongly coupled structures are effective at storing charge but not transferring it to water.

Dedication

For Joe, Bill, Don, Shelli, Mike, and Tim

Acknowledgments

This document contains the science behind the following publications:

1. **Smith, P.F.**; Kaplan, C.; Sheats, J.E.; Robinson, D.M.; McCool, N.S.; Mezle, N.; Dismukes, G.C. "What determines catalyst functionality in molecular water oxidation? Dependence on ligand and metal nuclearity in cobalt clusters." *Inorganic Chemistry,* **2014**, 53, 2113-2121.
2. Carrell, T.G.; **Smith, P.F.**; Dennes, T.J.; Dismukes, G.C. "Entropy and Enthalpy Contributions to the Kinetics of Proton Coupled Electron Transfer to the $Mn_4O_4(O_2PPh_2)_6$ Cubane". *Phys. Chem. Chem. Phys.*, **2014**, 16(24), 11843-11847.
3. Deibert, B.; Zhang, J.; **Smith, P.F.**; Chapman, K.W.; Rangan, S.; Banerjee, D.; Tan, K.; Wang, H.; Pasquale, N.; Chen, F.; Lee, K.-B.; Dismukes, G.C.; Chabal, Y.J.; Li, J. "Surface and Structural Investigation of MnO_x Birnessite-type Water Oxidation Catalyst Formed Under Photocatalytic Conditions." Chem. Eur. J. **2015.** DOI: 10.1002/chem.201501930
4. **Smith, P.F.**; Deibert, B.J.; Kaushik, S.; Gardner, G.; Hwang, S.; Wang, H.; Al-Sharab, J.; Garfunkel, E.; Li, J.; Dismukes, G.C. "Water Oxidation Activity by Manganite (γ-MnOOH) Occurs Exclusively *via* Corner Sharing $Mn^{3+}O_6$ Octahedra" Submitted
5. **Smith, P.F.**; Hunt, L.; Laursen, A.B.; Sagar, V.; Kaushik, S.; Calvinho, K.U.D.; Marotta, G.; Mosconi, E.; De Angelis, F.; Dismukes, G.C. "Water Oxidation by [Co4O4]5+ Cubiums is initiated by OH^- Addition." Submitted.

G. Charles "Chuck" Dismukes singlehandedly brought me to Rutgers. His presentation of the research leading up to that performed in this document was appealing both in its broad reach and its significant aims. He heavily recruited me, and in the process, boosted my self-esteem significantly. For these efforts, and subsequently putting up with my shenanigans for many years thereafter with great patience, I am first and foremost grateful to have had him as a mentor.

Gerhard Swiegers singlehandedly brought me to Australia, and specifically, the University of Wollongong, in very similar fashion of putting a lot of blind faith into my capacity to perform science. He cowrote my proposal to have me visit, though I suspect it was more the ideas than the writing that sent me on the defining trip of my life. One does

not just learn science when abroad, and I owe a great deal of my coming-of-age story to him, as well. To my other Aussie colleagues- Jun Chen, Mark Romano, Adrian Gestos, Grant Mathieson, Rod Shepherd, Pawel Wagner, Michael Higgins, Gordon Wallace, Stephen Beirne, David Officer, and their AAS colleagues Meaghan O'Brien and Shannon Newham….thank you all for what was a great period of study for me.

Arguably my Ph.D.-holding in-lab mentors, John Sheats and Clyde Cady, deserve most of the credit for teaching me basic thought processes in chemistry. Over time, other people to fill this role expanded to include Yong Bok Go and Anders Laursen. I am also indebted to Nick McCool and David Robinson, whose research was so impactful it led to most of the projects reported in this document.

I am grateful to those I was able to mentor, for putting as much faith in me as I did my mentors. Chris Kaplan, Liam Hunt, Karin Calvinho and Shivam Kaushik were major contributors to my getting published.

As one can imagine, I owe a lot to the people who helped maintain my infrastructure. Clark electrode (and pretty much everything)- Gennady Ananyev, NMR- Nagarajan Murali, MIMS- Alexei Ermakov, QTOF- G. Kenchappa Kumaraswamy "Kumar", EPR- Viral Sagar. Andy DeZaio is tremendously appreciated for (at times) assembling our lab from scratch. I also wish to thank the Chemistry front office who made purchasing and logistics so seamless: Melissa Grunwerg, Karen Fowler, Allison Larkin, Lydia Haynes, Anne Doeffinger, and Ninette Steinberg, in particular.

I owe a lot to several peers whose conversations at multiple conferences motivated my science upon my return. James Blakemore, Rebecca Lindquist, Adam Weingarten,

Roman Kazantsev, Bradley Brennan and Andreas Bachmeier: I hope to run into you all again.

I owe many Italians some thanks, but none moreso than Filippo De Angelis, who without hesitation, worked through August to ensure that my thesis was made significantly stronger.

Equally, I owe Jingming Zhang, Ben Deibert, and Jing Li many thanks for bringing manganite- and fantastic solid-state chemistry- into this document.

And the only people who can really relate to my experience are those who lived exactly the same life as I- fellow graduate students who entered in 2010. Andrew Steffens and Graeme Gardner oversaw most of my life over the past few years, and I thank them for being more than just colleagues. Other graduate students I'd like to thank are Bin Liu, Anagha Krishnan, David Vinyard, Shinjae Hwang, Colin Gates, and Xiao Qian.

And finally, as always, love to my family- for they know few things about the science in this document, yet they are proud of all of it.

TABLE OF CONTENTS

List of Tables

List of Figures and Schemes

Chapter 1 How to Make a Better Oxygen Evolving Catalyst by Applying Nature's Design Principles of Catalysis

1.1 Abstract

The Photosystem II water oxidizing complex (PSII-WOC) is nature's blueprint for the photochemical center that powers the most widespread form of photosynthesis on Earth. Here we summarize the operating performance of PSII-WOCs that have led to the evolutionary success of their host organisms under diverse environmental conditions of solar flux, pH, temperature and humidity. We reconcile recent atomic structural models from Xray diffraction data with extensive prior spectroscopic and chemical data to arrive at a self-consistent picture of the intermediate oxidation states (S states). We compare this knowledge with that from studies of abiotic water oxidation catalysts to arrive at the most feasible mechanisms for biological water oxidation. This understanding in turn reveals where the next development steps are needed for improving catalysts and membranes for artificial photosynthetic processes.

1.2 Introduction

This chapter shows the most relevant information needed to understand the chemical basis of biological water oxidation and its implications for catalysing water oxidation in general. More specialized reviews of oxygenic photosynthesis are available[1–4]. In particular, this is structured to address the following subjects: 1) how PSII reaction centers are designed as a trade-off between photochemical charge separation vs. photoprotection by charge recombination (efficiency), 2) how PSII-WOCs activate water for concerted four-electron oxidation and O-O bond formation, and 3) transports products away from the active site to enable catalytic turnover under variable light flux (dynamic performance).

1.3 Discussion

Why target PSII-WOCs? Oxygenic photosynthetic organisms comprise the largest and most diverse group of photoautotrophs on Earth, encompassing simple unicellular prokaryotes and eukaryotes extending to complex multi-cellular higher plants. Evidence indicates they evolved *circa* 2.7 billion years ago from an anoyxgenic phototroph via modifications to a type 2 (iron-quinone) reaction center that acquired the unique ability to use water as electron donor (Photosystem II - water oxidation complex or PSII-WOC).This innovation enabled these pioneer organisms to occupy every ecological niches on Earth where water and light exist. The PSII reaction center protein core is remarkably conserved across all species of oxygenic photoautotrophs examined to date. No firm evidence for transitional PSII-WOCs yet exists that can or could have used other substrates for oxygen production[5].

The compositional and structural conservation of both the WOC catalytic core and PSII reaction center core proteins across diverse oxygenic phototrophs is stunningly unexpected. This invariance contrasts with the wide structural and compositional diversity among other ancient metallo-enzymes such as hydrogenases, nitrogenases, oxygenases, etc. It suggests a single preferred chemical pathway for water oxidation exists or survived in every ecological niche permissive of photoautotrophic life on Earth[6]. The consequences of this Darwinian process in combinatorial synthesis has important lessons for both natural and artificial photosynthesis.

The WOC incorporates an inorganic catalyst containing four electronically coupled Mn ions that accumulate four holes provided by four photochemical charge separation steps in the reaction center before O_2 is released[7,8]. Following these steps O_2 is released in a

concerted process with no free partially oxidized intermediates[9,10]. The net reaction, eq. 1a + 1b, produce a proton gradient and reduced plastoquinol (PQH_2), the initial energy carriers prior to downstream conversion to adenylate and pyridine nucleotide redox products.

$$2H_2O + 4h\nu(1.23V - 0.059*pH) \rightarrow O_2 + 4e^- + 4H^+_{lumen}, \qquad 1a.$$

$$2PQ + 4e^- + 4H^+_{stroma} \rightarrow 2PQH_2 \qquad 1b.$$

The maximum energy conversion yield of PSIIs *in vivo*, including both redox and pmf is 0.81 to 1.02 V per e^- for each red photon (680 nm) absorbed, or 44 to 56%. The average light-satured power output of various PSIIs (P_{avg}) = Energy x Flux = (0.8-1V nF) x (25-88 s^{-1}) = 19 MW mol^{-1}. The peak power of selected PSIIs could be 10X greater if the oxidation rate of the PQ pool were not rate limiting[1].

PSII reaction center photochemistry. At the core of PSII is the D1 subunit, which provides most of the ligating amino acid residues to the WOC, as well as binding pockets for P_{680}, pheophytin (Pheo), and the secondary PQ acceptor (Q_B). Figure 1.1 summarizes the energy of electrons and holes as a function of time in PSII. When excited to its lowest singlet state, P_{680}^* transfers an electron first to Pheophytin (Pheo) then to plastoquinone Q_A, all on a timescale of picoseconds. The resulting P_{680}^+ serves as a strong oxidant, and the origin of the electron which reduces P_{680}^+ guides the overall efficiency of water oxidation. For OER catalysis to go forward, reduction of P_{680}^+ must occur by D1-tyrosine 161 (Y_Z), which occurs in triphasic kinetic steps[11] between 20-50 ns and 30-35 µs, depending upon the redox state of the WOC (S state). The resulting Y_Z holds 50-60 mV thermodynamic driving force for reducing P_{680}^+. However if P_{680}^+ or Y_Z are reduced by

Pheo or Q_A^-, the hole is lost to recombination. Hence, Nature requires charge separation to last for anywhere between 30 µs (S_0-S_1) to 2 ms (O_2 release) in order for holes to be harvested on the same timescales as catalytic kinetics. During this time, there is overwhelming thermodynamic preference for reduction by these latter species (>1.2 V from Q_A^-). Nature slows recombination by imposing significant kinetic barriers in the form of longer distances, poorer orbital overlap and large reorganizational energies[4]. The upper limit for forward electron transfer kinetics for various PSIIs fall in the range 100-400 s^{-1} and is typically limited by the reoxidation rate of PQH_2 with one exception. The carbonate requiring cyanobacterium *Arthrospira maxima* is the fastest PSII-WOC in vivo. It possess both an alternative oxidase to remove electrons from the PQ pools and uses carbonate as proton acceptor to accelerate water oxidation[12].

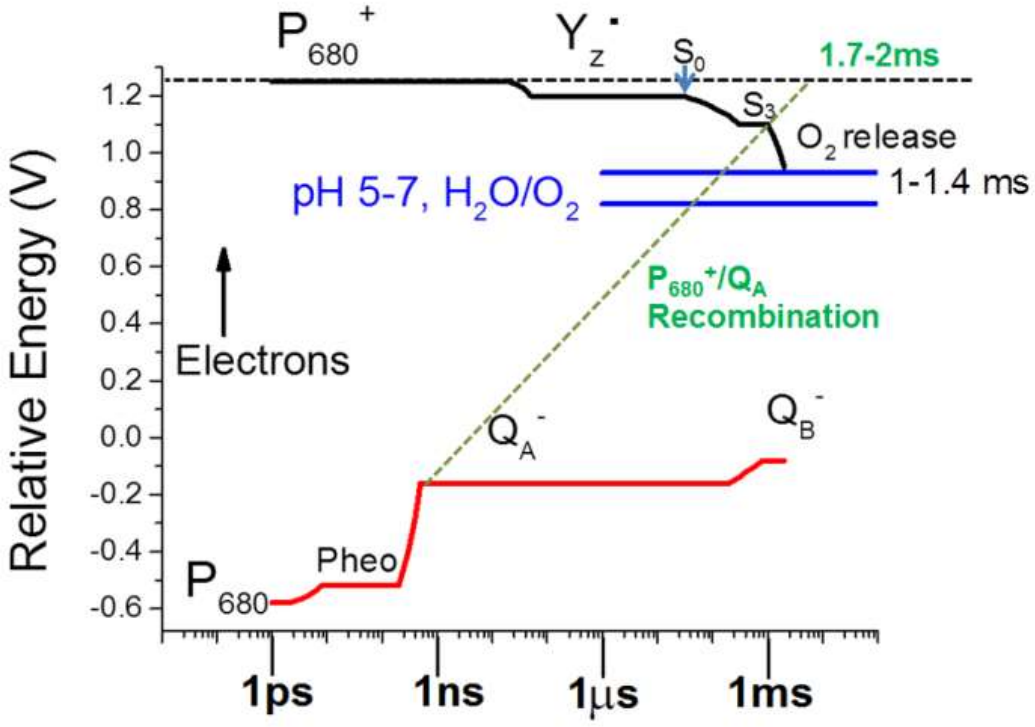

Figure 1.1. Energy and lifetimes of electron and holes in PSII-WOC.

PSII diversity and regulation. In order to thrive in diverse environmental conditions using a single type of reaction center and inorganic catalyst, oxygenic phototrophs evolved strategies to deal with wide environmental variations in light flux, pH, ionic strength, temperature, etc. Although the number and amino acid sequences of the extrinsic subunits of diverse PSII-WOCs vary substantially, the five protein subunits comprising the reaction center core (D1, D2, CP43, CP47, Cyt-b559αβ) are remarkably conserved (reviewed in ref[1]). The only significant variation observed to date in core proteins is in the D1 subunit of prokaryotes. At least four classes of D1 isoforms have been identified in cyanobacteria, compared to only one in eurkaryotes. The differential expression of these protein isoforms is controlled by transcriptional regulation of multiple *psbA* gene copies in response to environmental signals.

Light utilization efficiency is a trade-off between conversion and photoprotection: Differences in the amino acid sequences of the D1 isoforms control the efficiency of PSII specifically at very high and very low light intensities or under low-oxygen conditions. Two natural isoforms differing by 25 amino acids (7% AA) are expressed at low light (D1:LL) and high light (D1:HL), respectively (Figure 1.2). These offer either better primary photochemical quantum yield (hence better photoprotection) or better subsequent conversion efficiency into products (O_2, PQH_2 and ΔpH). The natural D1 isoforms can extend one or the other fitness criterion, as they act in opposition and thus create a trade-off in performance[13]. The isoforms result in growth rate performance benefits at high and low light intensities, respectively. This tuning feature has been further extended experimentally by constructing 7 conservative point mutations of the two natural D1 isoforms that partially convert D1:HL to D1:LL[14]. All strains reveal an inverse

correlation between performance metrics beneficial at LL vs HL intensities when plotted as a function of the PSII Quantum Yield (QY) (Figure 1.2). The latter reflects photochemical quenching of emission by charge separation in the reaction center and is measured most conveniently by Chl variable fluorescence quenching (F_V/F_M = QY). As the total charge separation QY is genetically varied in these D1 isoforms, there is a trade-off between excited state quenching by productive forward electron/hole transfer into the plastoquinone-pool/WOC, respectively, and quenching by charge recombination that provides protection against photoinactivation at high light intensity. This trade-off highlights Nature's capacity to "tune" the reaction center, depending on abundance of photons. The physicochemical mechanism used to achieve this tuning is based on adjusting the energy levels of the reduced intermediates[14], $Pheo^-$/Pheo and Q_A^-/Q_A.

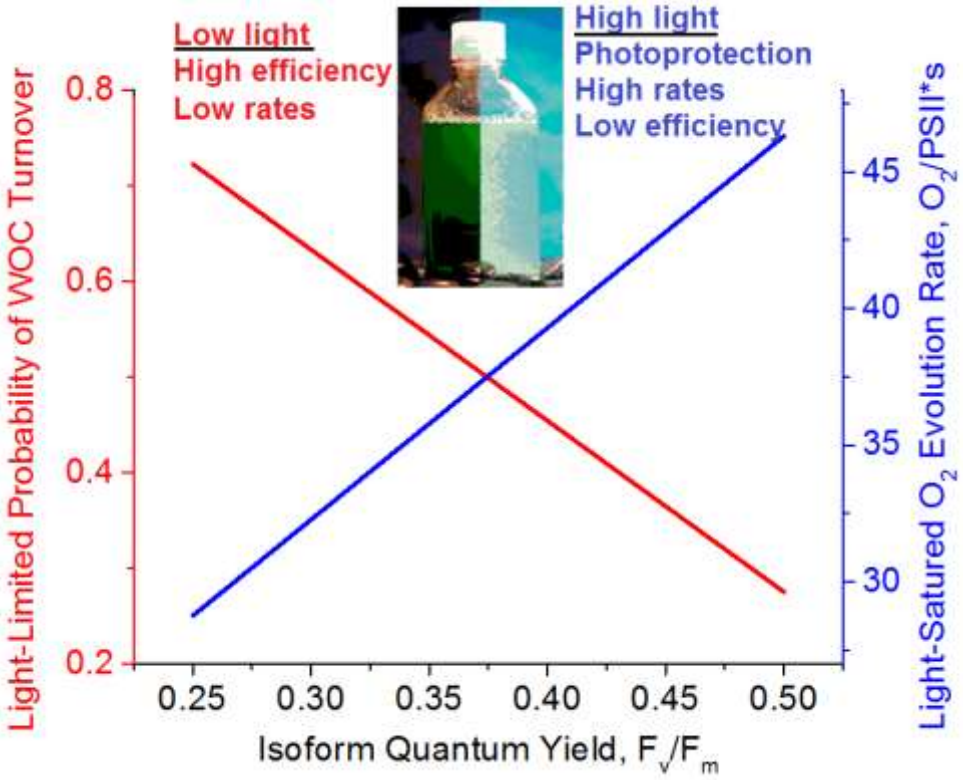

Figure 1.2. Regression equations from reference[14] correlating photochemical quantum yield of 9 isoforms of PSII to both the WOC efficiency under light limited conditions (black, R^2=0.789) and light saturated O_2 evolution rates (blue, R^2=0.859).

PSII's Catalyst. Uncatalyzed dissociation of the O-H bond of water requires an energy input of 119 kcal/mol; the amount of energy needed to break these O-H bonds is lowered both by activating water (via binding to metals) and releasing energy via the formation of two O-O bonds. The water oxidizing complex (WOC, Figure 1.3) to date represents nature's optimized strategy for catalysing this reaction. O_2 is released with kinetics on the order of 1-2 ms, indicative of a maximum turnover frequency (TOF) of 500-1000 O_2/s. This rate is remarkably fast when considering a modest 300 mV overpotential of Y_Z: no artificial catalyst is known to match 500/s TOF at 300 mV overpotential.

Atomic structures of PSII-WOCs obtained by EXAFS spectroscopy and later by high resolution crystallography of a cyanobacterial PSII-WOC have provided detailed structural information. The displayed structure refers to the most recent model from Xray diffraction using free electron laser to reduce radiation damage. This reveals a $CaMn_3O_4$ "heterocubane" that is oxo-bridged to a fourth Mn ion [15,16]. Our first discussion regarding this cluster concerns its capacity to bind water.

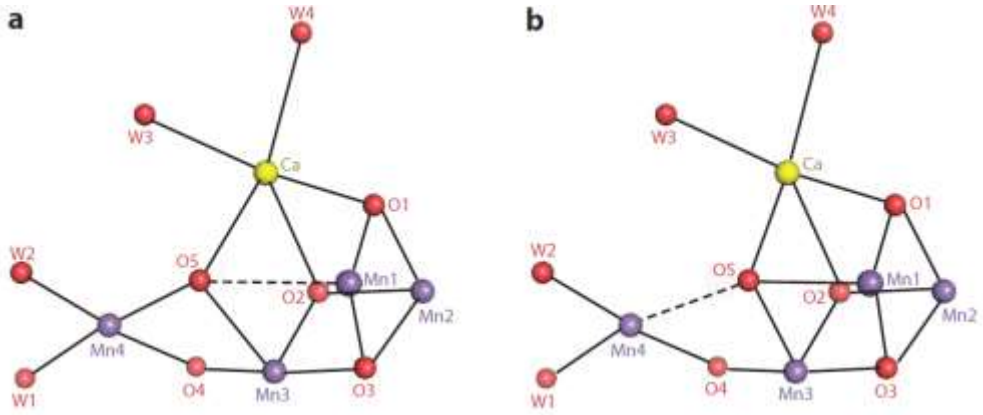

Figure 1.3. Structure of two tautomers of Nature's WOC. Courtesy ref[2]

Delivery of substrate water molecules- Terminal or bridging or both? Hillier and Wydrzynski demonstrated[17] that isotopically labeled water can bind into two oxo-sites of the WOC at various rates as a function of S state. Inspection of the WOC structure reveals that candidate sites include five *bridging* oxos vs. four *terminal* waters, of which only two are on a redox-active Mn. Significant discussion exists regarding which of these candidates are O_2 substrates. A conclusion by Hillier and Wydrzynski is that the two substrates consist of an Mn-O-Ca species and an Mn-OH_x species[1,17]. This has been supplemented by ^{17}O ENDOR experiments[18]. For the former species, our attention turns to μ_4-O5, which has unusual (nontetrahedral) geometry. The bond lengths to this bridge (ca. 2.2-2.7 Å) are significantly longer than all the other Mn-O bonds (1.8-2.1 Å). While the O atoms of the latter group retain a more usual distorted tetrahedral geometry, O5 is best geometrically characterized as an octahedral with two open coordination sites. As a consequence, the unhybridized character of the molecular orbitals on O5 differs vastly from O1, O2 and O3, which have sp^3 character. All the oxos in the heterocubane are noted for a minimization of π-bonding character to the metals, allowing for weaker and more flexible bonds. This is emphasized with the presence of calcium, which has nondirectional bonding to O1, O2 and O5. These features all point to a highly electron deficient (nearly neutral) O5 atom with atomic s + p valence orbitals occupied with both bonding and antibonding electrons from the Mn and Ca atoms resulting in long bonds and an unusual incomplete octahedral geometry. Our group[1] and others[19–21] support the proposal that O5 is an oxygen substrate.

Artificial mimics have shown a variety of results at introducing water molecules into bridging oxo sites between Mn centers. For instance, the $Mn_4O_4(O_2PPh_2)_6$ cubane

evolves two bridging oxos as O_2 either by heating or upon UV excitation in the gas phase[22]; these oxos can also be dehydrated as water molecules from sacrificial reductants[23–25], thus providing a pathway for converting between H_2O-O_2. In another system, Agapie and coworkers demonstrated the incorporation of water into a Mn^{III} tetramer, and oxygen atom transfer out of the resulting $Mn^{III}_2Mn^{IV}_2$ cubane[26]. These systems are likely dependent on Mn oxidation state. Brudvig and coworkers have measured rate constants $\leq 10^{-7}$ for exchange into bridging sites of all-Mn^{IV} tetramers- several orders of magnitude lower than those obtained (10^{-2}-10^{-4}) when mixed-valent $Mn^{III/IV}$ dimers were used[27]. Potentially, this provides information regarding the oxidation states achieved by nature's cubane, which must accommodate exchange of O5 with water up until it becomes "arrested" in the S_4 state[28].

Oxidation states of Mn in Natural Photosynthesis. Two possible sets of oxidation states can be ascribed to Nature's WOC: S_1 either has mean oxidation state of Mn^{3+} or $Mn^{3.5+}$. These possibilities are termed the Low Oxidation State (LOS) and High Oxidation State (HOS) paradigms, respectively. Extensive EPR, EXAFS, and XANES studies have been performed to determine which applies, for which we refer the reader to other literature[1,20,29–31]. Here, we will highlight the context now needed for either argument following publication of the 1.95 Å resolved S_1 structure free of radiation damage (XFEL structure)[16].

Density functional theory models of the PSII-WOC must have low energies and good agreements with experimental bond distances and EPR signals. New models have been created to assign either paradigm to the XFEL structure, which we note closely matches EXAFS data previously procured by the groups of Dau[32] and Yano[33]. The XFEL

structure thus represents the most precise depiction of the S1 state of the WOC to date from X-ray techniques. Models fitting the structure to the HOS have been published by the groups of Pantazis[34] and Batista[35], but both groups suggest that the XFEL structure must contain some S_0 population, hypothesized to originate from sample preparation. In contrast, Pace and coworkers have argued that the XFEL structure is pure S_1 which fits a LOS tautomer model to within 0.086 Å root mean square deviation[36]. It remains to be seen whether the collective EXAFS and XFEL data all include a significant S_0 population.

New data have also appeared from EPR techniques, following the discovery of a ^{55}Mn-ENDOR signal at 2.5 K which can assign multiple Mn^{III} in the S_2 state of *spinacia oleracia*[37]. This measurement indicates the LOS as correct, but was not reproduced in *T. elongatus*[34]. We refer the reader to a recent review of how to assign Mn hyperfine signals by Britt and coworkers[38].

We also refer the reader to photoassembly studies[39] which do not rely on spectroscopic comparison to model compounds in assigning oxidation state. Rather, these studies count the number of light flashes between addition of Mn^{2+} and O_2 evolution, and argue for the LOS paradigm.

Fortunately, several structural features exist independent of oxidation state assignment. We will discuss two: 1), the need for corner-sharing Mn^{3+} (on the dangler Mn), and 2) the accumulation of $3Mn^{4+}$ in the S_4 state. We will first discuss the accessibility of high Mn oxidation states, and in particular, oxidation states which run low risks of recombination.

WOC Thermodynamics Compared to Mn-oxides. In Figure 4, we overlay the known oxidizing potentials for P_{680}^{+}, Y_z^{ox}, and the WOC's S states onto the Mn Pourbaix diagram. Over the range of interest ($-0.5 \leq E_v \leq 1.75$, $0 \leq pH \leq 14$), Mn adopts two major oxidation states in solution (2+ and 7+), while solids range from all-Mn^{2+} to all-Mn^{4+}. Predominantly, processes for the WOC sit in the MnO_2 region of the diagram around the pKa of CO_2/HCO_3^-. As there is no evidence for peroxo intermediates during PSII water splitting, it is unsurprising that these processes sit below the thermodynamic threshold for peroxide oxidation/reduction.

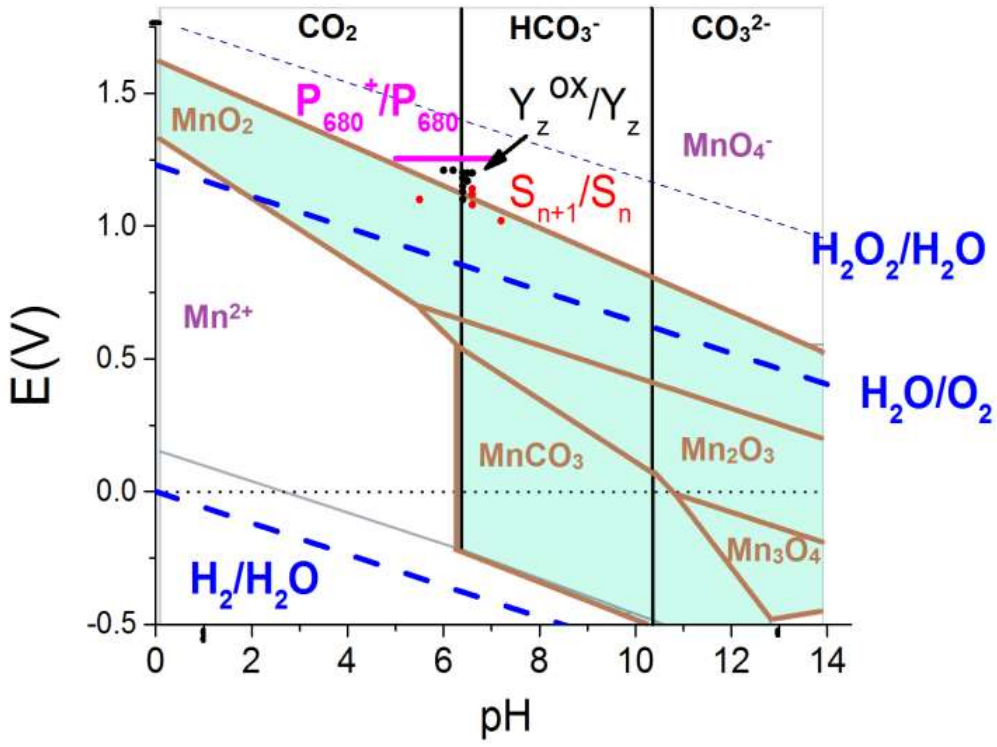

Figure 1.4. Thermodynamics for water oxidation overlaid on a Mn-Pourbaix diagram assuming 0.01 mol/kg Mn abundance and 100 uM abundance of Mn and C (Materials Project). All data for oxidation potentials for P_{680}^{+}, Y_z^{ox} and S_n states are taken from references[43–48].

The S states on the Pourbaix diagram align well with the region where Mn^{4+} could be expected to attain higher oxidation states. However, we note that the Pourbaix diagram does not reflect the presence of calcium, which plays several important roles in the WOC. One major function that it serves is preventing formation of a M_4O_4- homocubane subcluster during photoassembly. By doing this, Ca^{2+} reduces the extent of electronic delocalization between the Mn ions, thereby raising the cluster oxidation potential above that of the homocubane topology. This has been best demonstrated by Agapie and coworkers, who isolated the first known $CaMn_3O_4$ heterocubane, and showed that $3Mn^{IV}$ could be accessed at potentials >1V more moderate than the Mn_4O_4 derivative in the same ligand set (Table 1.1)[46].

Oxidation States	**E^0 vs. NHE (Ref[49])**
$Ca(Mn^{IV})_3O_4/Ca(Mn^{IV})_2(Mn^{III})O_4$	**-0.30 V**
$((Mn^{IV})_3(Mn^{III})O_4/(Mn^{IV})_2(Mn^{III})_2O_4$	**+0.93 V**
$((Mn^{IV})_2(Mn^{III})_2O_4/(Mn^{IV})(Mn^{III})_3O_4$	**-0.06 V**

Table 1.1. Calcium allows both $3Mn^{IV}$ and a mean oxidation level of 3.25 (per all metals) to be achieved at lower potentials than the all-Mn analog.

Calcium's location in the cluster is also of note, as it lies directly between Y_Z and the Mn subcluster. This juxtaposition and coordination via two water molecules to the phenolate-O atom of Y_Z provide a positive potential energy pathway that is important to creating the long range electronic coupling that ensures directional electron transfer between Mn and Y_Z (Figure 1.5). Calcium is only capable of being substituted by Strontium without complete loss of functionality.

One reason why this may be the case involves the comparable pK_A's of Ca and Sr. Agapie and coworkers have also shown a direct correlation between the oxidation potential of Mn-tetramers[47] and cubanes[48] as a function of the pKa of ligated redox inactive cations. This concept translates well into functional materials. Nam and coworkers have shown the reactivity and oxygen release of iron compounds is entirely modulated by redox inactive cations[49]. Catalytic systems (Ni-Fe[50], Co[51], and Mn[52] films) deposited on Au electrodes have higher activity than identical films on nonnoble metal supports, likely because gold tailors the oxidizing potentials accessible by these catalysts. Thus, among many reasons, the pK_A of calcium tailors the reactivity and electric potential of the WOC.

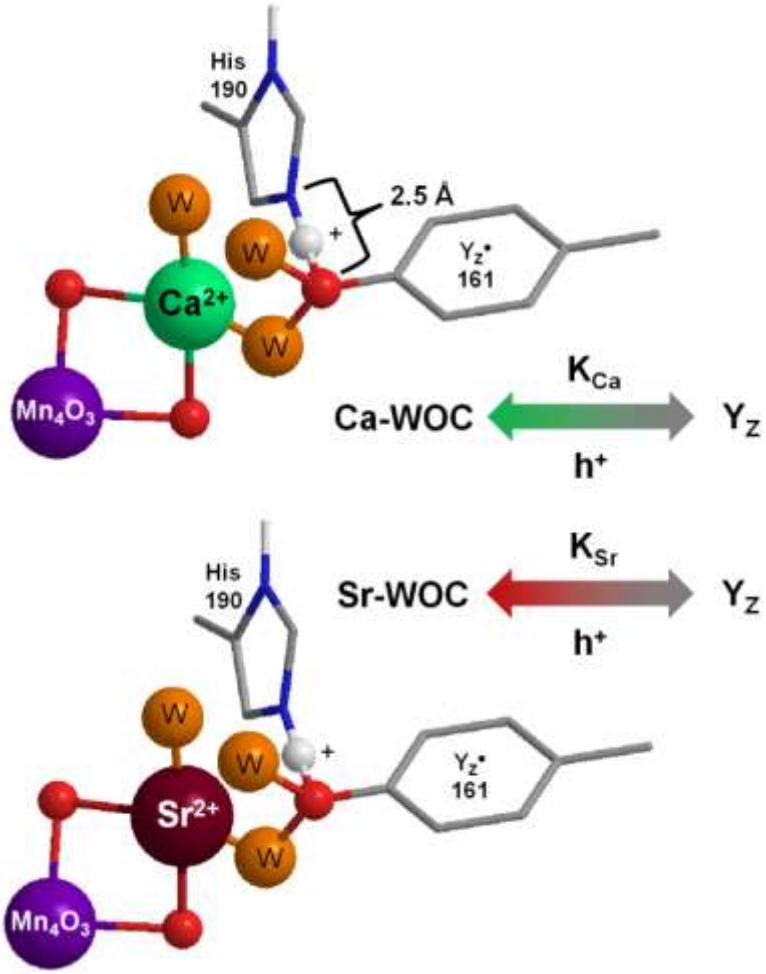

Figure 1.5. Depiction of the environment surrounding YZ in either Ca or Sr-substituted WOCs.

In absence of these redox inert cations, the MnO_2 stoichiometry inferred from the Pourbaix diagram in practice is realized through multiple polymorphs (geometries). Polymorphs of stoichiometry MnO_2 are widely regarded as stable, and as consequence, they are largely inactive as catalysts for water oxidation. This has been shown experimentally. Our lab tested eight crystalline polymorphs of manganese oxide for catalytic activity, including Mn_2O_3, Mn_3O_4, $LiMn_2O_4$, and five polymorphs of MnO_2 (α, β, δ, λ, R)[53]. It was found that the only active catalysts were Mn_2O_3 and Mn_3O_4, with low activity from λ-MnO_2. Activity was independent of surface area, particle morphology, and particle size, but was dependent on structure, since, for example, removing Mn_2O_3 "impurities" from β-MnO_2 resulted in complete inactivation of the sample. Our study complements a more apparent literature trend where manganese oxides of overall lower oxidation states (predominantly Mn^{3+}) are better artificial catalysts.[53–63] Many groups[56,64–67] have additionally reported activity from Mn_2O_3 and Mn_3O_4.

Why Mn^{3+}? One exception is glaring: $LiMn_2O_4$ with 50% Mn^{3+} is a poor catalyst in both electrochemical and photochemical assays[58,68]. This suggests that some Mn^{3+} structures are better suited at catalyzing water oxidation than others. In support of this assignment, we consider the birnessite family of water oxidation catalysts. Crystallographically defined birnessites having long range order exist in two structural archetypes: hexagonal (HexBir) and triclinic (TriBir). Both materials consist of sheets of edge-sharing MnO_6 octahedra separated by interstitial hydrated cations (Figure 1.6). TriBir contains Mn^{3+} octahedra within the MnO_2 sheets, while the reduced charge is compensated by interlayer spectator cations (here, K^+). In contrast, HexBir does not stabilize Mn^{3+} within sheets; instead these sites are vacancies with Mn^{3+} located above or below the vacancy in the

interlayer (or surface) bonded *via* corner-sharing bridges. Hexagonal birnessites are, in general, poorly crystalline and difficult to characterize due to the potential build-up of disordered vacancies.

Nonetheless, poorly crystalline birnessites correlate with higher catalytic activity in multiple studies,[69–73] in contrast to triclinic birnessites which are reported to exhibit low (or zero) activity for water oxidation.[53,69,74] This suggests a more viable role for corner-sharing Mn^{3+} than edge-sharing Mn^{3+} in designing artificial Mn-catalysts. Indeed, Dau and coworkers have directly correlated water oxidation activity to the presence of corner-sharing Mn octahedra in amorphous electrodeposited manganese oxides.[75]

As can be seen in the WOC (Figure 1.3B), the role of corner-sharing Mn is water binding and interaction (via tautomerization) with the cubane-based Mn. Indeed, the only Mn-bound terminal water ligands are located on the dangler, corner-shared species, while eight amino acid ligands collectively reside on the other Mn. This highlights Nature's strategy to prevent hydrolysis into poorly active Mn^{4+}-oxides. Further, it is noteworthy that supporters of *both* HOS and LOS paradigms have assigned the dangler as Mn^{3+} in the "closed cubane", spin=5/2 tautomer of the S2 state.[1,34]

Water binding by corner-sharing Mn has been observed experimentally. Studies of a crystalline hexagonal birnessite $K_{0.231}Mn^{3+}_{0.077}(Mn^{4+}_{0.885}\,\square_{0.115})O_2 \bullet 0.6\ H_2O$ ($\square$ represents lattice vacancies) by Lanson and coworkers assigned 0.24 (40%) of the formula water units as bound to interlayer (corner-shared) Mn^{3+}, despite being present as only 9% of the total Mn.[76]

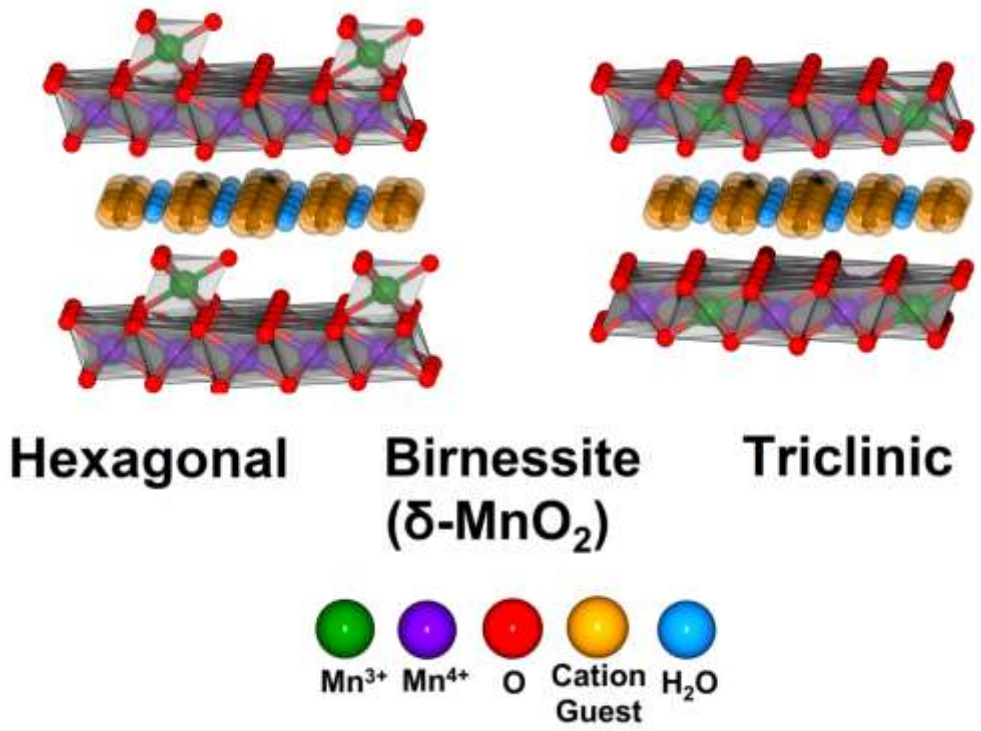

Figure 1.6. Difference between Hexagonal and Triclinic type birnessites.

Low light intensity: preventing recombination. The kinetic performance of the WOC catalytic cycle is not optimized for operation at full solar flux, but rather to achieve long lifetimes of the successive intermediates to suppress charge recombination (S_iQ_A- lifetimes). This latter property is indispensable for operation at low solar flux and explains why manganese is universally the only redox metal found in all PSII-WOCs. Charge recombination involves $Mn(III)Q_A$- which is slow owing to a large reorganization barrier for this oxidation state.

By contrast, other metals not found in WOCs such as Co(III) can form clusters and oxides based on $[Co_4O_4]^{4+}$ that are fast at water oxidation when operated at high rates of electron/hole removal. In particular, the $Co^{III}{}_4O_4$ cubane is the major structural feature in the unit cell of the known spinel OER catalyst Co_3O_4,[77] and several studies have offered it as a model and/or structure of catalytic amorphous cobalt oxide[78–82]. Our group[83] and others[84] have found that cubic $LiCoO_2$ (containing a Co_4O_4 unit cell) is an active water oxidation catalyst, while layered $LiCoO_2$ (containing a $LiCo_3O_4$ unit cell) is not. Collectively these highly active catalysts appear to converge significantly on this structure[85], and studies on molecular systems easily rationalize why.

The discrete cubanes $Co_4O_4(OAc)_4(py)_4$ (**1A**) and $[Co_4O_4(OAc)_2(bpy)_4]^{2+}$ (**1B**$^{2+}$), have been recently studied by many groups[81,82,86–88] (Figure 6). Both can be reversibly oxidized to their Co(IV)-containing analogs at modest potentials in water (1.25 V vs. NHE, >pH 4) and acetonitrile (<1.4 V vs. NHE)[89]. Via Hammett-type interaction, the ligand environment tailors the oxidation potential of the cubane's Co(IV)/(III) couple over a range of ca. 200 mV, which correlates with electron withdrawing (e.g., CN) or donating (e.g., OMe) substituents on the pyridine ligand[86,90]. But in contrast, "incomplete

cubanes" in the same ligand sets: dimers $[Co_2(OH)_2(OAc)_3(py)_4]^+$ and $[Co_2(OH)_2(OAc)_3(bpy)_2]^+$, as well as trimers $[Co_3O(OH)_2(OAc)_3(py)_5]^{2+}$ and $[Co_3O(OH)_3(OAc)_2(bpy)_3]^{2+}$ are not oxidized to Co(IV) up to 800 mV more positive[89]. Hence- while Co(IV) is accessible as a function of net charge (**1A** is neutral while $\mathbf{1B^{2+}}$ is dicationic) and ligand environment, Co-O structure plays a major contributor.

The lone electron pairs of each oxo bridge clearly contribute to stabilizing the Co(IV) oxidation state. This is evidenced by the increase in potential needed to obtain Co(IV) when these electrons form bonds to other cations. For instance, the Co(IV)/Co(III) potential increases in Nernstian behavior as a function of pH below the pKa (~3) of the oxo bridges (ref[81] and Figure 1.7). The octamer $Co_8O_4(O_2CPh)_{12}(solv)_4$- in which every μ-O bridge of a cubane is additionally coordinated to a "dangling" Co^{2+}- shows no oxidation *of any cobalt* up to 1.7 V vs. SCE (~1.95 V vs. NHE)[91]. Thus, it is clear that cobalt in some structures can more easily access the 4+ oxidation state than in others. We emphasize this may be a formal oxidation state assignment in these materials. Britt and coworkers have used EPR spectroscopy to describe $[Co_4O_4(OAc)_4(py)_4]^+$ ($\mathbf{1A^+}$) as having Co(IV) delocalized across the entire cubane core, with all metals and oxo bridges contributing to stabilizing the Co(IV) oxidation state[82,92]. This remains an important distinction because it is generally accepted that a single Co(IV) site is capable of catalysing OER: this conclusion is the result of reports of activity of cobalt monomers[93–97], in situ spectroscopic studies[98], and Tafel slope analyses[99]. Less considered, though, is how these catalysts are *designed* to access the Co(IV) oxidation state.

The molecular cubanes afford the unique opportunity to study charge recombination kinetics from a stable Co^{IV} cluster. While these kinetics may vary depending on the

acceptor, $\mathbf{1B^{3+}}$ has a second order rate constant of 300,000 M^{-1} s^{-1} for electron self-exchange[81]. This rate constant for recombination is several orders of magnitude higher than PSII (Table 1.2). Hence, cobalt's effectiveness at water oxidation in artificial systems is in one respect because formal Co(IV) is a powerful oxidant; moreso than Mn. On the other hand, there is little evidence of peroxo or superoxo intermediates during catalysis by nature's heterocubane, suggesting that PSII operates to *avoid* the generation of strong oxidants like Co^{IV} and free reactive oxygen species. In this line of thought it is evident that nature excels at catalysis by requiring very low overpotential.

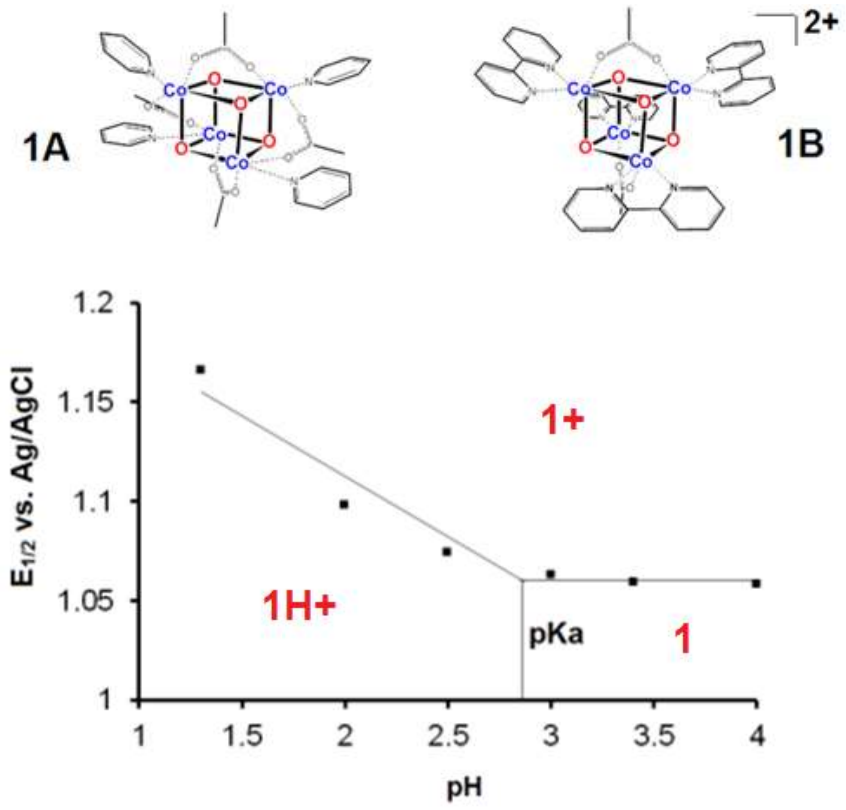

Figure 1.7. Depiction of cobalt cubanes **1A**, **1B**$^{2+}$, and redox accessibility to Co^{4+} as a function of pH.

Species	Recombination or Self-Exchange rate	Ref
PSII-WOC	< 500-1000 s^{-1}	[1]
$[Co^{IV}(Co^{III})_3O_4]^{3+}$ /$[Co^{III}{}_4O_4]^{2+}$	300,000 $(M*s)^{-1}$	[81]
Mn^{IV}(edta)/Mn^{III}(edta)	0.7 $(M*s)^{-1}$	[100]

Table 1.2. Recombination rates of Co(IV) vs. Mn(IV).

High light intensity: removal of products via Proton-Coupled Electron Transfer. Under high light conditions, where charge recombination does not compete, Nature must turn attention to timely removal of products from the reaction center. Most notably, the accumulation of product protons causes a lowering of local pH, and an increase in the required energy to split water. As one example, $Y_z^{\bullet}/Y_z$ oxidation occurs *only* when H^+ evolution is permitted; this reaction is blocked or reversed if protons derived from water oxidation accumulate[1]. Similar concepts extend to design of solar fuels architectures, as shown by Lewis and coworkers, who demonstrated that water splitting electrodes under steady state operation are exposed to highly acidic or alkaline conditions from product accumulation, even if the bulk electrolyte is buffered to neutral pH[101].

As seen in Figure 5, proton transfer from His_{190} plays an often overlooked yet critical function. This proton movement from His_{190} to $Y_Z^{\bullet}$ traps the electron and yields neutral Y_z-OH. This keeps the site of oxidation within the Mn4O5 subcluster, rather than on Y_z, where it is susceptible to recombination from the WOC or Q_A and Q_B[102]. The electron transfer network from the WOC to tyrosine thus runs first through Ca^{2+}/Sr^{2+} and subsequently the movement of H^+. This is indicative of an electrical potential gradient that facilitates forward electron transfer. Conversely, when the proton is not needed for this function, strong bonding to His_{190} prevents its release into the WOC core. The $Y_Z(H+)His_{190}$ "molecular diad" is analogous to a pn-diode, designed foremost to prevent reverse electron flow and keep the accumulated holes in the Mn_4O_5 subcluster where O_2 evolution can be catalyzed.

1.4 Conclusion

The reason for the activity of the aforementioned catalysts, and of the natural system, has been a source of extensive conjecture and discussion. Understanding the mechanism of artificial catalysts can lead to better understanding of the natural system, and vice versa, which leads to the development of better artificial photosynthetic systems. By no means are all the known artificial water oxidation catalysts composed in the same way, but it seems that the presence of general structural principles among active materials are often more than coincidental. These include weakly bonded oxos and long Mn-Mn distances as result of Jahn-Teller distortions, e_g orbital occupancy, and the cubane motif amongst first-row transition metals. The most obvious and least contested attribute of water oxidation catalysts is the ability to store oxidizing equivalents readily by distributing them over multiple centers. Many of the first row transition metals have access to multiple oxidation states but the redox potentials can vary substantially, thus bringing one metal to a highly oxidized form can be unstable and restrictive toward catalysis. PSII undergoes four sequential oxidations utilizing the same oxidant, P680, meaning a narrow potential window is necessary to oxidize all four manganese centers. Mechanistic pathways for dioxygen formation must also be considered, as redox active metal oxides are not always sufficient for catalysis. The capability for rearranging, breaking and forming bonds must also be a prerequisite for catalysis.

Overall, consideration of the relatively new high-resolution atomic structure of the WOC, combined with emerging reports of the WOC's oxidation states, the features of artificial catalysts and chemistry of structural mimics collectively continue to expand our

understanding of water oxidation catalysis by manganese. These findings both signify and encourage growth in this area for the future of this catalysis community.

1.5 Acknowledgment

We thank Ron Pace and David Vinyard for discussions. P.F.S. is grateful to NSF DGE0903675 for a fellowship. The authors declare no competing financial interests.

1.6 References

(1) Vinyard, D. J.; Ananyev, G. M.; Dismukes, G. C. Annu. Rev. Biochem. 2013, 82, 577–606.
(2) Shen, J.-R. Annu. Rev. Plant Biol. 2015, 66, 23–48.
(3) Cox, N.; Pantazis, D. A.; Neese, F.; Lubitz, W. Acc. Chem. Res. 2013, 46, 1588–1596.
(4) Renger, G. Biochim. Biophys. Acta - Bioenerg. 2012, 1817, 1164–1176.
(5) Nguyen, T. A.; Brescic, J.; Vinyard, D. J.; Chandrasekar, T.; Dismukes, G. C. Mol. Biol. Evol. 2012, 29 , 35–38.
(6) ANANYEV, G.; Dismukes, G. C. Photosynth. Res. 2005, 84, 355–365.
(7) Dismukes, G. C.; Siderer, Y. Proc. Natl. Acad. Sci. 1981, 78, 274–278.
(8) Dismukes, G. C.; Ferris, K.; Watnick, P. Photobiochem. Photobiophys. 1982, 3, 243–256.
(9) Kok, B.; Forbush, B.; McGloin, M. Photochem. Photobiol. 1970, 11, 457–475.
(10) Joliot, P.; Barbieri, G.; Chabaud, R. Photochem. Photobiol. 1969, 10, 309–329.
(11) Brettel, K.; Schlodder, E.; Witt, H. T. Biochim. Biophys. Acta - Bioenerg. 1984, 766, 403–415.
(12) Carrieri, D.; Ananyev, G.; Brown, T.; Dismukes, G. C. J. Inorg. Biochem. 2007, 101, 1865–1874.
(13) Vinyard, D. J.; Gimpel, J.; Ananyev, G. M.; Cornejo, M. A.; Golden, S. S.; Mayfield, S. P.; Dismukes, G. C. J Biol Chem 2013, 288, 5451–5462.
(14) Vinyard, D. J.; Gimpel, J.; Ananyev, G. M.; Mayfield, S. P.; Dismukes, G. C. J. Am. Chem. Soc. 2014, 136, 4048–4055.
(15) Umena, Y.; Kawakami, K.; Shen, J.-R.; Kamiya, N. Nature 2011, 473, 55–60.
(16) Suga, M.; Akita, F.; Hirata, K.; Ueno, G.; Murakami, H.; Nakajima, Y.; Shimizu, T.; Yamashita, K.; Yamamoto, M.; Ago, H.; Shen, J.-R. Nature 2015, 517, 99–103.
(17) Hillier, W.; Wydrzynski, T. Coord. Chem. Rev. 2008, 252, 306–317.
(18) Rapatskiy, L.; Cox, N.; Savitsky, A.; Ames, W. M.; Sander, J.; Nowaczyk, M. M.; Rögner, M.; Boussac, A.; Neese, F.; Messinger, J.; Lubitz, W. J. Am. Chem. Soc. 2012, 134, 16619–16634.
(19) Pérez Navarro, M.; Ames, W. M.; Nilsson, H.; Lohmiller, T.; Pantazis, D. a; Rapatskiy, L.; Nowaczyk, M. M.; Neese, F.; Boussac, A.; Messinger, J.; Lubitz, W.; Cox, N. Proc. Natl. Acad. Sci. 2013, 110 , 15561–15566.
(20) Cox, N.; Retegan, M.; Neese, F.; Pantazis, D. a.; Boussac, A.; Lubitz, W. Sci. 2014, 345 , 804–808.
(21) Siegbahn, P. E. M. Acc. Chem. Res. 2009, 42, 1871–1880.
(22) Ruettinger, W.; Yagi, M.; Wolf, K.; Bernasek, S.; Dismukes, G. C. J. Am. Chem. Soc. 2000, 122, 10353–10357.
(23) Carrell, T. G.; Smith, P. F.; Dennes, J.; Dismukes, G. C. Phys. Chem. Chem. Phys. 2014, 16, 11843–11847.
(24) Maneiro, M.; Ruettinger, W. F.; Bourles, E.; McLendon, G. L.; Dismukes, G. C. Proc. Natl. Acad. Sci. U. S. A. 2003, 100, 3707–3712.
(25) Ruettinger, W. F.; Ho, D. M.; Dismukes, G. C. Inorg. Chem. 1999, 38, 1036–1037.

(26) Kanady, J. S.; Mendoza-Cortes, J. L.; Tsui, E. Y.; Nielsen, R. J.; Goddard, W. A.; Agapie, T. J. Am. Chem. Soc. 2012, 135, 1073–1082.
(27) Tagore, R.; Chen; Crabtree, R. H.; Brudvig, G. W. J. Am. Chem. Soc. 2006, 128, 9457–9465.
(28) Nilsson, H.; Rappaport, F.; Boussac, A.; Messinger, J. Nat Commun 2014, 5.
(29) Lubitz, W.; Reijerse, E. J.; Messinger, J. Energy Environ. Sci. 2008, 1, 15–31.
(30) Pace, R. J.; Jin, L.; Stranger, R. Dalt. Trans. 2012, 41, 11145–11160.
(31) Glatzel, P.; Schroeder, H.; Pushkar, Y.; Boron, T.; Mukherjee, S.; Christou, G.; Pecoraro, V. L.; Messinger, J.; Yachandra, V. K.; Bergmann, U.; Yano, J. Inorg. Chem. 2013, 52, 5642–5644.
(32) Grundmeier, A.; Dau, H. Biochim. Biophys. Acta - Bioenerg. 2012, 1817, 88–105.
(33) Pushkar, Y.; Yano, J.; Glatzel, P.; Messinger, J.; Lewis, A.; Sauer, K.; Bergmann, U.; Yachandra, V. J. Biol. Chem. 2007, 282 , 7198–7208.
(34) Krewald, V.; Retegan, M.; Cox, N.; Messinger, J.; Lubitz, W.; DeBeer, S.; Neese, F.; Pantazis, D. a. Chem. Sci. 2015, 6, 1676–1695.
(35) Askerka, M.; Vinyard, D. J.; Wang, J.; Brudvig, G. W.; Batista, V. S. Biochemistry 2015, 54, 1713–1716.
(36) Petrie, S.; Pace, R. J.; Stranger, R. Angew. Chemie 2015, 127, 7226–7230.
(37) Jin, L.; Smith, P.; Noble, C. J.; Stranger, R.; Hanson, G. R.; Pace, R. J. Phys. Chem. Chem. Phys. 2014, 16, 7799–7812.
(38) Oyala, P.; Stich, T.; Britt, R. D. Photosynth. Res. 2015, 124, 7–18.
(39) Kolling, D. R. J.; Cox, N.; Ananyev, G. M.; Pace, R. J.; Dismukes, G. C. Biophys. J. 2012, 103, 313–322.
(40) Rappaport, F.; Guergova-Kuras, M.; Nixon, P. J.; Diner, B. A.; Lavergne, J. Biochemistry 2002, 41, 8518–8527.
(41) Rappaport, F.; Diner, B. A. Coord. Chem. Rev. 2008, 252, 259–272.
(42) Grabolle, M.; Dau, H. Biochim. Biophys. Acta - Bioenerg. 2005, 1708, 209–218.
(43) Ahlbrink, R.; Haumann, M.; Cherepanov, D.; Bögershausen, O.; Mulkidjanian, A.; Junge, W. Biochemistry 1998, 37, 1131–1142.
(44) Dau, H.; Haumann, M. Photosynth. Res. 2007, 92, 327–343.
(45) Dau, H.; Zaharieva, I. Acc. Chem. Res. 2009, 42, 1861–1870.
(46) Kanady, J. S.; Tsui, E. Y.; Day, M. W.; Agapie, T.; Tsiu, E. Y.; Day, M. W.; Agapie, T. Science (80-.). 2011, 333, 733–736.
(47) Tsui, E. Y.; Tran, R.; Yano, J.; Agapie, T. Nat Chem 2013, 5, 293–299.
(48) Tsui, E. Y.; Agapie, T. Proc. Natl. Acad. Sci. 2013, 110 , 10084–10088.
(49) Bang, S.; Lee, Y.-M.; Hong, S.; Cho, K.-B.; Nishida, Y.; Seo, M. S.; Sarangi, R.; Fukuzumi, S.; Nam, W. Nat Chem 2014, 6, 934–940.
(50) Trotochaud, L.; Young, S. L.; Ranney, J. K.; Boettcher, S. W. J. Am. Chem. Soc. 2014, 136, 6744–6753.
(51) Yeo, B. S.; Bell, A. T. J. Am. Chem. Soc. 2011, 133, 5587–5593.
(52) El-Deab, M. S.; Awad, M. I.; Mohammad, A. M.; Ohsaka, T. Electrochem. commun. 2007, 9, 2082–2087.
(53) Robinson, D. M.; Go, Y. B.; Mui, M.; Gardner, G.; Zhang, Z.; Mastrogiovanni, D.; Garfunkel, E.; Li, J.; Greenblatt, M.; Dismukes, G. C. J. Am. Chem. Soc. 2013, 135, 3494–3501.

(54) Yamaguchi, A.; Inuzuka, R.; Takashima, T.; Hayashi, T.; Hashimoto, K.; Nakamura, R. Nat Commun 2014, 5.
(55) Park, J.; Kim, H.; Jin, K.; Lee, B. J.; Park, Y.-S.; Kim, H.; Park, I.; Yang, K. D.; Jeong, H.-Y.; Kim, J.; Hong, K. T.; Jang, H. W.; Kang, K.; Nam, K. T. J. Am. Chem. Soc. 2014, 136, 4201–4211.
(56) Kuo, C.-H.; Mosa, I. M.; Poyraz, A. S.; Biswas, S.; El-Sawy, A. M.; Song, W.; Luo, Z.; Chen, S.-Y.; Rusling, J. F.; He, J.; Suib, S. L. ACS Catal. 2015, 1693–1699.
(57) Gorlin, Y.; Jaramillo, T. F. J. Am. Chem. Soc. 2010, 132, 13612–13614.
(58) Cady, C. W.; Gardner, G.; Maron, Z. O.; Retuerto, M.; Go, Y. B.; Segan, S.; Greenblatt, M.; Dismukes, G. C. ACS Catal. 2015, 3403–3410.
(59) Morita, M.; Iwakura, C.; Tamura, H. Electrochim. Acta 1979, 24, 357–362.
(60) Mattioli, G.; Zaharieva, I.; Dau, H.; Guidoni, L. J. Am. Chem. Soc. 2015, 137, 10254–10267.
(61) McKendry, I. G.; Kondaveeti, S. K.; Shumlas, S. L.; Strongin, D. R.; Zdilla, M. J. Dalt. Trans. 2015, 44, 12981–12984.
(62) Jeong, D.; Jin, K.; Jerng, S. E.; Seo, H.; Kim, D.; Nahm, S. H.; Kim, S. H.; Nam, K. T. ACS Catal. 2015, 5, 4624–4628.
(63) Takashima, T.; Hashimoto, K.; Nakamura, R. J. Am. Chem. Soc. 2012, 134, 1519–1527.
(64) Najafpour, M. M.; Ehrenberg, T.; Wiechen, M.; Kurz, P. Angew. Chemie Int. Ed. 2010, 49, 2233–2237.
(65) Jiao, F.; Frei, H. Chem. Commun. 2010, 46, 2920–2922.
(66) Ramírez, A.; Hillebrand, P.; Stellmach, D.; May, M. M.; Bogdanoff, P.; Fiechter, S. J. Phys. Chem. C 2014, 118, 14073–14081.
(67) Singh, A.; Roy Chowdhury, D.; Amritphale, S. S.; Chandra, N.; Singh, I. B. RSC Adv. 2015, 5, 24200–24204.
(68) Robinson, D. M.; Go, Y. B.; Greenblatt, M.; Dismukes, G. C. J. Am. Chem. Soc. 2010, 132, 11467–11469.
(69) Iyer, A.; Del-Pilar, J.; King'ondu, C. K.; Kissel, E.; Garces, H. F.; Huang, H.; El-Sawy, A. M.; Dutta, P. K.; Suib, S. L. J. Phys. Chem. C 2012, 160, 6474–6483.
(70) Wiechen, M.; Zaharieva, I.; Dau, H.; Kurz, P. Chem. Sci. 2012, 3, 2330–2339.
(71) Zaharieva, I.; Najafpour, M. M.; Wiechen, M.; Haumann, M.; Kurz, P.; Dau, H. Energy Environ. Sci. 2011, 4, 2400–2408.
(72) Menezes, P. W.; Indra, A.; Littlewood, P.; Schwarze, M.; Göbel, C.; Schomäcker, R.; Driess, M. ChemSusChem 2014, 7, 2202–2211.
(73) Deibert, B. J.; Zhang, J.; Smith, P. F.; Chapman, K. W.; Rangan, S.; Banerjee, D.; Tan, K.; Wang, H.; Pasquale, N.; Chen, F.; Lee, K.-B.; Dismukes, G. C.; Chabal, Y. J.; Li, J. Chem. Eur. J.
(74) Pokhrel, R.; Goetz, M. K.; Shaner, S. E.; Wu, X.; Stahl, S. S. J. Am. Chem. Soc. 2015, 137, 8384–8387.
(75) Zaharieva, I.; Chernev, P.; Risch, M.; Klingan, K.; Kohlhoff, M.; Fischer, A.; Dau, H. Energy Environ. Sci. 2012, 5, 7081–7089.
(76) Gaillot, A.-C.; Flot, D.; Drits, V. a.; Manceau, A.; Burghammer, M.; Lanson, B. Chem. Mater. 2003, 15, 4666–4678.
(77) Jiao, F.; Frei, H. Angew. Chemie-International Ed. 2009, 48, 1841–1844.

(78) Du, P.; Kokhan, O.; Chapman, K. W.; Chupas, P. J.; Tiede, D. M. J. Am. Chem. Soc. 2012, 134, 11096–11099.
(79) Risch, M.; Khare, V.; Zaharieva, I.; Gerencser, L.; Chernev, P.; Dau, H. J. Am. Chem. Soc 2009, 131, 6936–6937.
(80) Kanan, M. W.; Yano, J.; Surendranath, Y.; Dinca, M.; Yachandra, V. K.; Nocera, D. G.; Dincă, M.; Yachandra, V. K.; Nocera, D. G. J. Am. Chem. Soc 2010, 132, 13692–13701.
(81) Symes, M. D.; Surendranath, Y.; Lutterman, D. a.; Nocera, D. G. J. Am. Chem. Soc. 2011, 133, 5174–5177.
(82) McAlpin, J. G.; Stich, T. A.; Ohlin, C. A.; Surendranath, Y.; Nocera, D. G.; Casey, W. H.; Britt, R. D. J. Am. Chem. Soc. 2011, 133, 15444–15452.
(83) Gardner, G. P.; Go, Y. B.; Robinson, D. M.; Smith, P. F.; Hadermann, J.; Abakumov, A.; Greenblatt, M.; Dismukes, G. C. Angew. Chemie 2012, 124, 1648–1651.
(84) Maiyalagan, T.; Jarvis, K. A.; Therese, S.; Ferreira, P. J.; Manthiram, A. Nat Commun 2014, 5.
(85) Swiegers, G. F.; Clegg, J. K.; Stranger, R. Chem. Sci. 2011, 2, 2254–2262.
(86) Chakrabarty, R.; Bora, S. J.; Das, B. K. Inorg. Chem. 2007, 46, 9450–9462.
(87) La Ganga, G.; Puntoriero, F.; Campagna, S.; Bazzan, I.; Berardi, S.; Bonchio, M.; Sartorel, A.; Natali, M.; Scandola, F. Faraday Discuss. 2012, 155, 177.
(88) Dimitrou, K.; Folting, K.; Streib, W. E.; Christou, G. J. Chem. Soc. Chem. Commun. 1994, 838, 1385–1386.
(89) Smith, P. F.; Kaplan, C.; Sheats, J. E.; Robinson, D. M.; McCool, N. S.; Mezle, N.; Dismukes, G. C. Inorg. Chem. 2014, 53, 2113–2121.
(90) Berardi, S.; Natali, M.; Bazzan, I.; Puntoriero, F.; Sartorel, A.; Scandola, F.; Campagna, S.; Bonchio, M. J. Am. Chem. Soc. 2012, 134, 11104–11107.
(91) Dimitrou, K.; Sun, J.-S.; Folting, K.; Christou, G. Inorg. Chem. 1995, 34, 4160–4166.
(92) Stich, T.; Krzystek, J.; Mercardo, B. Q.; McAlpin, J. G.; Ohlin, C. A.; Olmstead, M. M.; Casey, W. H.; Britt, R. D. Polyhedron 2013, 64, 304–307.
(93) Wasylenko, D. J.; Ganesamoorthy, C.; Borau-Garcia, J.; Berlinguette, C. P. Chem. Commun. 2011, 47, 4249–4251.
(94) Pizzolato, E.; Natali, M.; Posocco, B.; Montellano Lopez, A.; Bazzan, I.; Di Valentin, M.; Galloni, P.; Conte, V.; Bonchio, M.; Scandola, F.; Sartorel, A.; Montellano López, A. Chem. Commun. 2013, 49, 9941–9943.
(95) Dogutan, D. K.; McGuire, R.; Nocera, D. G. J. Am. Chem. Soc. 2011, 133, 9178–9180.
(96) Wang, D.; Groves, J. T. Proc. Natl. Acad. Sci. 2013, 110 , 15579–15584.
(97) Ahn, H. S.; Yano, J.; Tilley, T. D. Energy Environ. Sci. 2013, 6, 3080–3087.
(98) Zhang, M.; de Respinis, M.; Frei, H. Nat Chem 2014, 6, 362–367.
(99) Gerken, J. B.; McAlpin, J. G.; Chen, J. Y. C.; Rigsby, M. L.; Casey, W. H.; Britt, R. D.; Stahl, S. S.; Rigsby, L.; Casey, W. H.; Britt, R. D.; Stahl, S. S. J. Am. Chem. Soc. 2011, 133, 14431–14442.
(100) Twigg, M. V. Mechanisms of Inorganic and Organometallic Reactions, Vol. 7.
(101) Jin, J.; Walczak, K.; Singh, M. R.; Karp, C.; Lewis, N.; Xiang, C. Energy Environ. Sci. 2014, 7, 3371–3380.
(102) Ioannidis, N.; Zahariou, G.; Petrouleas, V. Biochemistry 2008, 47, 6292–6300.

(103) McCrory, C. C. L.; Jung, S.; Peters, J. C.; Jaramillo, T. F. J. Am. Chem. Soc. 2013, 135, 16977–16987.
(104) McCrory, C. C. L.; Jung, S.; Ferrer, I. M.; Chatman, S. M.; Peters, J. C.; Jaramillo, T. F. J. Am. Chem. Soc. 2015, 137, 4347–4357.
(105) Vesborg, P. C. K.; Jaramillo, T. F. RSC Adv. 2012, 2, 7933.
(106) Stephens, I. E. L.; Bondarenko, A. S.; Gronbjerg, U.; Rossmeisl, J.; Chorkendorff, I. Energy Environ. Sci. 2012, 5, 6744–6762.
(107) Winther-Jensen, O.; Chatjaroenporn, K.; Winther-Jensen, B.; MacFarlane, D. R. Int. J. Hydrogen Energy 2012, 37, 8185–8189.

Chapter 2 What determines catalyst functionality in molecular water oxidation? Dependence on ligands and metal nuclearity in cobalt clusters.

2.1 Abstract

The metal-oxo M_4O_4 "cubane" topology is of special significance to the field of water oxidation as it represents the merging of bioinspired structural principles derived from natural photosynthesis with successful artificial catalysts known to date. Herein, we directly compare the rates of water oxidation/O_2 evolution catalyzed by six cobalt-oxo clusters including the Co_4O_4 cubanes, $Co_4O_4(OAc)_4(py)_4$ and $[Co_4O_4(OAc)_2(bpy)_4]^{2+}$, using the common $Ru(bpy)_3^{2+}/S_2O_8^{2-}$ photo-oxidant assay. At pH 8, the first-order rate constants for these cubanes differ by two fold, 0.030 and 0.015 s^{-1} respectively, reflecting the number of labile carboxylate sites that allow substrate water binding in a pre-equilibrium step before O_2 release. Kinetic results reveal a deprotonation step occurs on this pathway and that two electrons are removed before O_2 evolution occurs. The Co_4O_4 cubane core is shown to be the smallest catalytic unit for the intramolecular water oxidation pathway, as neither "incomplete cubane" trimers $[Co_3O(OH)_3(OAc)_2(bpy)_3]^{2+}$ and $[Co_3O(OH)_2(OAc)_3(py)_5]^{2+}$, nor "half cubane" dimers $[Co_2(OH)_2(OAc)_3(bpy)_2]^{+}$ and $[Co_2(OH)_2(OAc)_3(py)_4]^{+}$ were found capable of evolving O_2, despite having the same ligand sets as their cubane counterparts. Electrochemical studies reveal that oxidation of both cubanes to formally Co_4(3III,IV) (0.7 V vs Ag/AgCl) occurs readily, while neither dimers nor trimers are oxidized below 1.5V, pointing to appreciably greater charge delocalization in the $[Co_4O_4]^{5+}$ core. The origin of catalytic activity by Co_4O_4 cubanes illustrates three key features for water oxidation: 1) four one-electron redox metals, 2) efficient charge delocalization of the first oxidation step across the Co_4O_4 cluster,

allowing for stabilization of higher oxidizing equivalents, and 3) terminal coordination site for substrate aquo/oxo formation.

2.2 Introduction

Water oxidation catalysts based on first row transition ions are widely sought as replacements for costly noble metal catalysts. Numerous examples of molecular catalysts have been studied which operate over a wide range of cluster nuclearities, ligand functionalities, kinetic activities, and energy efficiencies[1–10]. Systematic studies within families of related catalysts have uncovered mechanistic complexities that have hampered understanding the factors that influence the rate of O_2 production and the catalyst lifetime.

As a reference point, oxygenic photosynthesis is capable of photooxidizing water far faster than any artificial catalyst based on first row transition metals. A recent analysis of the 1.9 Å resolved crystal structure of Photosystem II has shown that nature's universally conserved water oxidation catalyst is a $CaMn_4O_5$ cluster best described as a $CaMn_3O_4$ "heterocubane" with an O-Mn "dangler"[11]. As result, molecular tetrametallic clusters are increasingly reported as water oxidation catalysts[12]. Among these, the Co_4O_4 cubane structure has been found highly active among metal-oxide molecular catalysts[13–15]. It also serves as a simplified model for several heterogeneous metal oxide catalysts that contain cubical Co_4O_4 and Mn_4O_4 subunits, respectively[16]; notably the spinels Co_3O_4[17] and λ-MnO_2[18], cubic $LiCoO_2$[19] and studies which conjecture that cubic structures may form in the amorphous Co-Pi catalyst[20–22].

A particularly clear example of the benefit of the cubical topology for catalysis is seen among the two polymorphs of $LiCoO_2$ which differ by 100 fold in catalytic activity. Layered $LiCoO_2$ is made up of alternating layers of cobalt oxide comprised of "incomplete cubane" Co_3O_4 replicas, and lithium oxide layers. This material is catalytically inactive[19]. By contrast, active cubic $LiCoO_2$ is comprised of Co_4O_4 cubes stitched together by lithium ions at the corner oxos. This research inspired us to analyse clusters resembling fractions of the Co_4O_4 cubane to determine the required Co nuclearity and other properties needed for catalysis.

In this work we examine the influence of cluster nuclearity and ligand type on the kinetics of water oxidation among the six cobalt clusters depicted in Scheme 2.1. These compounds represent the gradual building of the M_4O_4 cubical core of interest *within the same ligand sets* (acetate and either pyridine or bipyridine). These clusters include two cubanes: $Co_4O_4(OAc)_4(py)_4$ (**1A**) and $[Co_4O_4(bpy)_4(OAc)_2]^{2+}$ (**1B**), two "half-cubane" dimers $[Co_2(OH)_2(OAc)_3(py)_4]^+$ (**2A**) and $[Co_2(OH)_2(OAc)_3(bpy)_2]^+$ (**2B**), and two "incomplete cubane" trimers $[Co_3O(OH)_2(OAc)_3(py)_5]^{2+}$ (**3A**) and $[Co_3O(OH)_3(OAc)_2(bpy)_3]^{2+}$ (**3B**). Table 2.1 lists the Co-Co, Co-O and estimated O-O bond distances for each of these materials based on previous single crystal X-ray diffraction studies[23–25]. All bond lengths are remarkably conserved throughout these clusters, indicating no major structural changes apart from nuclearity per cluster. We report that there is a clear correlation between cluster nuclearity, ligand lability and catalytic activity among these materials. Specifically, both cubanes **1A** and **1B** are active catalysts for oxygen evolution, differing in specific rates according to the number of labile carboxylate ligands. By contrast, the lower nuclearity clusters are inactive catalysts.

Trimer **3A** and dimer **2A** possessing pyridine ligands undergo ligand dissociation that triggers rearrangement to cobalt-oxo oligomers that are active catalysts. These results have significant implications towards understanding the molecular basis by which other reported cobalt complexes may oxidize water.

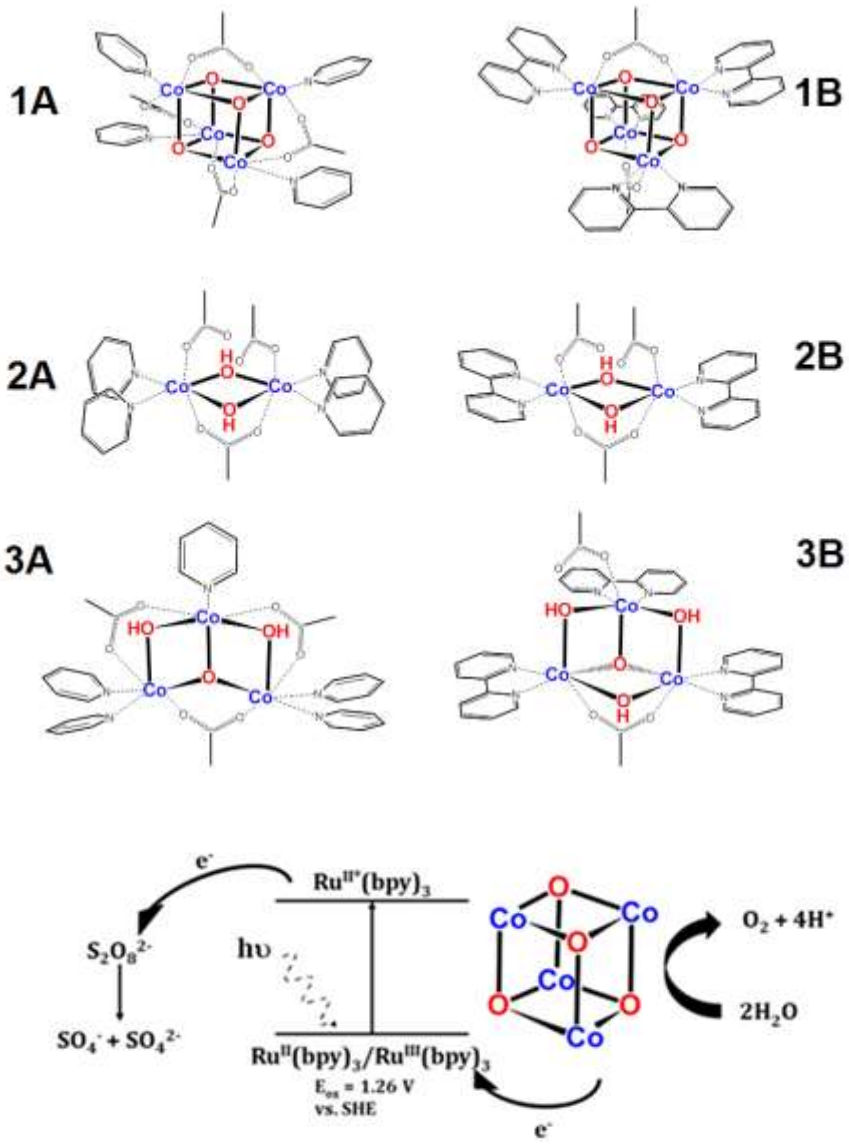

Scheme 2.1. Compounds and photoassay used.

Cluster	O-O distance[i]	Range of Co-O distances, Å	Range of Co-Co Distances, Å
1A	2.56	1.860-1.872	2.696-2.824
1B	n/a	1.863-1.895	2.663-2.850
2A	2.50	1.885-1.893	2.811
2B	2.56	1.883-1.901	2.793
3A	2.49	1.862-1.906	2.780-2.791[ii]
3B	2.65	1.880-1.919	2.717-2.874

Table 2.1. Selected atomic distances of molecular Cobalt compounds from Xray diffraction[23-25].

i) Estimated, this work.

ii) Co-Co not bridged by OH^- is excluded.

2.3 Experimental

Methods and Instruments. All solvents and reagents were reagent grade, purchased commercially and used without further purification. UV-Vis spectra were recorded on a HP 8452A Diode Array spectrophotometer. ESI-MS data were recorded on a Finnigan LCQ-DUO Mass Spectrometer. NMR data were recorded with a 400 MHz Varian VNMR; spectra in D_2O where indicated are referenced to an internal TMS standard. Cyclic voltammetry was collected on a CH Instruments Electrochemical Workstation using a Pt disc working electrode, Pt mesh counter electrode, Ag/AgCl reference, and a 100 mV/s scan rate.

$Co_4O_4(py)_4(OAc)_4$, **1A.** Synthesis and characterization have been previously described[13,24].

$Co_4O_4(bpy)_4(OAc)_2(ClO_4)_2$, 1B. Synthesis was adapted from ref[26] by reacting $[Co_2(OH)_2(OAc)_3(bpy)_2]ClO_4$ (0.16 g) with Li_2O_2 (0.046 g) in DMSO (15 mL) for 3 days at 70°C. After filtering, $CHCl_3$ (50 mL) was added to the filtrate and a brown solid was collected after >24 h of refrigeration. As prepared, we regularly observed sideproduct LiOAc and residual DMSO by ^{1}H NMR. A pure product is obtained, with slight loss of yield, by rigorous washing with water. ESI-MS: 521 (**$1B^{2+}$**), 463, 436, 367, 275. ^{1}H-NMR (DMSO): 8.8 (d, 8H), 8.4 (d, 8H), 8.2 (t, 8H), 7.2 (t, 8H), 0.8 (s, 6H). UV-Vis: 420 (br), see ref[27]. $E_{1/2}$ (CH_3CN)= 0.69 V vs. Fc^+/Fc, see ref[28].

$[Co_2(OH)_2(OAc)_3(py)_4]PF_6$, 2A and **$[Co_3O(OH)_2(OAc)_3(py)_5](PF_6)_2$, 3A.** Synthesis was taken from ref[25] by adding 35% peracetic acid (7.4ml) dropwise to $Co(OAc)_2$ (6.0g), pyridine (4.2ml), and glacial acetic acid (10ml) in H_2O (90ml). The mixture was

then heated to reflux for ten minutes, after which the heat was removed, and NH_4PF_6 (2.6g) in H_2O (20ml) was added. The solution was then cooled to room temperature and chilled in an ice bath. A solid was collected by filtration and washed with H_2O. Addition of methylene chloride (50ml) dissolves **2A** and leaves behind solid **3A.** Layering the dichloromethane layer with pentane (100 mL) overnight causes **2A** to crash out. Our characterization matches the original data provided in ref[25].

2A: ^{1}H-NMR (CD_3CN) δ= 8.3 (d, 8H), 8.05 (t, 4H), 7.55 (t, 8H), 7.3 (s, 2H), 2.3 (s, 3H), 2.05 (s, 6H). ESI-MS: 645 (**2A**$^+$), 566 (**2A**$^+$-py), 505 (**2A**$^+$-py-OAc), 426, 388, 348.

3A: ^{1}H-NMR (CD_3CN) δ= 8.85 (d, 2H) 8.4 (d, 4H), 8.1 (m, 3H), 7.9 (d, 4H), 7.7 (m,4H), 7.5 (t, 4H), 7.1 (t, 4H) 5.5 (s, 2H), 2.55 (s, 3H), 2.25 (s, 6H). As discussed in ref [25], ESI-MS for this cluster does not give interpretable signals.

$Co_2(OH)_2(OAc)_3(bpy)_2(ClO_4)$, **2B.** Synthesis was adapted from ref[26] by adding H_2O_2 (2.6mL, 35%) dropwise to $Co(OAc)_2$ (2.5g) and bipyridine (1.5g) in 20mL H_2O/60mL methanol. The mixture was then heated to 50°C for 30 minutes after which THF (80ml) and $LiClO_4$ (1.06g in 5ml H_2O) were added. The solution was heated at 50°C for 48 hours, cooled and finally filtered. The resulting solid was then washed with warm THF/H_2O (4:1) and dried at 100°C for 1 hour. ESI-MS: 641 (**2B**$^+$), 581 (**2B**-OAc), 521 (**2B**-2OAc). ^{1}H-NMR (DMSO): δ=9.7 (d, 4H), 8.8 (d, 4H), 8.5 (t, 4H), 8.1 (t, 4H), 7.5 (s, 2H), 1.5 (s, 6H), 1.4 (s, 3H).

$Co_3O(OH)_3(OAc)_2(bpy)_3(ClO_4)_2$, **3B.** Synthesis was adapted from ref[26] by adding H_2O_2 (6 mL, 35%) dropwise to a mixture of $Co(OAc)_2$ (1.3g), bipyridine (0.5g) in 100 mL of 6:1 EtOH/H_2O. $LiClO_4$ (1.2g) was then added. After 4 hours of stirring at room

temperature, a solid was collected by filtration. The product was then washed with ethanol and water and dried at 100°C for 2 hours. ESI-MS: 928 (**3B**ClO_4^+), 868 (**3B**ClO_4^+-OAc), 415 (**3B**$^{2+}$), several peaks of **2B** were visible. ^{1}H-NMR (CD_3CN): 1.4 (s, 3H), 1.3 (s, 3H).

Clark Electrode Procedure

A Clark type oxygen electrode (Hansatek Ltd) was used to obtain oxygen evolution data, and calibrated daily using deoxygenated and oxygen saturated atmospheric solutions. The temperature is controlled at 20°C for all experiments. The assay is loaded into a 2 mL temperature controlled Teflon-lined reaction chamber and illuminated with four LED lamps. For tests of **1A** and **1B,** photooxidation experiments consist of 1 mM $Ru(bpy)_3Cl_2$ and 5 mM $Na_2S_2O_8$ in 0.05 M sodium borate buffer adjusted to pH 8 with 2 M HNO_3.

For our tests of **2A, 2B, 3A,** and **3B,** we utilized the conditions as described in reference[13] . The presence of a lagtime before O_2 evolution is highly indicative of decomposition under these conditions, most notably the choice of pH 7.

Crystal structure Co-O distances and O-Co-O angles for **2A** and **3A** were taken from reference[25] ; **2B** and **3B** from reference[26]. Structures are assumed to be planar. The diagram below extends to the trimers by using the μ_3-O as one oxo, and one of the μ_2-OH as the other. The law of cosines enables calculation of the O-O distance based on the equation: $Z^2 = x^2 + y^2 - 2xy\cos(\Theta)$.

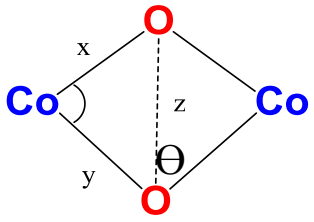

2.4Results

There are several reports of homogeneous water oxidation by **1A**, using the widely adopted photoassay depicted in Scheme 2.1[13–15]. In light of these reports, **1B** became an interesting candidate to study because the $Co_4O_4^{4+}$ core structure is conserved, but the nature of the coordinating ligands is different. The clusters also differ in charge: **1A** is neutral as isolated, while **1B** is dicationic. To our knowledge, **1B** has not been studied for water oxidation catalysis.

We prepared **1B** as a perchlorate salt according to the literature method[23]. Composition, structure and purity were established by ^{1}H-NMR, ESI-MS, cyclic voltammetry (CV) and UV-Vis (Figures 2.1-2.4). Figure 5 shows the resulting O_2 evolution traces when **1A** and **1B** are used as catalysts with the photoassay of Scheme 2.1 (pH 8, 0.05 M borate buffer, 1 mM Ru^{2+}, 5 mM persulfate) and dissolved O_2 was monitored by a Clark-type electrode. The amount of O_2 detected exceeded the oxygen content of **1B** at all concentrations measured, indicating that its generation is catalytic in nature and not due to stoichiometric decomposition. This conclusion is further supported by the absence of O_2 production in the control lacking either cubane (Figure 2.5).

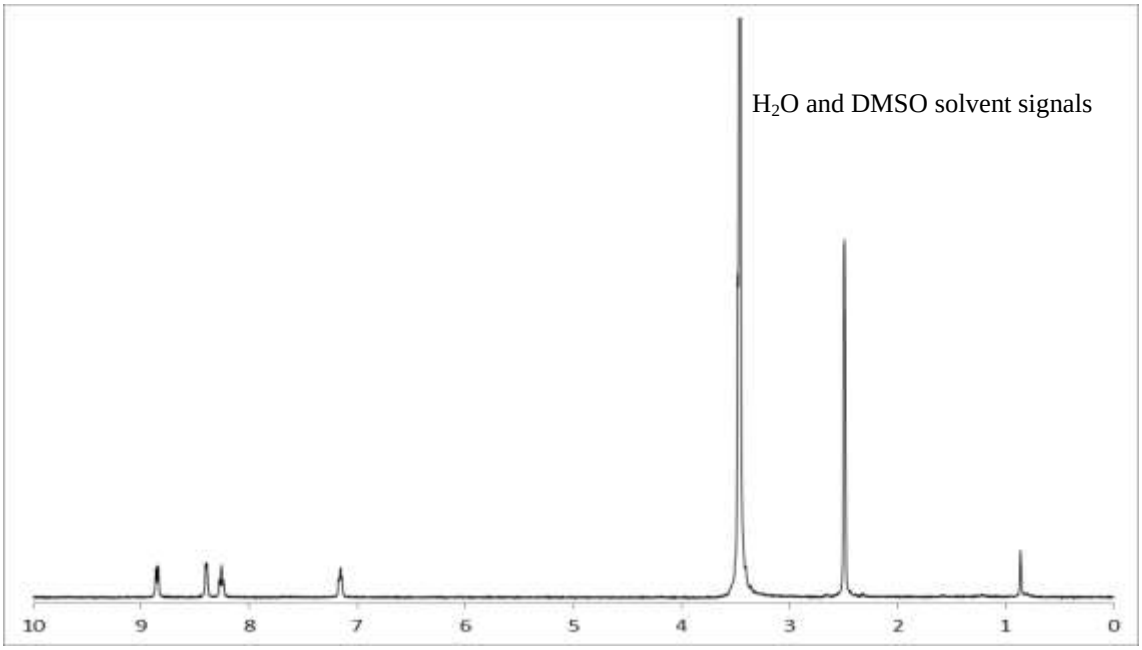

Figure 2.1. ^{1}H-NMR characterization of $[Co_4O_4(OAc)_2(bpy)_4]^{2+}$, (1B) complete spectrum (above), and insets (below).

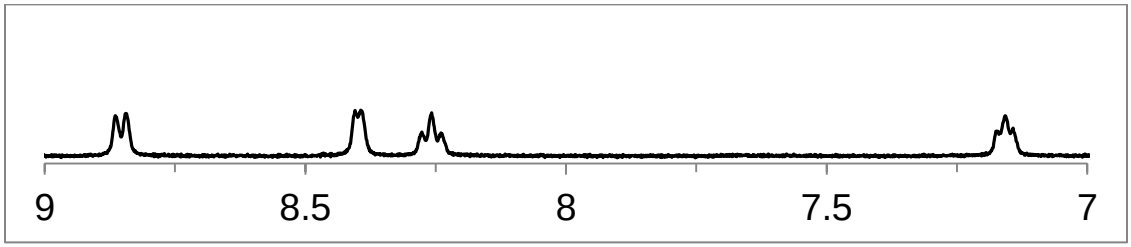

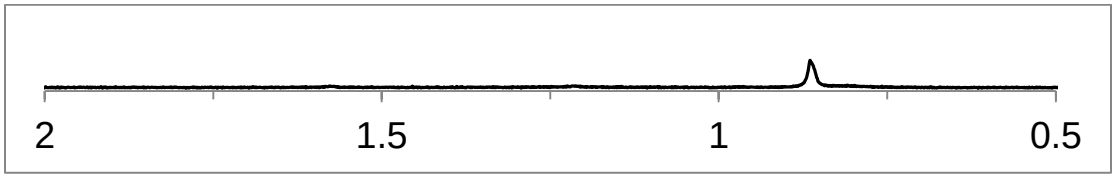

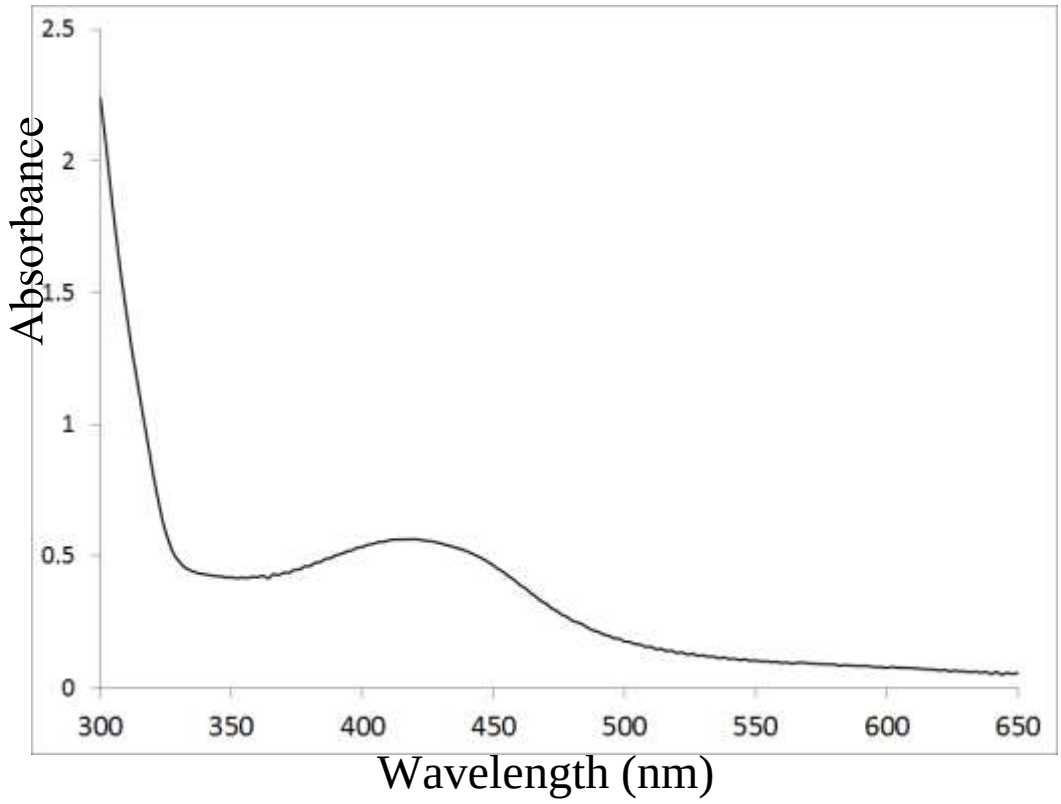

Figure 2.2. UV-Vis characterization of $Co_4O_4(OAc)_2(bpy)_4^{2+}$ **(1B)** in acetonitrile.

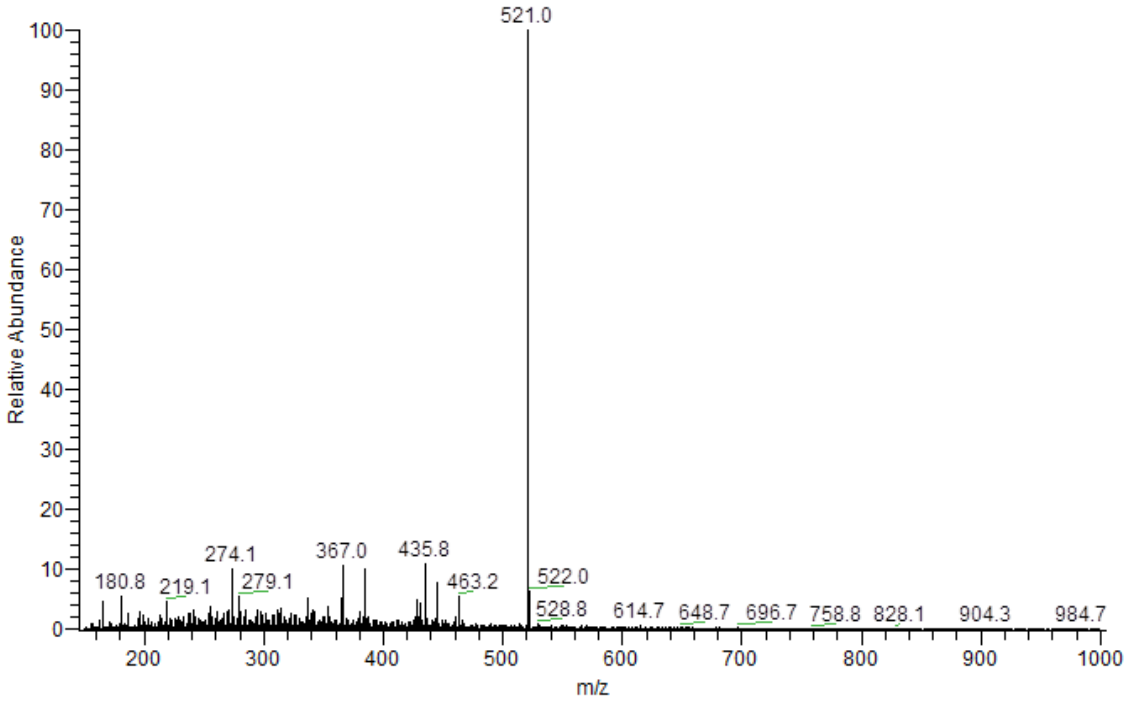

Figure 2.3. ESI-MS characterization of $Co_4O_4(OAc)_2(bpy)_4^{2+}$ (**1B**) in acetonitrile.

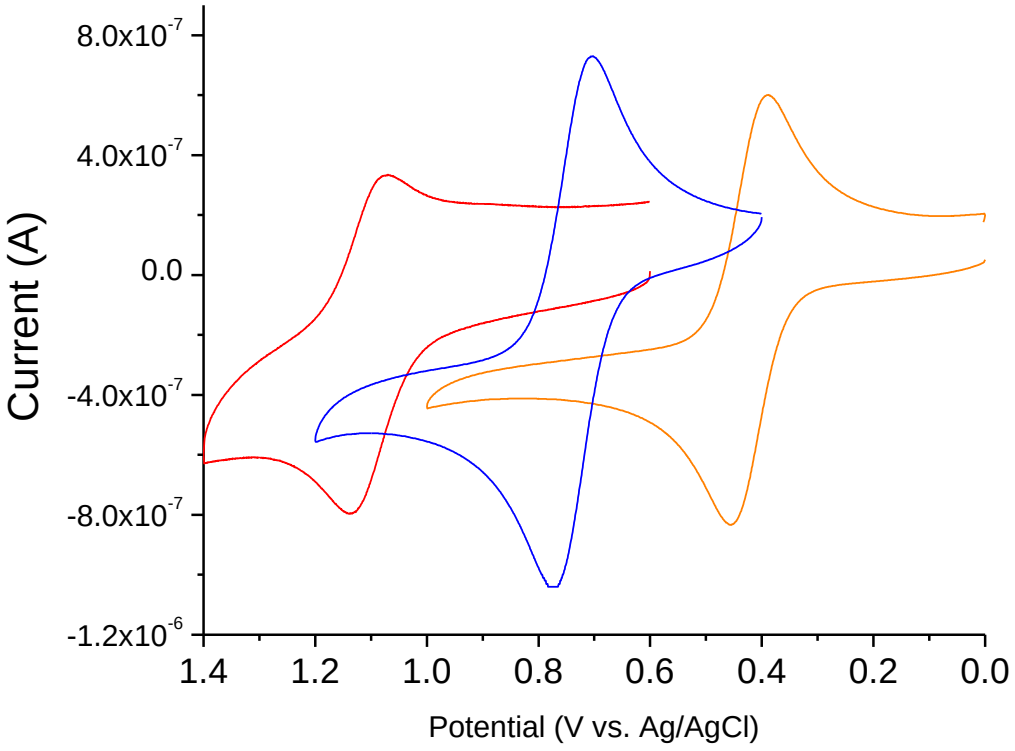

Figure 2.4. Cyclic voltammograms taken in acetonitrile (0.1 M $TBAPF_6$ electrolyte) of ferrocene (orange), **1A** (blue) and **1B** (red).

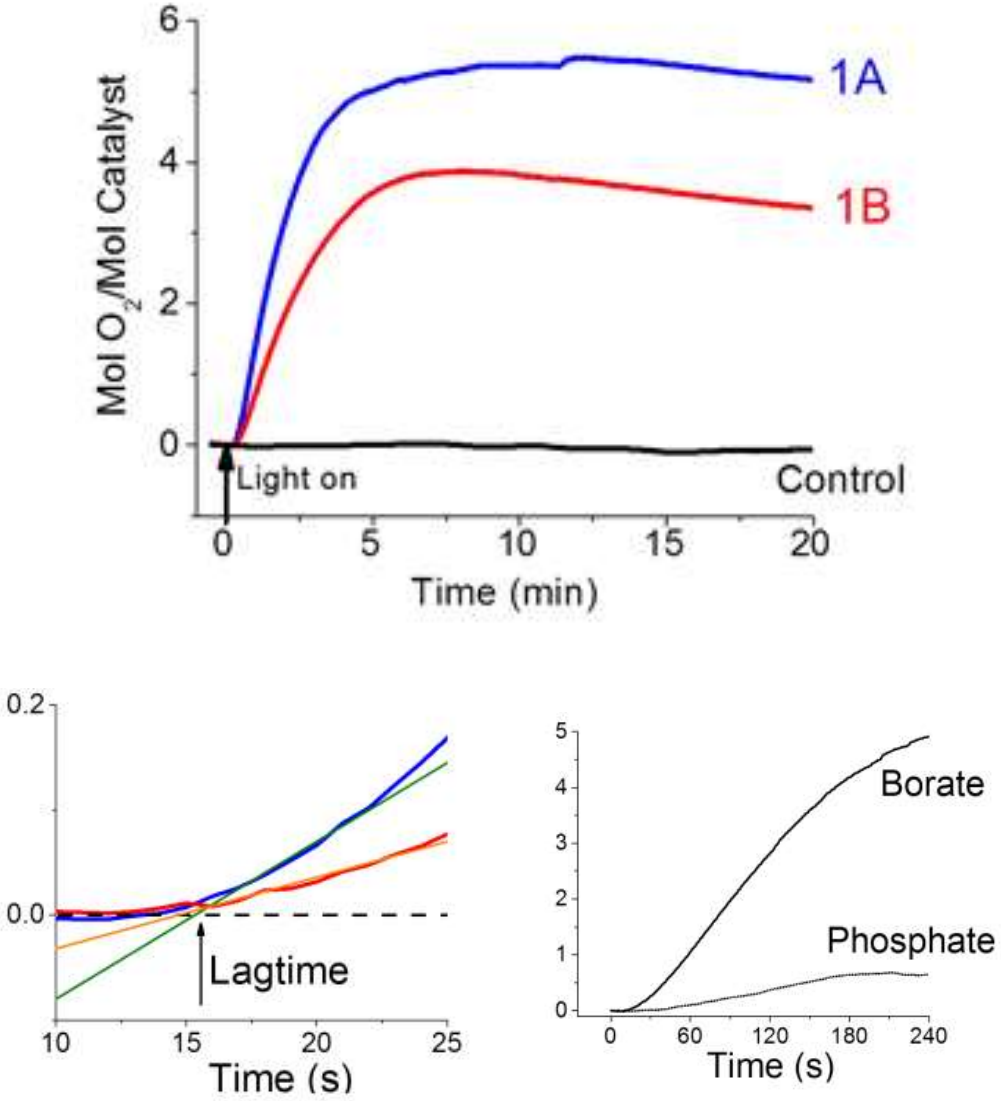

Figure 2.5. **Top**: O_2 evolution profiles for **1A** (blue) and **1B** (red) in borate. A control with neither catalyst (black) is also depicted. **Lower left**: The beginning period of illumination. Intercepts of extrapolated lines for **1A** (green) and **1B** (orange) allow quantification of lag time. **Lower right**: Profiles of **1A** in pH 8 buffers. Conditions: 100 μM catalyst, 1 mM $Ru(bpy)_3^{2+}$, 5 mM $S_2O_8^{2-}$, 0.05 M buffer, pH 8.

When considering cobalt based homogeneous water oxidation catalysts, experiments are required to ensure that the nascent molecular cluster, not decomposition products or cobalt oxide nanoparticles are the sole source of catalytic O_2 evolution[29–37]. As **1A** has been shown to be stable in the photoassay media under illumination[13] we anticipated that **1B** would be stable as well. To prove this, we compared ^{1}H-NMR of **1B** alone (Figure 2.6 bottom trace), $Ru(bpy)_3^{2+}$ and NaOAc (middle trace), and the contents of the photoassay after 10 minutes of O_2 evolution from 0.01 M borate buffer in D_2O (top trace). The fact that all peaks present after catalysis can be assigned to either $Ru(bpy)_3^{2+}$ or **1B**, and not free acetate, confirms that **1B** is the source of catalytic O_2 evolution, rather than a decomposed species. ESI-MS also confirms the presence of **1B** in solution after 10 minutes of catalysis (Figure 2.7). When borate buffer is removed from the photoassay conditions in Figure 1, neither **1A** nor **1B** demonstrates catalysis. ^{1}H-NMR analysis of this *inactive* solution revealed that *no peaks* of intact cubane (**1A** nor **1B**) are observed after as little as 5 minutes of illumination. Thus, photodecomposition of cubanes **1A** and **1B** is greatly suppressed in borate. This requirement for a chelating buffer like borate (or carbonate) for cubane catalytic activity may be more than only stability against photodecomposition. Mechanistically, this chelate influence could mean that catalysis may proceed via a base-dependent pathway, involving either deprotonation of an intermediate or hydroxide transfer from borate anion, $B(OH)_4^-$.

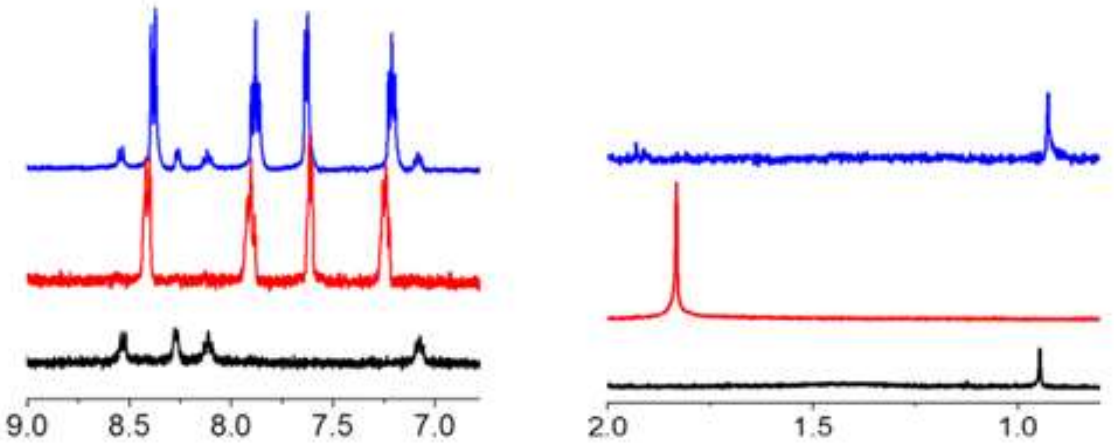

Figure 2.6. ^{1}H-NMR Stability of **1B** during catalysis. Black: **1B** alone. Red: $Ru(bpy)_3^{2+}$ and NaOAc. Blue: contents of photoassay in 90/10 D_2O/H_2O, pH 8 solution (0.01M in borate) after 10 minutes of catalysis.

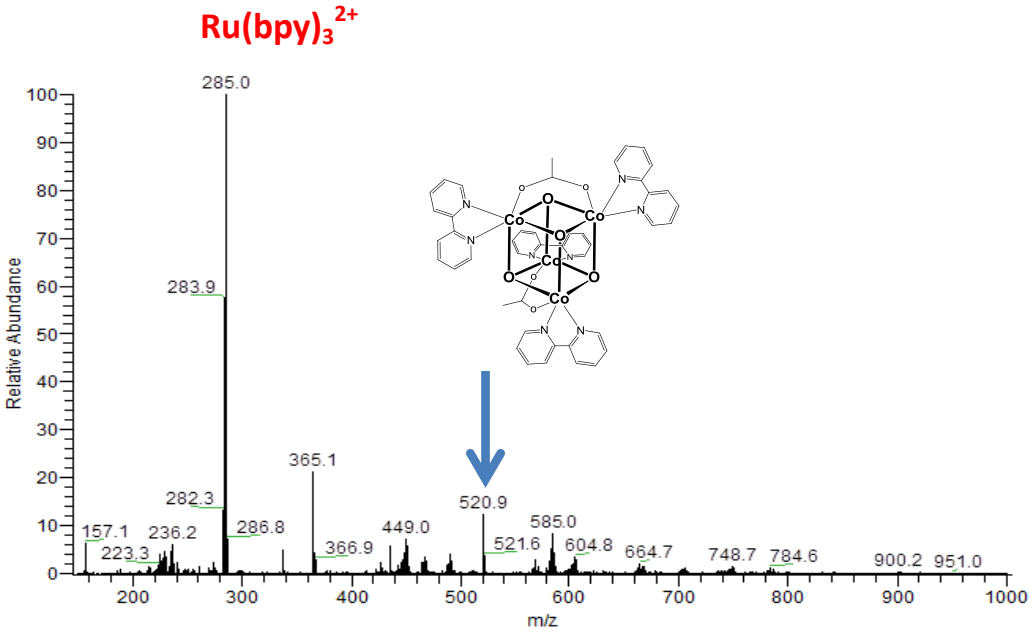

Figure 2.7. ESI-MS of the photoassay (conditions: 100 µM of **1B**, 0.5 mM $Ru(bpy)_3^{2+}$, 2.5 mM $Na_2S_2O_8$) before (above) and after (below) 10 minutes of illumination. Samples were diluted with acetonitrile prior to analysis. No peaks at 521 were observed in control samples ($Ru(bpy)_3^{2+}$ and $Na_2S_2O_8$ only) before or after illumination.

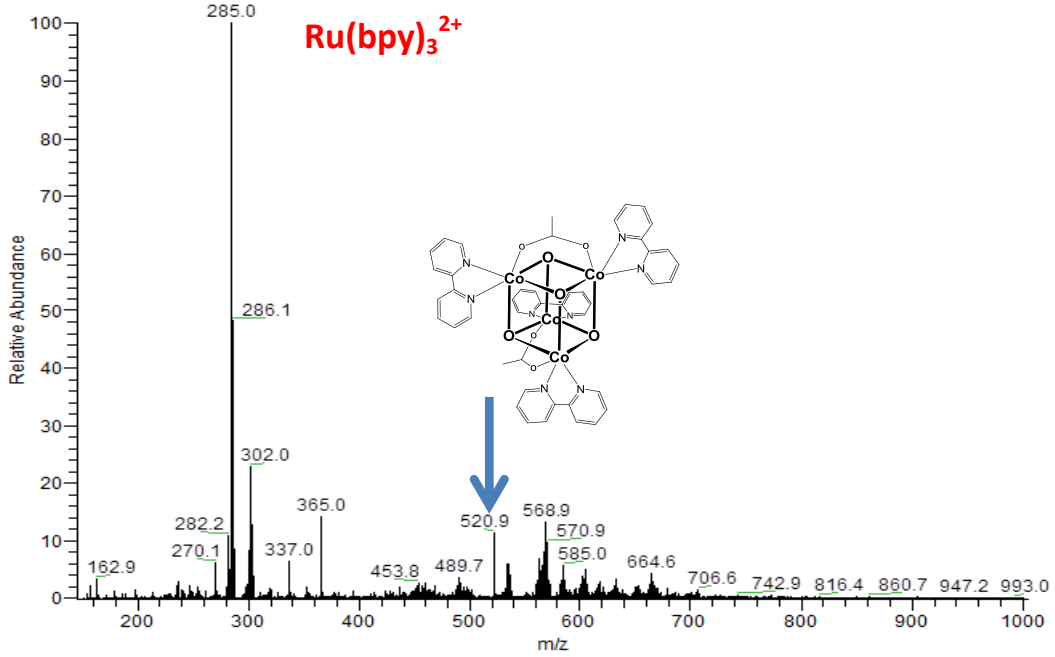

To test this idea we investigated the dependence of catalytic rate on buffer concentration. Remarkably, addition of borate (pH 8) shows an *inverse* relation between buffer concentration and O_2 evolution rate (Figure 2.8). While this trend is seemingly counterintuitive, we note that buffer-dye interactions must be present in excess of buffer-catalyst interactions, and that borate is known to accelerate the decomposition of $Ru(bpy)_3^{3+}$ via first-order kinetics (further, the rate constants for this decomposition compare to our observed O_2 evolution constants, suggesting an effect on the same timescale, see below)[38]. Further proof of this buffer induced dye decomposition effect is provided in Figure 2.5, which shows that when borate is replaced at the same pH with phosphate (a faster decomposer of $Ru(bpy)_3^{3+}$)[38], a dramatic decrease in O_2 evolution is observed. Our results agree with a previous report on an observed decrease in quantum yield as borate is replaced with phosphate[14]. Thus, while buffer is required for O_2 evolution and cubane stability against photodecomposition, determination of the reaction order dependence on buffer concentration is complicated by the buffer-dye reaction and the self-terminating nature of the photoassay.

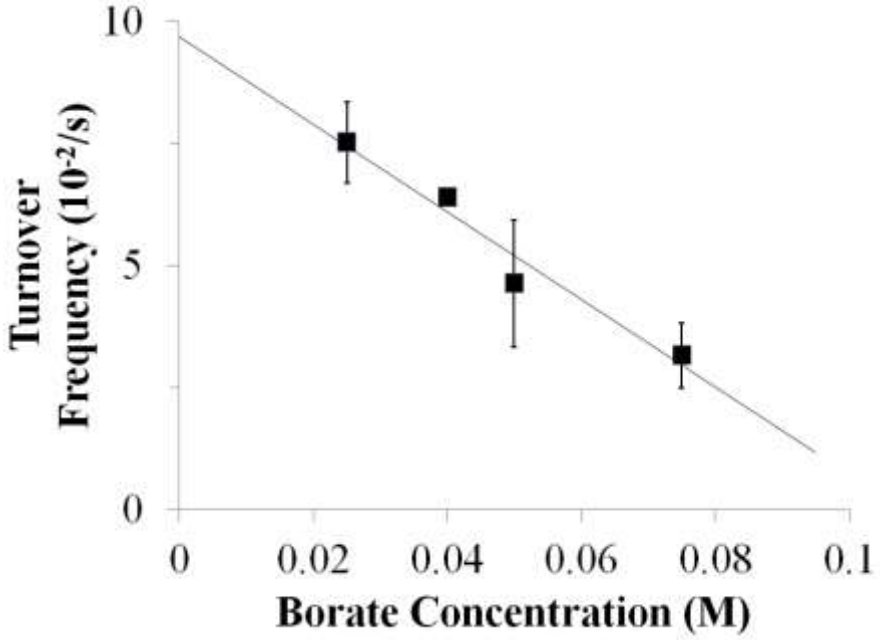

Figure 2.8. Turnover frequency for catalysis by **1A** as a function of borate buffer concentration. Conditions: 25 μM catalyst, 1 mM $Ru(bpy)_3^{2+}$, 5mM $S_2O_8^{2-}$, pH 8.

In light of recent reports regarding the sensitive use of conditions when studying homogeneous cobalt water oxidation catalysts, we paid careful attention to the choice of reaction conditions as described next[33,36,37]. For example, the lifetime of the photoassay can be extended to complete consumption of persulfate electron acceptor by using an acetonitrile-water solvent mixture[15]. To directly compare the kinetics of O_2 evolution from **1A** and **1B** we ultimately chose not to pursue this mixed solvent strategy because the potential for one electron oxidation of **1B** in acetonitrile (1.09 V vs. SHE) is not equal to that of **1A** (Figure 2.4); hence **1A** would receive a thermodynamic advantage. On the other hand, the reduction potentials reported for the $\mathbf{1A}^{+}$/**1A** and $\mathbf{1B}^{+}$/**1B** couples in water at pH > 4 are identical (1.25 V vs. SHE)[14,39]. Thus, while aqueous photoassays do not last to complete persulfate consumption, water-only solvent is used in order to allow for accurate comparison without significant thermodynamic contributions. Deliberately, we chose not to measure the onset potential for catalytic water oxidation for cubanes **1A** and **1B** via electrochemical methods, as we are currently unable to unambiguously assign the resulting data to solely the intact clusters. In fact, we have observed catalytic CoO_x films formed on the surface of glassy carbon electrodes as a result of decomposition of the cubanes at high potentials on glassy carbon, and we echo other studies[33,37] advising caution if considering studying homogeneous cobalt water oxidation catalysis via electrochemical methods. While we normally use bicarbonate buffer at pH 7 to screen catalysts (see below), this buffer failed to give consistent kinetic results for **1A** as previously reported[13]. This is due to poorer solubility windows of the photoassay components in concentrated bicarbonate. Despite the change in ligand environment between **1A** and **1B,** the Co_4O_4 core remains a catalytically active structure which acts

via a base dependent mechanism. Further comparisons between **1A** and **1B** are presented in the context of the following kinetic analysis.

As can be seen in Figure 2.5, **1B** evolves O_2 after the lag phase at a slower rate than **1A** over the same time scale. For both materials, the concentration curves plateau at ca. 5 minutes, after which a steady decrease is observed; this is expected given the self-terminating dye system utilized. To begin a kinetic analysis of these plots, we first consider the lag phase for both materials (Figure 2.5, inset), during which the assay is illuminated but no O_2 is evolved. The lag time is determined from the intercept of the linear extrapolated fit with the baseline. Under identical conditions, we did not observe noticeable difference between the lag time of **1A** and **1B.** The lag times decrease from 15 to 8 seconds with increasing [$Ru(bpy)_3^{2+}$] concentration (Figure 2.9), consistent with a mechanism that attributes the lag to the time required to photogenerate the oxidant and transfer holes into the cubane catalyst.

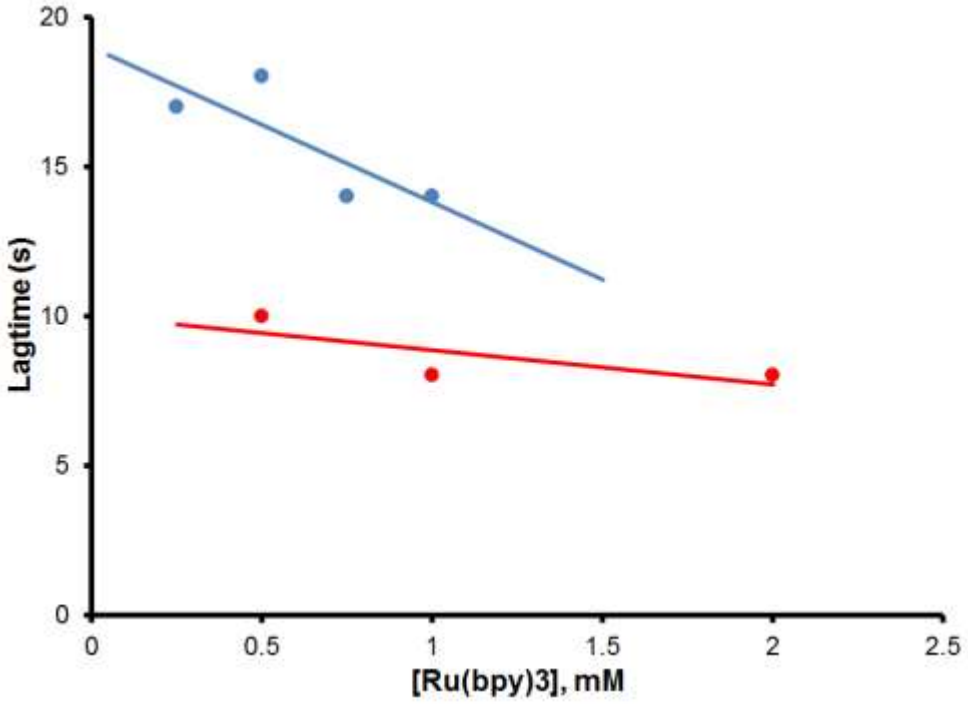

Figure 2.9: Lagtime as a function of initial $Ru(bpy)_3^{2+}$ concentration for 100 µM of **1A** (blue) and 300 µM of **1A** (red). Conditions: 5 mM $S_2O_8^{2-}$, pH 8.

From the slope of the initial linear portion of the plots in Figure 5, the initial rate of O_2 evolution (O_2/s) is obtained. A plot of these rates (μmol/s) vs. concentration of catalyst (μmol) gives a straight line for *both* cubanes (Figure 2.10, top), indicating that the observed catalysis is first-order in both **1A** and **1B**. Above catalyst concentrations depicted in Figure 2.10, the O_2 evolution rate was observed to remain unchanged for each cubane. In this region, the $[Ru(bpy)_3^{2+}]$:[catalyst] ratio is less than 10:1, which we interpret as being non-representative of pseudo first-order conditions. Hence, because the region in Figure 2.10 reflects a correlation of rate with concentration of catalyst, the kinetic representation for our data is eqn (1):

$$Rate = k[catalyst]\sum_i [oxidant]_i + C$$

$$= k'[catalyst] + C \qquad (1)$$

The slope of the lines in Figure 2.10 is thus the pseudo first-order rate constant (k') for each cubane. We obtain values of 0.030 for **1A** and 0.015 mol for **1B** in units of mol O_2 (mol catalyst * s)$^{-1}$. However, the y-intercepts are nonzero ($C_{\mathbf{1A}}$=0.0011, $C_{\mathbf{1B}}$=0.0007 μmol/s) implying the presence of a zeroth-order pathway. As described next, this zeroth-order contribution is a statistically significant contributor to the overall rate description. First, error analysis of the y-intercepts gives $0.0005 \leq C_{1A} \leq 0.0014$ (95% confidence) and $-0.0002 \leq C_{1B} \leq 0.0012$; these ranges indicate a nonzero y-intercept within experimental error. Second, a log/log plot of the data in Figure 2.10 gives straight lines with slopes of 0.59 for **1A** and 0.58 for **1B**. This fractional order also indicates the presence of multiple pathways.

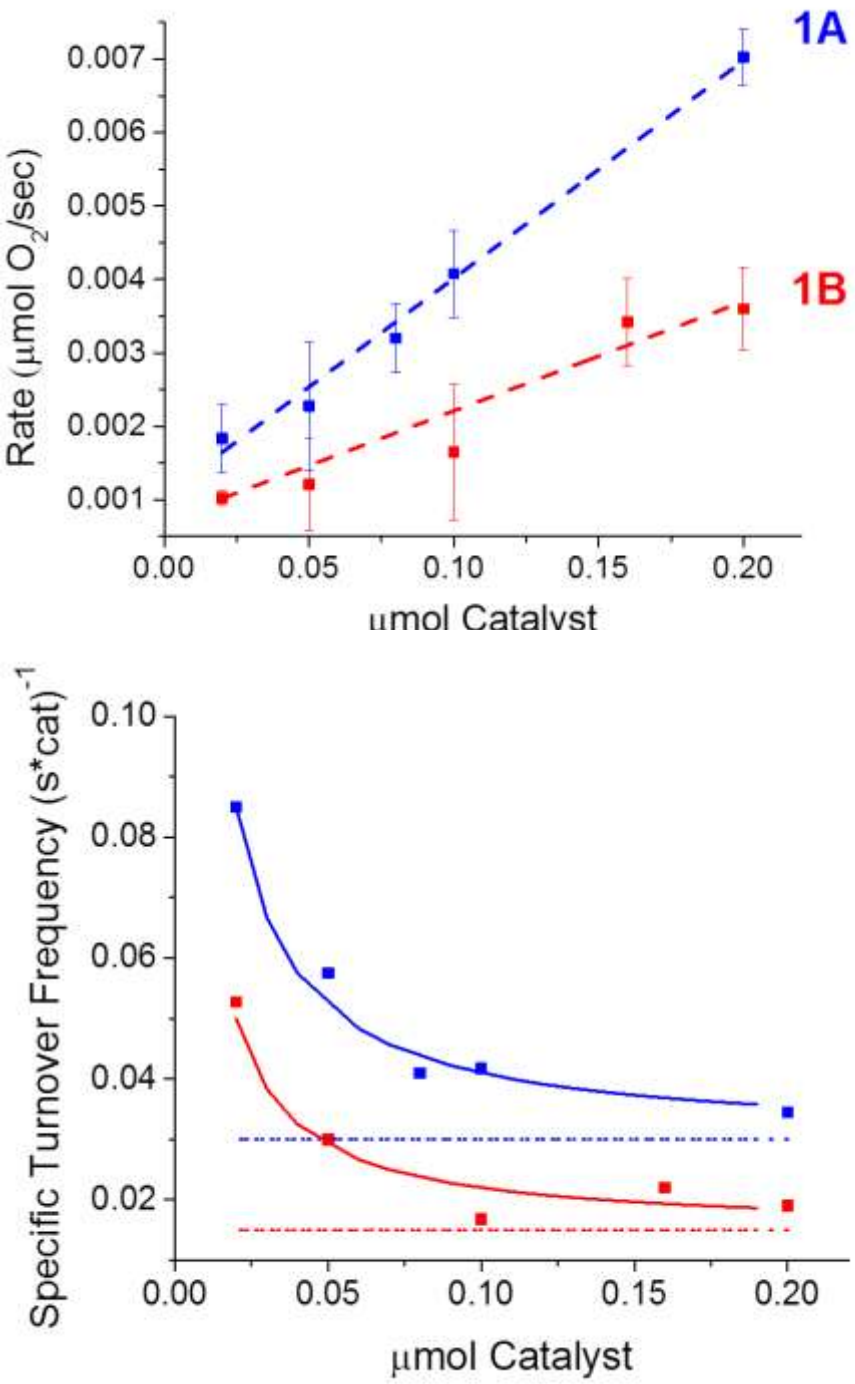

Figure 2.10. Top: Plot of O_2 evolution rate vs. catalyst concentration for 1A (blue) and 1B (red). Error bars represent standard deviation of the mean value of each point. **Bottom**: Plot of TOF vs. catalyst concentration for 1A (blue) and 1B (red). Dotted lines are the pseudo first-order rate constants. Solid lines are fits of equations 2 and 3. At least 6 independent trials are represented per data point.

Third, we obtain the turnover frequency per catalyst molecule (TOF), by normalizing the rates to the moles of catalyst in solution (Figure 2.10, bottom). Accurate fits of the data (solid lines) in the resulting plots are constructed only if a significant effect of the nonzero intercept term is included:

$$TOF_{\mathbf{1A}} = \text{Rate}/[\mathbf{1A}] = 0.030 + 0.0011/[\mathbf{1A}] \quad (2)$$

$$TOF_{\mathbf{1B}} = \text{Rate}/[\mathbf{1B}] = 0.015 + 0.0007/[\mathbf{1B}] \quad (3)$$

If the nonzero intercept term is omitted, the fit of solely the pseudo first-order rate constant (dotted lines, Figure 2.10, bottom) is poor. We conclude that a zeroth-order pathway exists in this system which is not explained by uncatalyzed O_2 production (Figure 2.5, control trace). As described next, this pathway is explained by the presence of a multistep mechanism derived from the presence of at least two oxidants from the photoassay medium.

As shown in equations 2-3, an inverse relation between TOF and [catalyst] is seen prominently at low catalyst concentrations. This inverse relationship indicates that catalyst molecules compete with each other for the oxidizing equivalents needed to produce O_2. In light of a previous report which suggested that the sulfate radical contributes to oxidizing **1A**[14], we suspected this oxidant to be necessary for O_2 evolution. The sulfate radical is formed *in situ* when excited $Ru(bpy)_3^{2*}$ is quenched by persulfate (Scheme 2.1). The $SO_4^{\bullet-}/SO_4^{2-}$ reduction potential is 2.4 V vs. SHE[40], significantly stronger than $Ru(bpy)_3^{3+}$/ $Ru(bpy)_3^{2+}$ (1.26 V vs. SHE). As a consequence of the high reduction potential, $SO_4^{\bullet-}$ readily oxidizes $Ru(bpy)_3^{2+}$, **1A**, and the Cl^- counterion[41]. Two

experiments verify that $SO_4^{\bullet-}$ is necessary for O_2 evolution. First, addition of excess (>500 eq.) $Ru(bpy)_3(ClO_4)_3$ to solutions of **1A** *failed to produce any O_2*, as monitored by Clark electrode.

Second, a series of photoassays in which 5mM NaCl or $NaClO_4$ was added prior to illumination and compared to a control with neither salt. As evidenced in Figure 2.11, addition of $NaClO_4$ gave a reproducible trace indistinguishable from the control with no $NaClO_4$; in contrast, NaCl drastically decreased the rate and yield of O_2 evolution. Chloride oxidation is thermodynamically too high (Cl_2/Cl^-, 1.36 V) to have an impact on any material in the photoassay other than the sulfate radical. Hence, we conclude that as part of the reaction mechanism, both **1A** and **1B** are oxidized by the sulfate radical in at least one of the four oxidation steps.

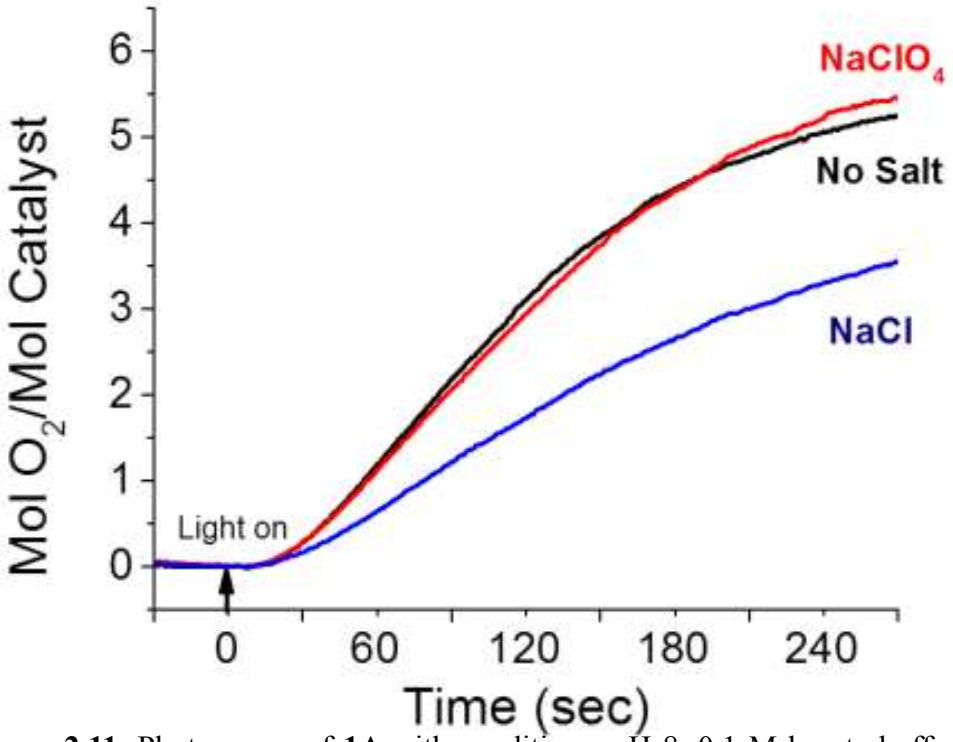

Figure 2.11. Photoassays of **1A** with conditions: pH 8, 0.1 M borate buffer, 1 mM $Ru(bpy)_3^{2+}$, 5 mM S_2O_8, 100 μM of catalyst, 5 mM salt.

The kinetic results further imply a mechanistic feature. Within experimental error, the zeroth-order constants C_{1A} and C_{1B} are both nonzero, however we cannot distinguish between the two values using their 95% confidence intervals. In contrast, there exists exactly a two-fold decrease in the observed pseudo first-order rate constants for **1B** vs **1A.**

This data strongly implies that a rate-limiting step occurs at a Co-OAc binding site, because the number of these coordination sites decreases by 50%. This result agrees with numerous literature reports of labile acetate ligands. Carboxylate exchange on **1B** has been demonstrated synthetically[23] and has been previously utilized to immobilize **1A** on functionalized silica[42]. Insights from EPR studies on both $\mathbf{1A}^{+}$ [43] and $\mathbf{1B}^{+}$ [28] show that, upon single electron oxidation, the hole is delocalized predominantly across the Co_4O_4 core, residually to the pyridine/bipyridine ligands, and not at all to the acetate, also confirming varying electronic interactions of the ligands on the core. In contrast, our own ^{1}H-NMR data indicate no observable exchange of pyridyl group ligands on the timescale of catalyst turnover. To our knowledge, there are no reports of pyridyl group exchange for either cubane.

Because a base is required for catalysis, we thus conclude that binding of substrate water or hydroxide to a carboxylate site (i.e., an oxo-transfer step) is part of the catalytic mechanism. When coupled to the proof that two species oxidize the cubane, it follows that this oxo-transfer step may occur before or after either oxidation step. These observations thus account for the presence of two observed pathways, one major (in which most catalyst molecules proceed via certain intermediates) and one minor (in which a small amount of catalyst molecules proceed via other intermediates).

One observation which may unify these views is that we cannot eliminate hydroxyl radicals (produced from the quenching reaction of the sulfate radical on water or OH^-) as the additional oxidant[41]. This will be elaborated in discussion.

To test whether binuclear "half cubane" and trinuclear "incomplete cubane" analogues of both **1A** and **1B** could act as catalysts for water oxidation, we synthesized and tested two dimers $[Co_2(OH)_2(OAc)_3(py)_4](PF_6)$ (**2A**), and $[Co_2(OH)_2(OAc)_3(bpy)_2](ClO_4)$ (**2B**), and two trimers $[Co_3O(OH)_2(OAc)_3(py)_5](PF_6)_2$ (**3A**), and $[Co_3O(OH)_3(OAc)_2(bpy)_3](ClO_4)_2$ (**3B**). Synthesis was conducted by procedures from the literature[23,25], and all clusters were characterized by ^{1}H-NMR and ESI-MS.

Figure 2.12 compares representative O_2 evolution profiles for these clusters as measured by Clark electrode (conditions: 0.1 M bicarbonate buffer at pH 7, 0.5 mM $Ru(bpy)_3^{2+}$, 20 mM $S_2O_8^{2-}$ in 90/10 H_2O/MeCN) compared to a blank photoassay (no cobalt). The results are ligand dependent. Both pyridine species (**2A**, **3A**) exhibit O_2 uptake followed by recovery and finally catalytic O_2 evolution after a delay. Both other samples (**2B, 3B**) and the control are not only catalytically inactive, but also indicate the presence of a reaction that consumes O_2 below the baseline. Given the almost identical structures of **2A** and **2B**, we sought to reconcile this data. Next we present several lines of evidence showing that the pyridyl complexes **2A** and **3A** actually decompose to a different product which does catalyse water oxidation. By contrast, the more stable coordination of bipyridine to both **2B** and **3B** prevents photodecomposition and neither complex is active catalytically.

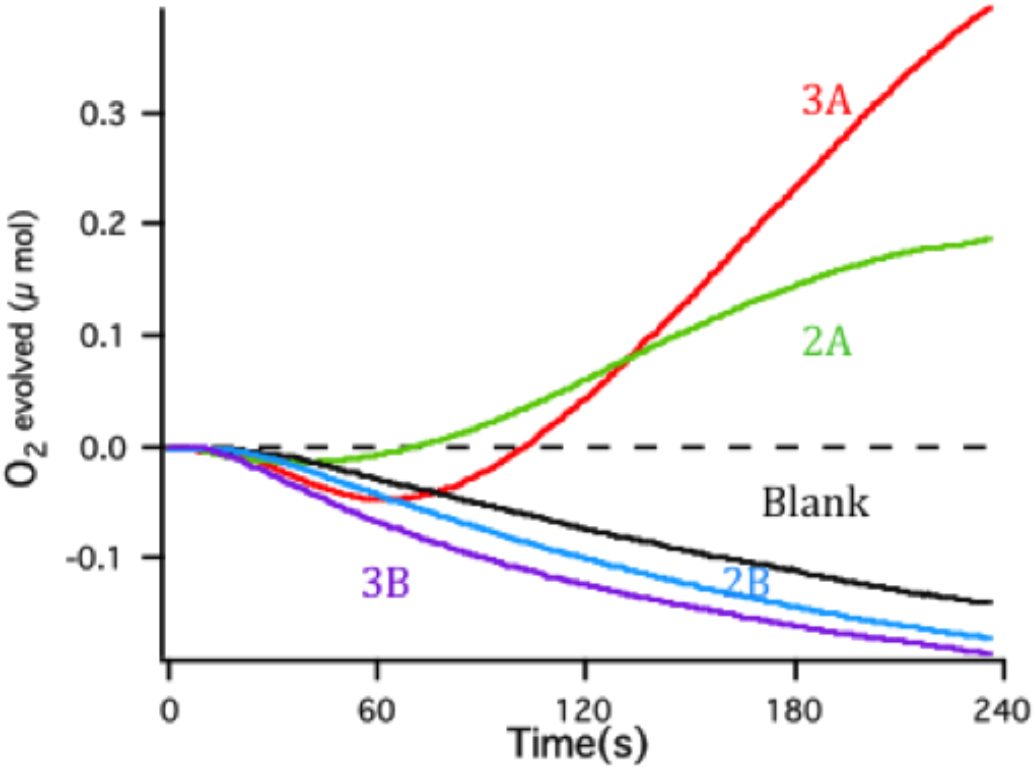

Figure 2.12: Representative O_2 evolution profiles for lower nuclearity materials as measured by Clark electrode, 0.1 M bicarbonate buffer at pH 7, 0.5 mM $Ru(bpy)_3^{2+}$, 20 mM $S_2O_8^{2-}$ in 90/10 H_2O/MeCN. Cluster concentrations; 100µM. Illumination begins at time t=0.

The observation that complexes **2A** and **3A** take up O_2 from solution under illumination during the long lagphase before catalytic O_2 evolution, in contrast to the profiles of **1A** and **1B**, indicates another reaction(s) occurs. For **2A** and **3A**, the lag times (time to reach the minimum O_2 concentration) were in excess of 30 seconds and often exceeded one minute, which compares to the lag times for $Co^{2+} \rightarrow CoO_x$ catalyst under identical conditions[13]. The observed lag times thus suggest that decomposition products, not **2A** and **3A**, are the source of observed O_2 evolution.

Further evidence for decomposition of **2A** and **3A** was obtained by monitoring the photoassay solutions via ^{1}H-NMR in 95/5 D_2O/CD_3CN (Figure 2.13). Before illumination all peaks can be assigned to intact cluster or $Ru(bpy)_3^{2+}$. However, after 10 minutes of illumination, additional peaks which correlate neither to **2A** nor **3A** are seen in the pyridine and acetate regions. These new peaks do not correspond to free ligands, thus revealing the presence of new molecular species.

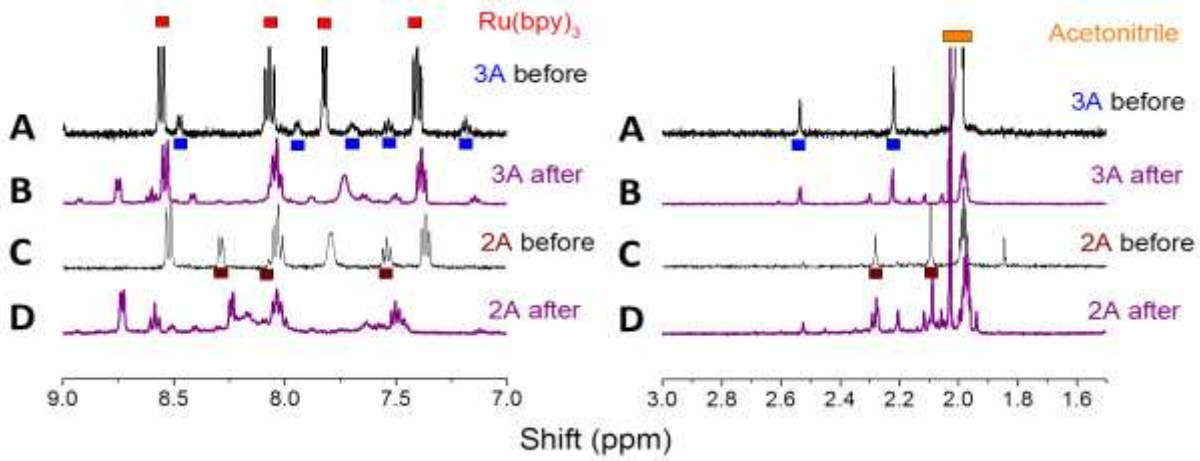

Figure 2.13: ^{1}H-NMR stability tests of **2A** and **3A** before and after 10 minutes of illumination in 95/5 D_2O/CD_3CN, 0.05 M pH 8 borate buffer. Lines A and C are before measurements, lines B and D are after.

Electrochemical oxidation allowed definitive attribution of catalytic activity to decomposition product(s) rather than intact **2A** or **3A**, in agreement with the results from photoassay studies. Cyclic voltammetry (CV) of **2A** and **3A** in 0.1 M, pH 7.5 bicarbonate buffer (90/10 H_2O/MeCN) on glassy carbon shows no significant increase in current relative to a blank CV of pure electrolyte. We then electrolyzed solutions of each compound at 1.05 volts vs. Ag/AgCl, (similar to the redox potential of the $Ru(bpy)_3^{2+/3+}$ couple), and performed cyclic voltammetry of the resulting solutions *with a polished separate electrode*. This ensures that any changes in the electrochemical response of **2A** and **3A** were not simply due to the formation of a heterogeneous cobalt oxide film. The CV traces of **2A** taken after 0 (red), 3 (blue), 6 (purple) and 12 (green) minutes of electrolysis show the gradual appearance of a catalytic wave, illustrating the formation of an active homogeneous or suspended species (Figure 2.14). A similar change was observed for solutions of **3A** (Figure 2.15). Attempts to isolate and characterize the catalytically active species were unsuccessful. UV-Vis of the electrolyzed solutions over time showed disappearance of **2A** and **3A** absorbance features, but failed to identify any new features. ^{1}H-NMR of the resulting solution indicated the presence of multiple molecular species (Figure 2.16), which were not characterized further. These results indicate that **2A** and **3A** are inactive as catalysts and photodecompose or oxidatively rearrange into active species.

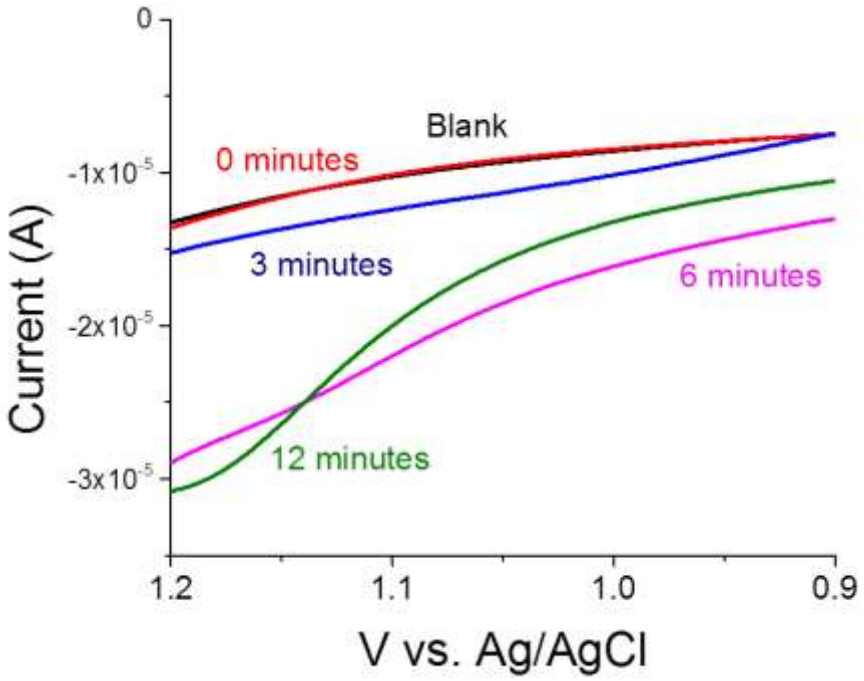

Figure 2.14: Linear voltammetry of 0.2 mM of **2A** in 0.1 M pH 7.5 bicarbonate (90/10 H_2O/CH_3CN) after various electrolysis times (1.05 V vs. Ag/AgCl). The black trace corresponds to blank electrolyte.

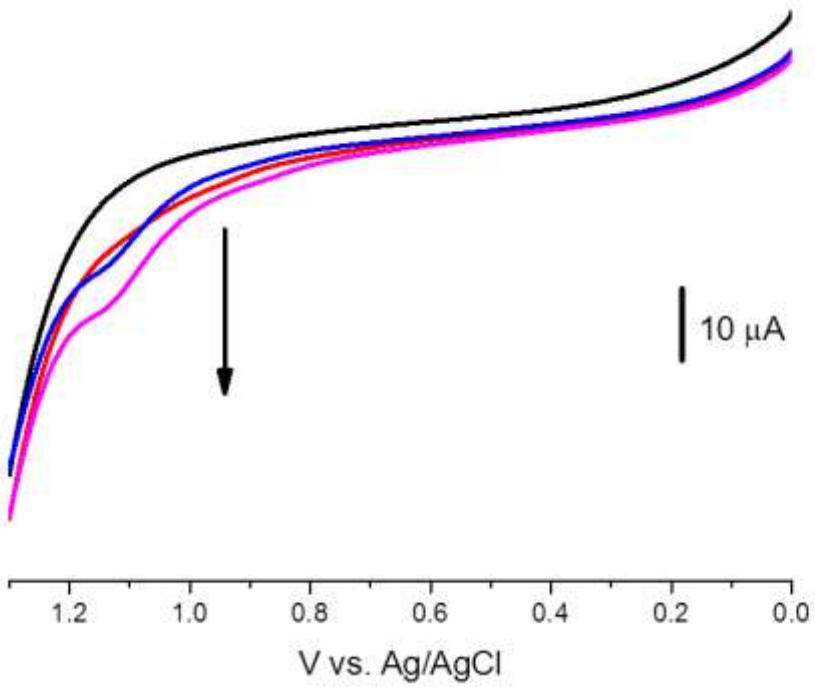

Figure 2.15. Linear voltammetry of electrolyzed solutions of 0.2mM **3A** in 0.1 M pH 7.5 bicarbonate buffer 90/10 H_2O/MeCN. Solutions were electrolyzed on a platinum mesh for 0 (black), 3 minutes (red), 6 minutes (blue) and 12 minutes (purple) at 1.05V. Working electrode: glassy carbon; counter electrode: platinum; reference electrode: Ag/AgCl.

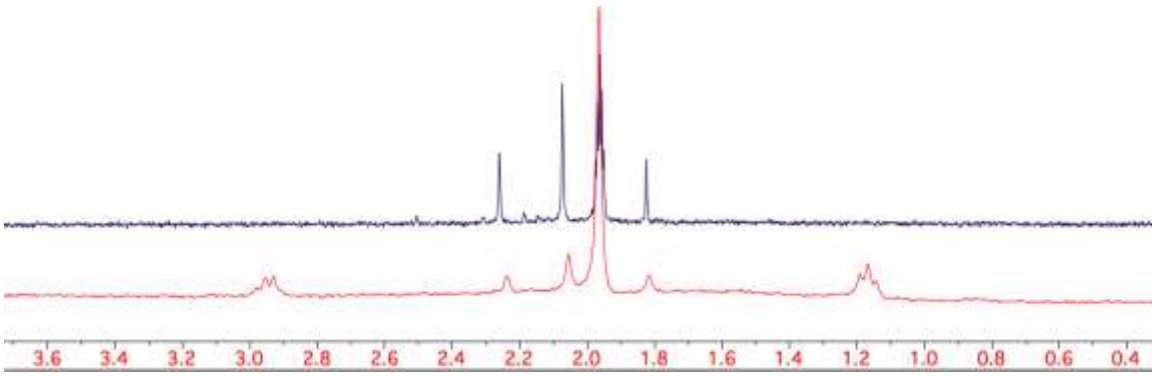

Figure 2.16: ^{1}H-NMR of 0.2mM **2A** before (blue) and after (red) 4950 seconds of electrolysis at 1.1V vs Ag/AgCl. Electrolysis conditions; 0.2mM **2A** in 0.1M pH 8 borate buffer 93/7 H_2O/MeCN for 4950 seconds at 1.1V vs Ag/AgCl. Spectrum taken after electrolysis shows multiplets consistent with formation of another molecular species.

By contrast, tests of O_2 evolution from the bipyridyl species **2B** and **3B** (Figure 2.12) show low level uptake of O_2 from the photoassay solution even after ten minutes of illumination. This O_2 uptake is small (< 5%) compared to the yield of catalytic O_2 produced by an equivalent amount of either cubane **1A** or **2A** (Figure 2.5). We tested this in some detail and found that > 50% of the O_2 uptake could be attributed to the photoassay medium (Figures 2.17 and 2.18).

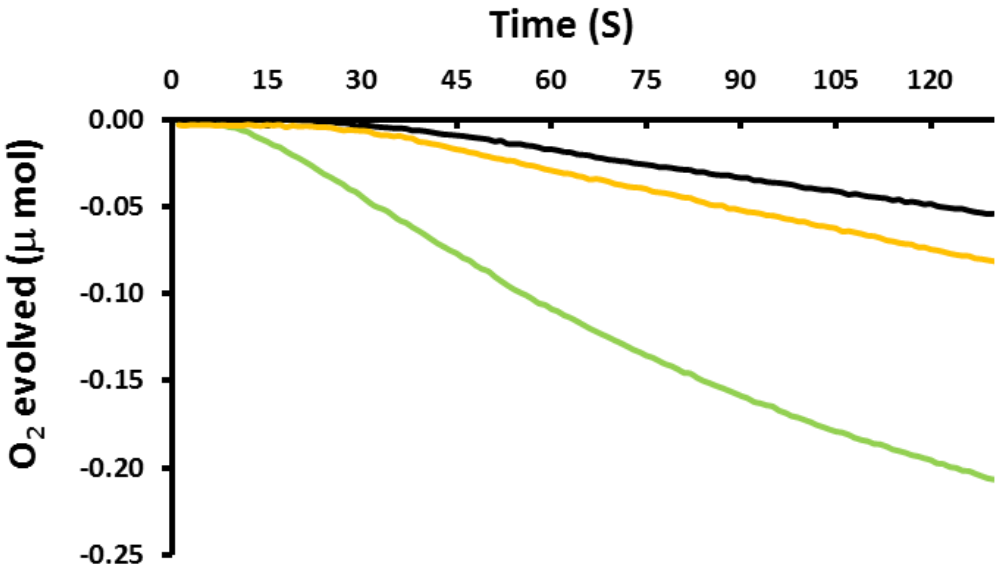

Figure 2.17: O_2 uptake by $Ru(bpy)_3$ photoassay, varying solvent composition. O_2 uptake accelerated as solvent composition was varied from 100% H_2O (black) to 90/10 H_2O/MeCN (yellow), to 75/25 H_2O/MeCN (green). Conditions: pH 7 0.1M $NaHCO_3$, 0.5mM $Ru(bpy)_3^{2+}$, 20mM $Na_2S_2O_8$.

Figure 2.18: *Left*: O_2 uptake by photoassay alone (black), 0.1 mM **2B** red, and 0.2mM **2B** (green). *Right*: O_2 uptake by photoassay alone (black), 0.1 mM **3B** purple, and 0.2mM **3B** (yellow). Photoassay conditions: 0.1M $NaHCO_3$ pH 7 buffer in 90/10 H_2O/MeCN

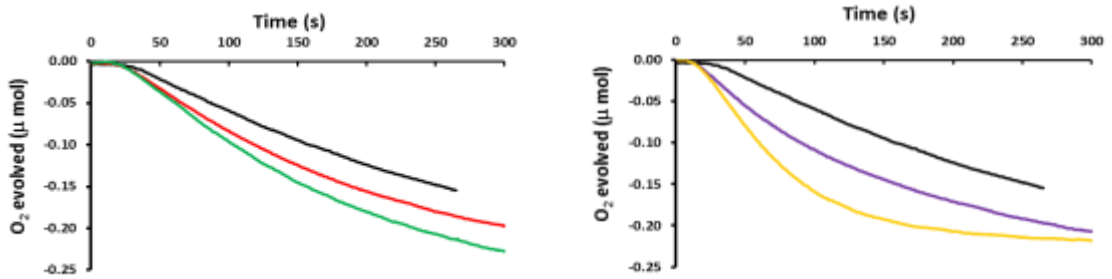

Left: Plot of maximum rate of O_2 uptake vs. concentration of **2B** (blue diamonds) and **3B** (red triangles) for trials shown above. Rates of O_2 uptake were greater for **3B** than **2B**, and rates of uptake were observed to increase with concentration of both **2B** and **3B**. *Right*: variance of O_2 uptake by $Ru(bpy)_3$ as a function of [$Ru(bpy)_3$]. Blue, 0.05mM $Ru(bpy)_3$, Red, 0.125mM, Green, 0.38mM, Purple, 0.5mM.Photoassay conditions; 0.1M pH 7 $NaHCO_3$ buffer, 20mM NaS_2O_8 in 90/10 H_2O/MeCN

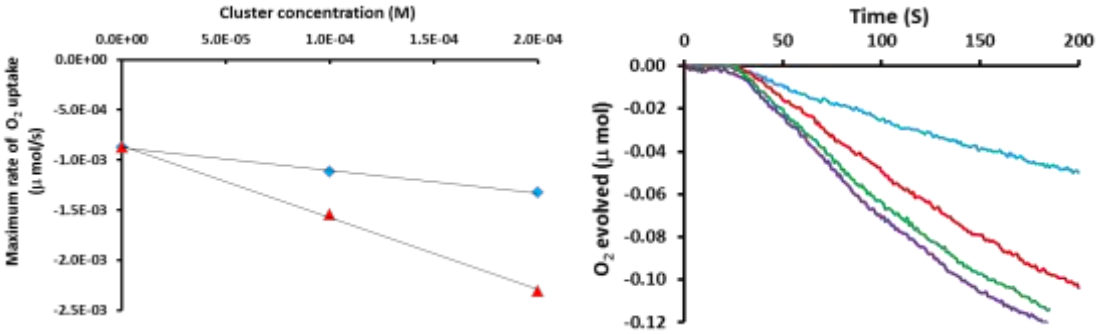

The stark differences between **2A** and **3A**, which decompose to form active materials, versus **2B** and **3B** which shows no O_2 evolution, prompted us to investigate the role of the bipyridine ligand in suppressing catalytic O_2 evolution. Bpy has been previously noted to poison amorphous CoO_x which may form *in situ*, and can serve as a ligand to determine the origin of catalytic activity.[9] Titration of bipyridine into the photoassay medium containing the pyridyl complex **2A** (Figure 2.19) significantly increases the lag time preceding net O_2 evolution from 30 seconds (0 equivalents bpy), to 90 seconds (.0625 equivalents, yellow), to 110 seconds (0.125 equivalents, red). When excess bpy (>5 equivalents) is added no net O_2 evolution is observed up to 5 minutes of illumination, and the O_2 profiles largely resemble those of **2B** and **3B** (Figure 2.20). On the other hand, titration of free bpy into **2B** or **3B** showed no further changes (Figure 2.21), indicating that free bpy alone is not responsible for O_2 uptake. Thus, we propose that the weak O_2 consumption exhibited by **2B/3B,** and **2A/3A** in the presence of bpy, is consistent with irreversible oxidation of bpy chelated to cobalt, possibly by attack of an oxo/hydroxo ligand on the bpy. Further, bpy chelation to these precursor complexes slows or prevents them from forming the active CoO_x decomposition product.

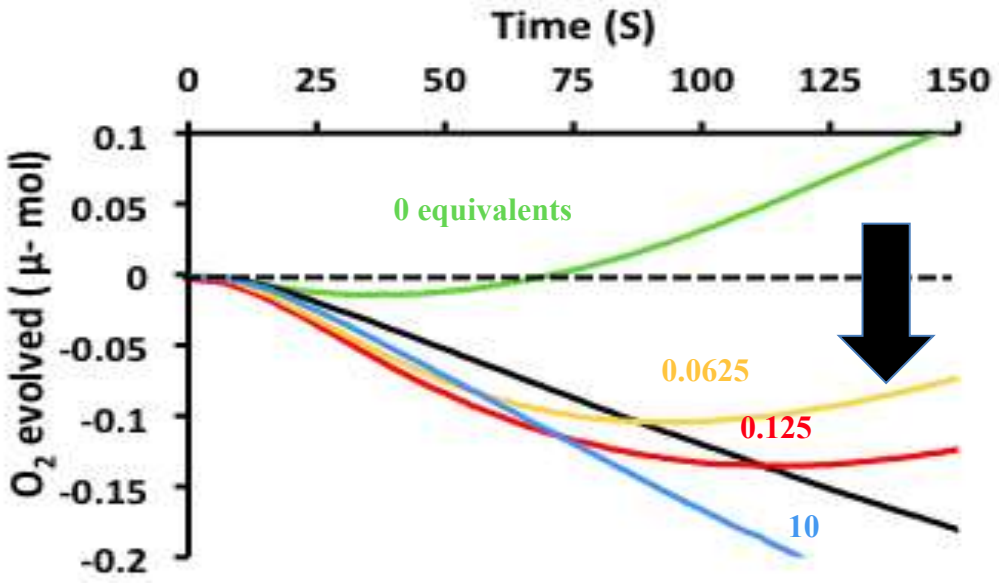

Figure 2.19: Clark electrode traces of 0.1 mM solutions of **2A** with equivalents of bipyridine. The black trace is a control (no **2A**) as reference. Conditions: 0.1 M bicarbonate buffer (pH 7), 0.5 mM $Ru(bpy)_3^{2+}$, 20 mM $S_2O_8^{2-}$, 90/10 H_2O/CH_3CN.

Figure 2.20: Addition of excess (top) and substoichiometric (bottom) bpy to photoassays containing **3A**.

Black; blank photoassay, blue 0.1mM **3A**, green; **3A** with 5 equivalents bpy, red; **3A** with 10 equivalents bpy, purple; **3A** with 25 equivalents bpy added. Photoassay conditions; 0.1M pH 7 $NaHCO_3$ buffer, 0.5mM $Ru(bpy)_3$, 20mM NaS_2O_8 in 90/10 H_2O/MeCN

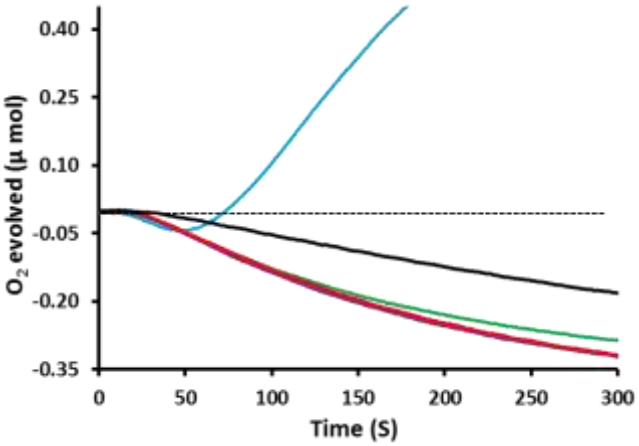

Black; blank photoassay, blue 0.1mM **3A**, yellow; 0.1mM **3A** with 0.25 equivalents bpy added. Photoassay conditions; 0.1M pH 7 $NaHCO_3$ buffer, 0.5mM $Ru(bpy)_3$, 20mM NaS_2O_8 in 90/10 H_2O/MeCN

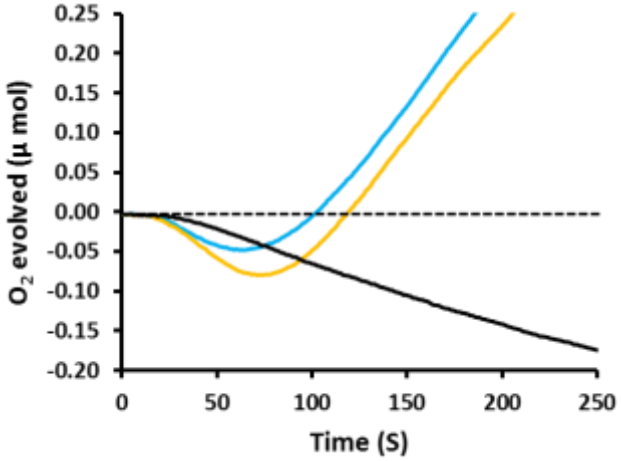

Figure 2.21: Addition of excess bpy to $Ru(bpy)_3^{2+}$ (top) and **2B** and **3B** (bottom).

Black; 0mM bpy, red; 0.18mM, yellow; 0.36mM, blue; 0.72mM, green; 2.88mM bpy added. Photoassay conditions; 0.1M pH 7 $NaHCO_3$ buffer, 0.5mM $Ru(bpy)_3$, 20mM NaS_2O_8 in 90/10 H_2O/MeCN

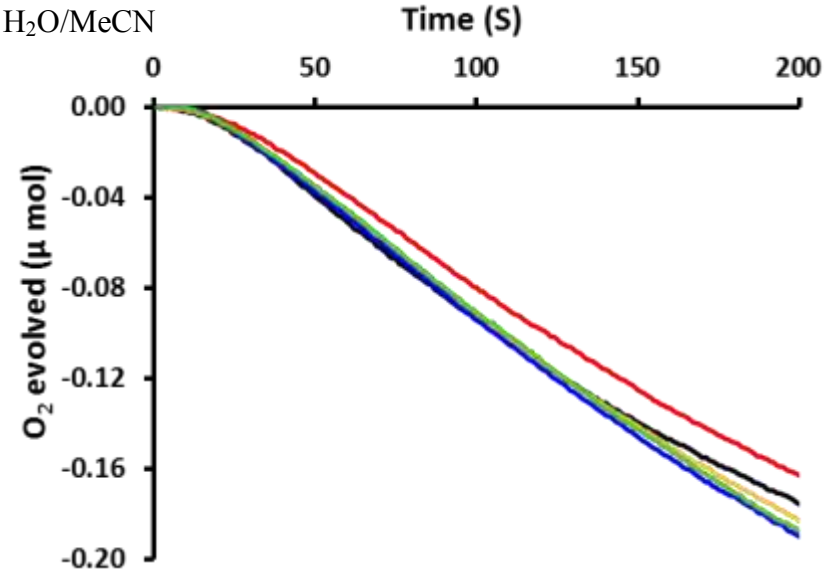

Black; blank photoassay, yellow 0.1mM **2B**, red 0.1mM **2B** with 1mM bpy added, green; 0.1mM **3B**, purple; 0.1mM **3B** with 1mM bpy added. Photoassay conditions; 0.1M pH 7 $NaHCO_3$ buffer, 1.1mM $Ru(bpy)_3$, 20mM NaS_2O_8 in 90/10 H_2O/MeCN

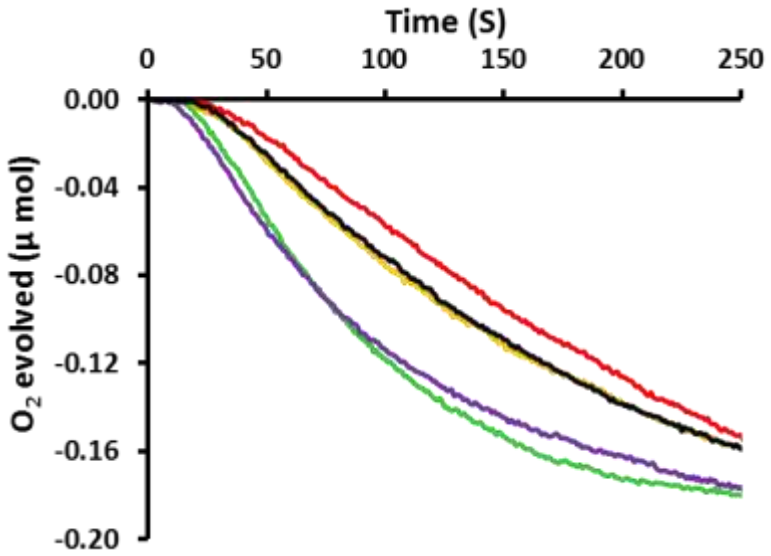

2.5Discussion

We have shown that in neutral and near neutral pH conditions, two fully assembled cubane motifs, **1A** and **1B,** are intrinsically active catalysts for water oxidation, and that their relative rates scale precisely with the number of labile carboxylate sites. By contrast, molecular cobalt-oxo clusters of lower nuclearity- half cubane dimers and incomplete cubane trimers- are catalytically inactive, even though both dimers and trimers have bridging oxos and labile carboxylate sites where terminal water molecules may exchange. Comparing the activity of the compounds tested in this study to the structural parameters listed in Table 2.1 reveals that the O-O, Co-O, and Co-Co bond distances are largely conserved across all clusters tested. Thus, no major changes in bond distances are responsible for the sudden appearance of O_2 production as Co nuclearity increases to four in both these series. We conclude that a four-electron oxidation pathway is not accessible in these dimers and trimers, and that the Co_4O_4 cubane topology provides the necessary pathway for activation and O-O bond formation.

Our report of inactivity from organo-cobalt clusters with nuclearity less than 4 stands in contrast to reports of catalytic activity from several organo-Co_2O_2 dimers[44] and Co monomers[45–49,31,50]. The proposed mechanisms for these materials from their original literature are presented in Scheme 2.2.

Scheme 2.2. Proposed mechanisms of water oxidation by other cobalt clusters[28,42-47] and theoretical calculations (bottom)[48].

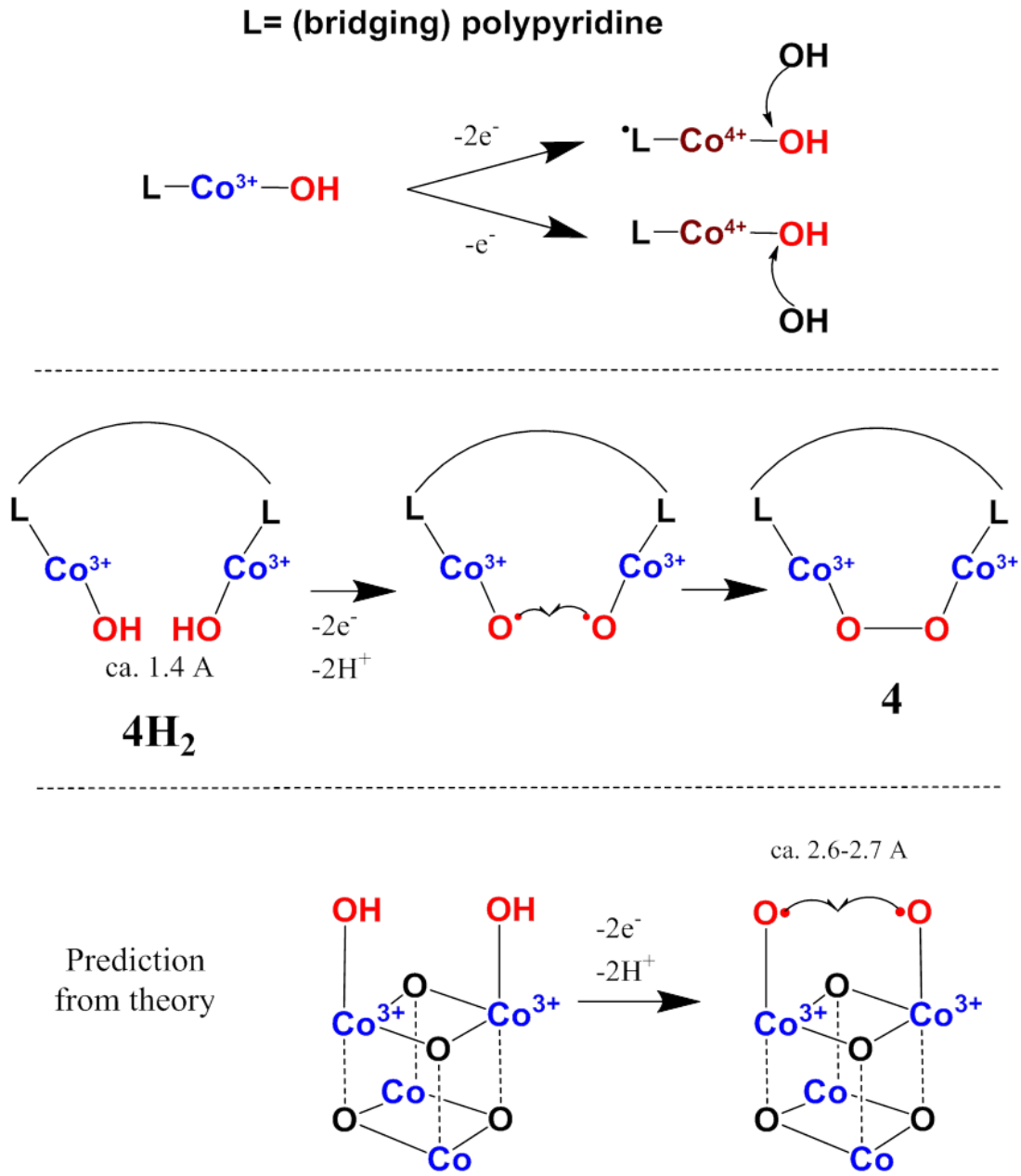

To our knowledge, a nucleophilic attack mechanism of water or hydroxide is proposed for all the catalytic monomers[45–49,31]. Since these studies are performed at pH ≥ 7, we depict hydroxide as the attacking substrate (Scheme 2.2, top) for simplicity. The oxidation state of the catalyst that is immediate precursor to O-O bond formation is uncertain, and different claims have been made. For example, Berlinguette et al. and Sartorel et al. postulate Co^{4+}-OH and Co^{4+}=O, respectively, in their systems[45,47,31]; these are both formally $1e^-$ above a Co^{3+}-OH moiety. On the other hand, Nocera et. al. and Groves et. al. propose $2e^-$ above Co^{3+}-OH in their systems; their catalysts are abbreviated ●L-Co^{4+}-OH, where the second hole is ligand-centered[48,49]. The reasons for these differences are not known, but may reflect their different coordination environments. It becomes apparent upon increasing cobalt nuclearity that multiple metals may contribute to the O-O bond formation step, as opposed to tailoring the electronic environment around a single, active metal center. This is evidenced in the proposed mechanism for the known dimer catalysts (Scheme 2.2, middle). $[Co(L)]_2(\mu\text{-bpp})(\mu\text{-}1,2\text{-}O_2)^{3+}$ (L= terpyridine or bis-N(methyl-imidazoyl)pyridine, bpp=bispyridylpyrazolate) each contain a bound peroxo, Co^{3+}-O-O-Co^{3+}, when isolated[44]. We label this structure **4** in Scheme 2.2. During catalytic turnover, the proposed reduced intermediate $\mathbf{4H_2}$ consists of two terminal Co^{3+}-OH groups. The first two oxidations generate two Co^{3+}-O● in which the unpaired electron occupies an antibonding 2pπ orbital on oxygen. (This electronic configuration is formally equivalent to Co^{4+}=O, in which an electron is promoted from a filled 3dπ orbital on Co to fill the π bonding orbital to oxygen that is denoted by the double bond. An unpaired electron exists in the $(3d)t_{2g}^5$ orbitals on Co, formally denoted Co^{4+}. For simplicity, we retain the oxo radical notation here). Unlike the nucleophilic

attack mechanism, the peroxo bond is formed via coupling of the two Co^{3+}-O● groups. This mechanism has been postulated to occur for the Co_4O_4 cubane with an energy barrier of 2.3 kcal/mol based on DFT calculations[50] (Scheme 2.2, bottom). We note that this cross-coupling mechanism indirectly implies that a single Co^{3+}-O● (equivocally Co^{4+}=O) is insufficient to oxidize water via a nucleophilic attack mechanism. This is substantiated by several Co^{3+}-OOR alkylperoxide systems, in which the Co^{3+}-O● generated by homolytic bond cleavage is a weaker oxidant of hydrocarbons than the counterpart ●OR[51–53].

Applying these parameters to our system, we note that all intramolecular O-O bond distances are conservatively estimated to be ca. 2.5 Å, a full angstrom longer than peroxo bonds (Table 2.1). For this reason, intramolecular coupling between *bridging* O-O is unfavorable in *any* of our compounds (active and inactive). An alternate possibility for intramolecular *terminal* O-O coupling can be envisioned (as in Scheme 2.2, bottom). However, this requires *full* dissociation of a (bidentate) acetate, and must occur over Co-Co distances in the range of ca. 2.6-2.8 Å (Table 1). A recent study reports only a small contraction (0.03 Å) of some Co-Co distances from **1A** to $\mathbf{1A}^{+}$, indicating this Co-Co distance remains relatively long upon hole injection[54]. Combined with the lack of free acetate detection in solution, these lines of evidence suggest that the catalytic mechanism for **1A** and **1B** is not cross-coupling of two Co^{3+}-O● moieties. From this we conclude that intramolecular O-O bond distance is the primary structural feature needed for water oxidation by cobalt *dimers*.

We propose that efficient hole delocalization, which facilitates buildup of oxidizing equivalents on cobalt, is the defining property of catalysis from the Co_4O_4 cubane. This is

emphasized for **1A** in acetonitrile, where an electron can be removed electrochemically from the core at ca. 0.7 V vs. Ag/AgCl, reversibly forming Co_4(3III,IV). In contrast, electrochemical hole injection into either **2A** or **3A** is not seen up to 1.5 V vs. Ag/AgCl (Figure 2.22).

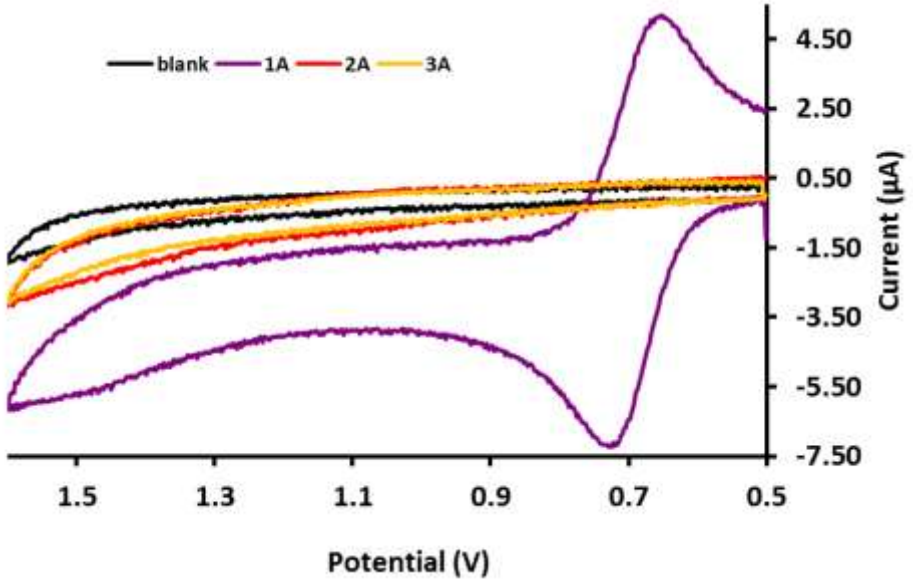

Figure 2.22: CV of pyridine materials in 0.1M tetrabutylammonium perchlorate/MeCN. Cluster concentrations: **1A** 1.15mM, **2A** 1.06mM, **3A** 1.14mM. Working electrode: platinum; counter electrode; platinum; reference electrode; Ag/AgCl

This effect we believe is more intrinsic to the core type as opposed to the varying cluster charge (**1A** is neutral, **2A** and **3A** are cations) because the 2+ cation **1B** is also reversibly oxidized within this window (Figure 2.4).

Our proposed mechanism presented in Scheme 2.3 accounts for our experimental observations and highlights the effective hole delocalization properties of the cubane structure. The first-order pathway is assigned to oxidation of cubane **1** by Ru^{3+}; this occurs quickly (10^7 $(M^*s)^{-1}$)[14] and hence $[1]_o \approx [1^+]$. Due to the known properties of $\mathbf{1}^+$ with both ligand sets, the hole is delocalized across the core, though we depict this in the form of resonance where the hole lies on a cobalt (A) or an oxo bridge (B). Generation of a terminal hydroxide at a carboxylate site then occurs (C), which gives an intermediate that is also accessible via attack by (persulfate generated) ●OH in the proposed zeroth-order pathway (D).

Experimental and computational results suggest that a range of potentials for oxidation of a catalyst containing Co^{4+}-OH is 1.4-1.5 V vs. SHE[45,48,50], which is too high for $Ru(bpy)_3^{3+}$ (1.26 V), but not $SO_4^{\bullet-}$ (2.4 V). Thus, the sulfate radical is the only oxidant of sufficient strength to perform the next PCET step on the terminal hydroxide, and a base is required to remove the proton. Depending on resonance, this gives (formally) a terminal Co^{4+}-O● (E), or one bridging and one terminal O● connected by a Co^{3+} center (F). The O-O bond formation step thus proceeds via nucleophilic attack of hydroxide in the former case, or oxo-oxyl radical coupling in the latter case. We do not yet have single turnover ^{18}O data that might distinguish these pathways, but we note that the need for a base in our system suggests either one or two oxo substrates originate from bulk water. For either

peroxo product, subsequent two electron oxidation would generate the O_2 product and regenerate the starting Co_4O_4 cubane.

The oxo-oxyl radical coupling mechanism (F) in particular has been proposed by our group to occur in Photosystem II[55], and is favored in recent EPR studies[56]. This mechanism may account for the isotope labelling studies which found oxos from the Co-Pi catalyst incorporated into product O_2[57]. Depending on the resonance stabilization observed in the cubane, either or both mechanisms may occur simultaneously.

As a final note, **1A** and **1B** compare to the structurally similar $Co^{II}_4(hmp)_4(\mu\text{-}OAc)_2(H_2O)_2$ (hmp= 2-hydroxymethyl pyridine) cubane catalyst, but have lower TOFs under similar conditions[58]. A similar derivative to **1A** has been demonstrated to last for three times as many turnovers[15]. We ascribe the slower rates of catalysis from **1A** and **1B** as due to the need to displace an acetate ligand in order to generate a terminal oxo, as precursor to O_2 evolution. However, the ligand environment of **1A** allows for greater catalyst longevity as the terminal aquo form is unstable towards decomposition which results in lower turnover numbers.

Scheme 2.3. Proposed mechanism for water oxidation by the Co_4O_4 cubane (this work).

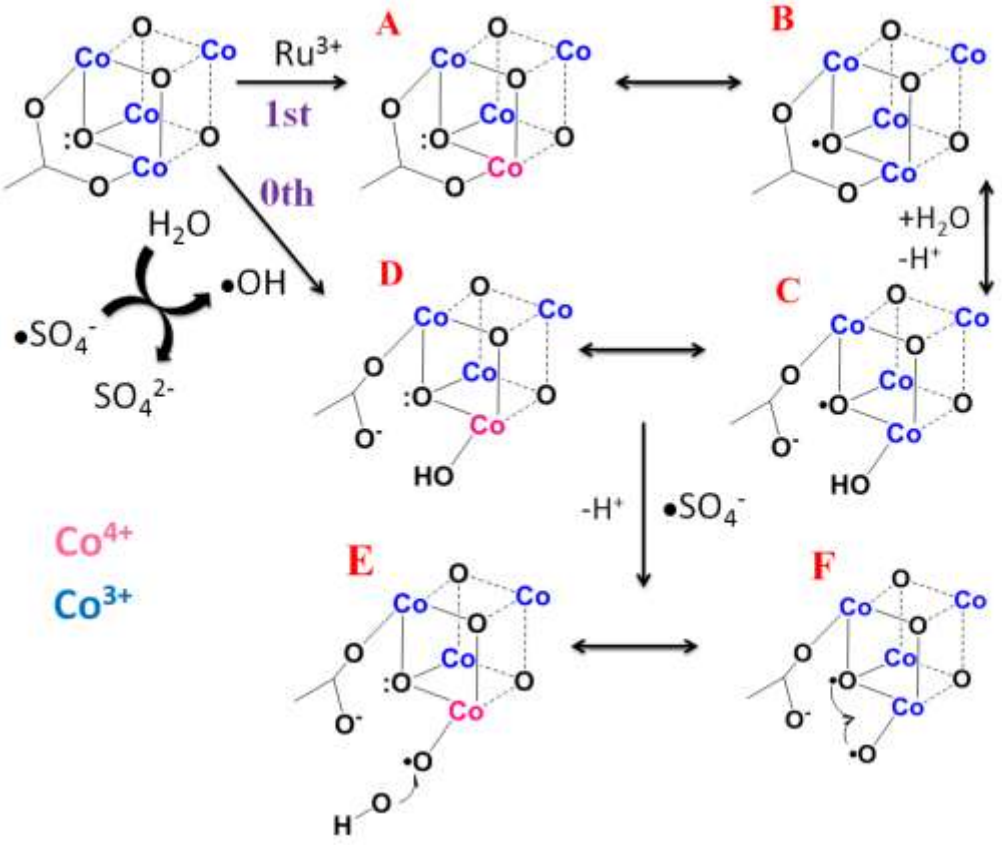

2.6 Conclusion

The molecular clusters studied herein represent discrete models of various cobalt oxide water oxidation catalysts including the solid state spinels. In particular, we have compared the Co_4O_4 cubane structure with smaller subclusters, including Co_2O_2 and $Co_3O_{3,4}$ cores, and conclude based on multiple lines of evidence that none of these smaller subclusters is catalytically active for O_2 evolution from water. The origin of catalytic activity by Co_4O_4 cubanes illustrates three key features for water oxidation: 1) four one-electron redox metals, 2) efficient charge delocalization of the first oxidation step across the Co_4O_4 cluster, allowing for stabilization of higher oxidizing equivalents, and 3) terminal coordination site for substrate aquo/oxo formation.

Our findings also illustrate the complexity of the $Ru(bpy)_3^{2+}/S_2O_8^{2-}$ photoassay, since we have shown that persulfate and buffer are both necessary for catalysis outside of their "standard' roles as sacrificial electron and proton acceptors, respectively.

2.7Acknowledgments

We thank Clyde Cady, Anders Laursen, David Vinyard and Jennifer Sun for discussions, Nagarajan Murali and Gennady Ananyev for instrument support. This work was supported by the Air Force Office of Scientific Research (Grant # FA9550-11-1-0231). We acknowledge partial support from an NSF IGERT fellowship, the Rutgers University Aresty Research Center, Rutgers Energy Institute, and Rutgers University.

2.8 References

[1] C. A. Kent, J. J. Concepcion, C. J. Dares, D. A. Torelli, A. J. Rieth, A. S. Miller, P. G. Hoertz, T. J. Meyer, *J. Am. Chem. Soc.* **2013**, *135*, 8432–8435.

[2] K. J. Young, L. A. Martini, R. L. Milot, R. C. Snoeberger Iii, V. S. Batista, C. A. Schmuttenmaer, R. H. Crabtree, G. W. Brudvig, *Coord. Chem. Rev.* **2012**, *256*, 2503–2520.

[3] X. Lin, X. Hu, J. J. Concepcion, Z. Chen, S. Liu, T. J. Meyer, W. Yang, *Proc. Natl. Acad. Sci.* **2012**, DOI 10.1073/pnas.1118344109.

[4] Y. Gao, R. H. Crabtree, G. W. Brudvig, *Inorg. Chem.* **2012**, *51*, 4043–4050.

[5] W. C. Ellis, N. D. McDaniel, S. Bernhard, T. J. Collins, *J. Am. Chem. Soc.* **2010**, *132*, 10990–10991.

[6] S. M. Barnett, K. I. Goldberg, J. M. Mayer, *Nat Chem* **2012**, *4*, 498–502.

[7] Z. Chen, T. J. Meyer, *Angew. Chemie Int. Ed.* **2013**, *52*, 700–703.

[8] K. S. Joya, J. L. Vallés-Pardo, Y. F. Joya, T. Eisenmayer, B. Thomas, F. Buda, H. J. M. de Groot, *Chempluschem* **2013**, *78*, 35–47.

[9] Q. Yin, J. M. J. M. Tan, C. Besson, Y. V Geletii, D. G. Musaev, A. E. Kuznetsov, Z. Luo, K. I. Hardcastle, C. L. Hill, *Science (80-.).* **2010**, *328*, 342–345.

[10] L. Duan, F. Bozoglian, S. Mandal, B. Stewart, T. Privalov, A. Llobet, L. Sun, *Nat. Chem.* **2012**, 1–6.

[11] Y. Umena, K. Kawakami, J.-R. Shen, N. Kamiya, *Nature* **2011**, *473*, 55–60.

[12] A. Sartorel, M. Bonchio, S. Campagna, F. Scandola, *Chem. Soc. Rev.* **2013**, *42*, 2262–2280.

[13] N. S. McCool, D. M. Robinson, J. E. Sheats, G. C. Dismukes, *J. Am. Chem. Soc.* **2011**, *133*, 11446–11449.

[14] G. La Ganga, F. Puntoriero, S. Campagna, I. Bazzan, S. Berardi, M. Bonchio, A. Sartorel, M. Natali, F. Scandola, *Faraday Discuss.* **2012**, *155*, 177–190.

[15] S. Berardi, M. Natali, I. Bazzan, F. Puntoriero, A. Sartorel, F. Scandola, S. Campagna, M. Bonchio, *J. Am. Chem. Soc.* **2012**, *134*, 11104–11107.

[16] G. F. Swiegers, J. K. Clegg, R. Stranger, *Chem. Sci.* **2011**, *2*, 2254–2262.

[17] F. Jiao, H. Frei, *Angew. Chemie-International Ed.* **2009**, *48*, 1841–1844.

[18] D. M. Robinson, Y. B. Go, M. Greenblatt, G. C. Dismukes, *J. Am. Chem. Soc.* **2010**, *132*, 11467–11469.

[19] G. P. Gardner, Y. B. Go, D. M. Robinson, P. F. Smith, J. Hadermann, A. Abakumov, M. Greenblatt, G. C. Dismukes, *Angew. Chemie* **2012**, *124*, 1648–1651.

[20] M. W. Kanan, J. Yano, Y. Surendranath, M. Dinca, V. K. Yachandra, D. G. Nocera, *J. Am. Chem. Soc* **2010**, *132*, 13692–13701.

[21] M. Risch, V. Khare, I. Zaharieva, L. Gerencser, P. Chernev, H. Dau, *J. Am. Chem. Soc* **2009**, *131*, 6936–6937.

[22] P. Du, O. Kokhan, K. W. Chapman, P. J. Chupas, D. M. Tiede, *J. Am. Chem. Soc.* **2012**, *134*, 11096–11099.

[23] K. Dimitrou, K. Folting, W. E. Streib, G. Christou, *J. Am. Chem. Soc.* **1993**, *115*, 6432–6433.

[24] R. Chakrabarty, S. J. Bora, B. K. Das, *Inorg. Chem.* **2007**, *46*, 9450–9462.

[25] C. E. Sumner, *Inorg. Chem.* **1988**, *27*, 1320–1327.

[26] K. Dimitrou, K. Folting, W. E. Streib, G. Christou, *J. Am. Chem. Soc.* **1993**, *115*, 6432–6433.
[27] K. Dimitrou, A. D. Brown, K. Folting, G. Christou, *Inorg. Chem.* **1999**, *38*, 1834–1841.
[28] K. Dimitrou, A. D. Brown, T. E. Concolino, A. L. Rheingold, G. Christou, *Chem. Commun.* **2001**, 1284–1285.
[29] D. Shevchenko, M. F. Anderlund, A. Thapper, S. Styring, *Energy Environ. Sci.* **2011**, *4*, 1284–1287.
[30] S. Tanaka, M. Annaka, K. Sakai, *Chem. Commun.* **2012**, *48*, 1653–1655.
[31] D. J. Wasylenko, R. D. Palmer, E. Schott, C. P. Berlinguette, *Chem. Commun.* **2012**, *48*, 2107.
[32] M. Natali, S. Berardi, A. Sartorel, M. Bonchio, S. Campagna, F. Scandola, *Chem. Commun.* **2012**, *48*, 8808–8810.
[33] J. J. Stracke, R. G. Finke, *J. Am. Chem. Soc.* **2011**, *133*, 14872–14875.
[34] B. S. Brunschwig, M. H. Chou, C. Creutz, P. Ghosh, N. Sutin, *J. Am. Chem. Soc.* **1983**, *105*, 4832–4833.
[35] V. Artero, M. Fontecave, *Chem. Soc. Rev.* **2013**, *42*, 2338–2356.
[36] J. W. Vickers, H. Lv, J. M. Sumliner, G. Zhu, Z. Luo, D. G. Musaev, Y. V Geletii, C. L. Hill, *J. Am. Chem. Soc.* **2013**, *135*, 14110–14118.
[37] J. J. Stracke, R. G. Finke, *ACS Catal.* **2013**, *3*, 1209–1219.
[38] M. Hara, C. C. Waraksa, J. T. Lean, B. A. Lewis, T. E. Mallouk, *J. Phys. Chem. A* **2000**, *104*, 5275–5280.
[39] M. D. Symes, Y. Surendranath, D. a. Lutterman, D. G. Nocera, *J. Am. Chem. Soc.* **2011**, *133*, 5174–5177.
[40] A. R. Parent, R. H. Crabtree, G. W. Brudvig, *Chem. Soc. Rev.* **2013**, *42*, 2247–2252.
[41] R. H. Waldemer, P. G. Tratnyek, R. L. Johnson, J. T. Nurmi, *Environ. Sci. Technol.* **2006**, *41*, 1010–1015.
[42] P. Sarmah, R. Chakrabarty, P. Phukan, B. K. Das, *J. Mol. Catal. A Chem.* **2007**, *268*, 36–44.
[43] J. G. McAlpin, T. A. Stich, C. A. Ohlin, Y. Surendranath, D. G. Nocera, W. H. Casey, R. D. Britt, *J. Am. Chem. Soc.* **2011**, *133*, 15444–15452.
[44] M. L. Rigsby, S. Mandal, W. Nam, L. C. Spencer, A. Llobet, S. S. Stahl, *Chem. Sci.* **2012**, *3*, 3058.
[45] D. J. Wasylenko, C. Ganesamoorthy, J. Borau-Garcia, C. P. Berlinguette, *Chem. Commun.* **2011**, *47*, 4249–4251.
[46] C.-F. Leung, S.-M. Ng, C.-C. Ko, W.-L. Man, J. Wu, L. Chen, T.-C. Lau, *Energy Environ. Sci.* **2012**, *5*, 7903.
[47] E. Pizzolato, M. Natali, B. Posocco, A. Montellano Lopez, I. Bazzan, M. Di Valentin, P. Galloni, V. Conte, M. Bonchio, F. Scandola, et al., *Chem. Commun.* **2013**, *49*, 9941–9943.
[48] D. Wang, J. T. Groves, *Proc. Natl. Acad. Sci.* **2013**, *110* , 15579–15584.
[49] D. K. Dogutan, R. McGuire, D. G. Nocera, *J. Am. Chem. Soc.* **2011**, *133*, 9178–9180.
[50] L. P. Wang, T. Van Voorhis, *J. Phys. Chem. Lett.* **2011**, *2*, 2200–2204.

[51] F. A. Chavez, J. M. Rowland, M. M. Olmstead, P. K. Mascharak, *J. Am. Chem. Soc.* **1998**, *120*, 9015–9027.
[52] F. A. Chavez, P. K. Mascharak, *Acc. Chem. Res.* **2000**, *33*, 539–545.
[53] J. Zhang, A. V Biradar, S. Pramanik, T. J. Emge, T. Asefa, J. Li, *Chem. Commun.* **2012**, *48*, 6541–6543.
[54] T. Stich, J. Krzystek, B. Q. Mercardo, J. G. McAlpin, C. A. Ohlin, M. M. Olmstead, W. H. Casey, R. D. Britt, *Polyhedron* **2013**, *64*, 304–307.
[55] D. J. Vinyard, G. M. Ananyev, G. C. Dismukes, *Annu. Rev. Biochem.* **2013**, *82*, 577–606.
[56] M. Pérez Navarro, W. M. Ames, H. Nilsson, T. Lohmiller, D. a Pantazis, L. Rapatskiy, M. M. Nowaczyk, F. Neese, A. Boussac, J. Messinger, et al., *Proc. Natl. Acad. Sci.* **2013**, *110* , 15561–15566.
[57] Y. Surendranath, M. W. Kanan, D. G. Nocera, *J. Am. Chem. Soc* **2010**, *132*, 16501–16509.
[58] F. Evangelisti, R. Güttinger, R. Moré, S. Luber, G. R. Patzke, R. Guettinger, R. More, S. Luber, G. R. Patzke, R. Güttinger, et al., *J. Am. Chem. Soc.* **2013**, 18734–18737.

Chapter 3 Water Oxidation by the $[Co_4O_4(OAc)_4(py)_4]^+$ Cubium is Initiated by OH^- Addition

3.1Abstract

The cobalt cubium $Co_4O_4(OAc)_4(py)_4(ClO_4)$ (**1A+**) containing the mixed valence $[Co_4O_4]^{5+}$ core is shown by multiple spectroscopic methods to react with hydroxide (OH^-) but not with water (H_2O) to produce O_2. The yield of reaction products is stoichiometric (>99.5%): 4 $\mathbf{1A}^+$ + 4 OH^- → O_2 + 2 H_2O + 4 **1A**. EPR spectroscopy demonstrates no free Co^{2+} or Co_3O_4 participates or forms. Mass spectrometry of the reaction between isotopically labeled μ-^{16}O(bridging-oxo) $\mathbf{1A}^+$ and ^{18}O-bicarbonate/water shows: 1) no exchange of ^{18}O into the bridging oxos of $\mathbf{1A}^+$, and 2) $^{36}O_2$ is the major product and likely forms via rearrangement or displacement of an acetate ligand by OH^-. NMR indicates that 0.5% ligands (Py and OAc-) are released following the O_2 evolution reaction between $\mathbf{1A}^+$ and OH^-. DFT calculations of solvated intermediates indicate a mechanism of successive addition of two OH^- to $\mathbf{1A}^+$ via carboxylate rearrangements and oxidation to form intermediate $[1A(OH)_2]^+$, is an energetically preferred intermediate to further oxidation by $\mathbf{1A}^+$ and O_2 formation. Collectively, these data indicate that water oxidation must be preceded by inner sphere insertion of OH^- to Co-OAc- bond to form a more readily oxidizable inner-sphere complex that serves as catalyst for O2 formation by outer sphere electron transfer to remaining cubium as oxidant. These results, and recent literature (Faraday Discussions, doi:10.1039/C5FD00076A) validate organometallic $[Co_4O_4]^{4+/5+}$ cubane **1A** as a catalyst for water oxidation.

3.2 Introduction

Sustainable production of hydrogenic fuels requires an abundant source of hydrogen. Water is the ideal source of hydrogen, but must first be cleaved by an energetic process in which 4 strong O-H bonds are broken. Towards this goal, several heterogeneous cobalt oxide catalysts for electrochemical water oxidation have been reported[1–6] and widely applied[7–18]. Rational design of heterogeneous catalysts is difficult, and can significantly benefit from understanding gained from simpler homogenous catalysts. To better understand their basis for catalysis, several molecular cobalt clusters have been synthesized and reported to be active homogenous catalysts[19–29]. The most active catalysts among these organometallic clusters contain a Co_4O_4 "cubane" core[30,31], which is a recurring structural theme among biological and synthetic water oxidation catalysts[32,33]. Many studies have described the properties[34–47] of $Co_4O_4(OAc)_4(py)_4$, **1A**, and $[Co_4O_4(OAc)_2(bpy)_4](ClO_4)_2$, $\mathbf{1B}^{2+}(ClO_4)_2$ (Scheme 3.1).

The synthesis and characterization of cubane **1A** has an extensive history. Oxidation of Co^{2+} acetate by peroxide or peracetic acid was known to give a complex, equilibrating, reaction mixture, until the addition of pyridine allowed isolation of dimeric and trimeric cobalt cations[48]. Cubane **1A**, which is neutral and has high solubility in many solvents, escaped detection from this synthesis until many years later[47]. Other studies targeted formation of the cubane using alternate carboxylates and substituted pyridines to shift the equilibrium[38], though the general synthetic method remained similar. These later reports served as the basis for the preparation of **1A** by several groups including ourselves, who all showed **1A** (and close analogs) to be an active water oxidation catalyst[49–55]. DFT calculations further confirmed energetically accessible routes to catalytic O_2 evolution

from model Co_4O_4 cubanes (terminated by water ligands), though with preference for different mechanisms[56,57].

Scheme 3.1. Cubanes: $Co_4O_4(OAc)_4(py)_4$, 1A, and $[Co_4O_4(OAc)_2(bpy)_4]^{2+}$, $1B^{2+}$

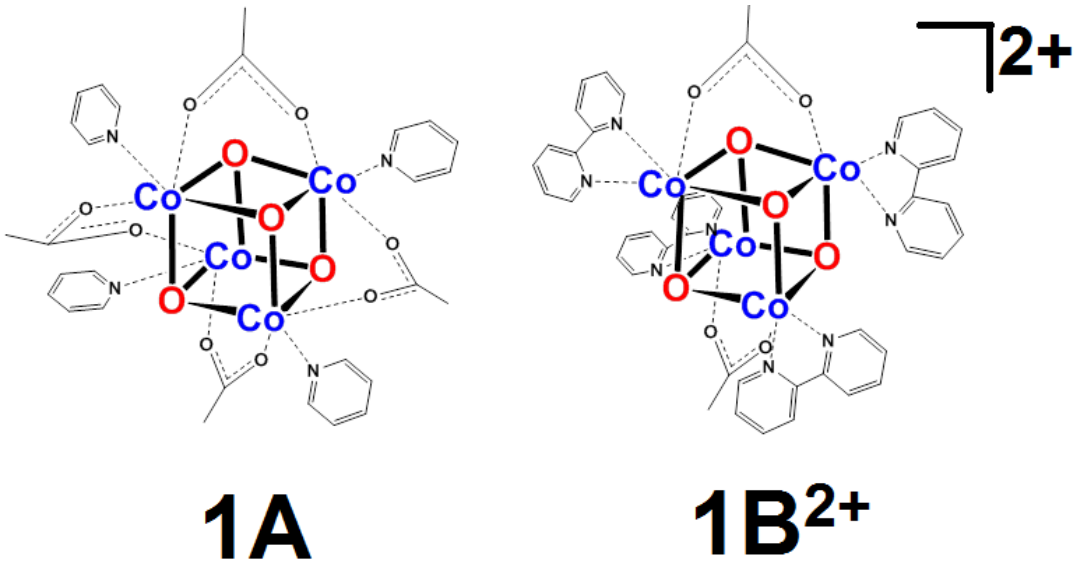

Recently, Nocera et al. provided strong evidence that Co^{2+} impurities remaining from synthesis form the main catalyst when oxidized in phosphate buffer either electrochemically or *via* a Ru^{3+} photo-oxidant[58]. From that report, pristine **1A** was found inactive for electrochemical water oxidation. While the pure compound was photochemically active, catalysis was ascribed to decomposition products. More recently, Bonchio et al. showed by kinetic studies that **1A** minus an acetate ligand is the most likely intrinsic water oxidation catalyst in the photochemical assay[59]. This derivative is accessible by aging **1A** in water.

Hence, cubane **1A** must rearrange or dissociate ligands to bind water to Co[44,54] . The present work reconciles these recent contradictions by demonstrating for the first time that the oxidized cubium **1A**ClO_4 reacts with OH^- to release O_2 spontaneously *in the dark without adding any external oxidants.* The oxidizing equivalents originate from the intact (fully ligated) cubiums (1.25 V vs. NHE) which are reduced in 99.5% yield to **1A**. The active catalyst is the ligand-labilized or ligand-dissociated cubium itself, as evidenced by NMR and mass spectrometry. These tools show 0.5% total starting ligands as unbound in the postreaction solution, consistent with facile carboxylate exchange reported previously[35,40]**.** Consistent with experiments, DFT calculations quantify the favorable energetics of OH^- addition and the favorable oxidation potential of the bis-hydroxo species relative to **1A**$^+$**/1A**. These results affirm that the $[Co_4O_4]^{4+/5+}$ molecular cubane core is indeed precursor to an efficient water oxidation catalyst, following activation by hydroxide binding. Paramagnetic Co^{2+} impurities are rigorously excluded as the source of any catalytic potential. The data presented herein allow renewed confidence in the use of organometallic cubanes as models for heterogenous catalysts.

3.3 Experimental

Materials and Methods. All solutions were prepared with reagent grade water (18 MΩ, Hydro Picopure). All solvents and reagents were reagent grade, purchased commercially and used without further purification. $NaH^{13}C^{18}O_3$ bicarbonate was used to induce formation of $^{18}OH^-$ in experiments requiring isotopic labeling. ^{18}O water was purchased as 97% from Aldrich or 98% from Icon Isotopes. UV-Vis spectra were recorded on an HP-8452A Diode Array spectrophotometer in standard 1 cm pathlength quartz cells. EPR spectra were recorded on a Bruker ESP300 spectrometer equipped with Oxford cryostat model 900 at 10K. Samples were glasses of $\mathbf{1A}^+$ in acetonitrile and $\mathbf{1B}^+$ in 1M H_2SO_4. A CH Instruments Electrochemical Workstation was used for exhaustive electrolysis experiments.

A Clark type oxygen electrode (Hansatek Ltd) was used to obtain oxygen evolution data, and calibrated daily using N_2 deoxygenated and oxygen saturated atmospheric solutions. Clark electrode experiments were performed by monitoring the addition of 20µL of 1M NaOH to 500µL of 95/5 H_2O/CH_3CN solutions of $\mathbf{1A}^+$**.** The initial rates were obtained by determining the slope over the beginning linear region (~10s) of O_2 evolution.

Gas chromatography data were recorded on a Perkin Elmer Clarus 680 GC with a TCD detector (Ar carrier gas) operating at 40ºC (O2) or 200ºC (CO2). Gas chromatography experiments monitored the addition of 200 µL of Ar-degassed 0.1 M NaOH to solid powders of $\mathbf{1A}^+$ or $\mathbf{1B}^{3+}$ in Ar-degassed 2 mL vials, and were adjusted using the N_2 signal as a control.

Membrane Inlet Mass Spectroscopy data were taken with a Stanford Research Systems CIS100 residual gas analyzer. A 1/16" capillary partially submerged in a dry ice/ethyleneglycol/ethanol trap @ -40ºC was used to connect the CIS to a KF/Swagelok adapter, in which sat a porous polyethylene support, a 12.5 µm Teflon membrane (Hansatech), and an O-ring. This assembly was clamped to the KF connection of a glass reaction vessel. Solid **1A**$^+$ and ^{18}O bicarbonate were placed on top of the membrane while the vessel was Ar-purged, and ^{18}O was Ar-purged in its container as delivered. When ^{18}O water was added by syringe, nitrogen, CO_2 (labeled and unlabeled) and Argon were monitored in addition to the O_2 isotopes as control signals; the $^{32}O_2$ and $^{34}O_2$ signals were adjusted from the residual N_2 signal in the resulting data. The $^{36}O_2$ signal was adjusted from the background Ar signal in the resulting data. All O_2 signals adjust for separate background signals before injection. For MS data>100 amu, spectra were recorded by direct injection of nM samples via syringe pump into an Agilent 6510 QTOF LC/MS running in dual ESI mode.

Syntheses. 1A was prepared as previously described[49,54]. Purification was performed by collecting the first, green fraction off a column of silica gel using 5% methanol/dichloromethane mobile phase. **1AClO_4 (1A$^+$)** was made by bulk electrolysis (1.1-1.2V) of a 0.4M $LiClO_4/CH_3CN$ solution of **1A**, followed by reduction of solvent volume to ~5ml by rotary evaporation, addition of water (~35 ml), and overnight refrigeration, giving a precipitate collected by filtration in 10-15% yield. A porous carbon rod (working), Ti wire (counter) and silver wire (pseudoreference) were used as electrodes; the latter two electrodes were compartmentalized in fritted glass tubes (Ace

glass) filled only with blank electrolyte (no cobalt). **1A**$^{+}$ as the PF_6 salt was prepared exactly as described in ref[58].

1B^{2+} as a perchlorate salt was prepared as described previously[54]. **1B**$^{3+}$ was isolated in two ways, as a tri-perchlorate salt **1B(ClO4)3** which precipitates following CH3CN electrolysis at 1.5 V vs. Ag pseudoreference; alternately, as a cerium salt **1BCe(NO3)6** as the precipitate formed following the CH3CN reaction of **1B** with excess cerium ammonium nitrate.

3.4 Results

After performing column chromatography on samples of cubane **1A**, we observed no noticeable water oxidation current above a background glassy carbon electrode in buffered water (0.1 M phosphate buffer at pH 7) (Figure 3.1), consistent with the pure samples isolated by Nocera, et. al[58]. We adapted two literature procedures to synthesize $\mathbf{1A}^+$: 1) electrochemical oxidation[44], yielding the ClO_4 salt; 2) chemical oxidation[58], yielding the PF_6 salt. The following results are all consistent regardless of preparation method.

The EPR spectrum of $\mathbf{1A}^+$ dissolved in water/acetonitrile glass forming solvent is comparable to the initial report[44] (Figure 3.2). Specifically, the line shape and Curie temperature dependence indicate a spin S = ½ ground state with an axial g tensor, $g_{\parallel}$ =2.06 and $g_{\perp}$=2.28. There is no resolved hyperfine structure from ^{59}Co (I = 7/2, 100% n.a.) and no features at lower field where species of higher spin multiplicity can absorb. The sample (up to 15 mM concentration) exhibits no EPR signal for Co^{2+} or for that matter any paramagnetic impurity. $\mathbf{1A}^+$ as isolated is not water soluble, but dissolves in aqueous solutions of NaOH, N-butylammonium hydroxide, sodium bicarbonate, and sodium carbonate. As monitored by EPR and UV-Vis spectroscopies the addition of any of these hydroxide sources to $\mathbf{1A}^+$/CH_3CN solutions results in reduction to diamagnetic **1A** (Figures 3.2 and 3.3, respectively). Bubbles are released upon this reaction and confirmed as O_2 by Clark electrode, gas chromatography and membrane inlet mass spectrometry (*vide infra*).

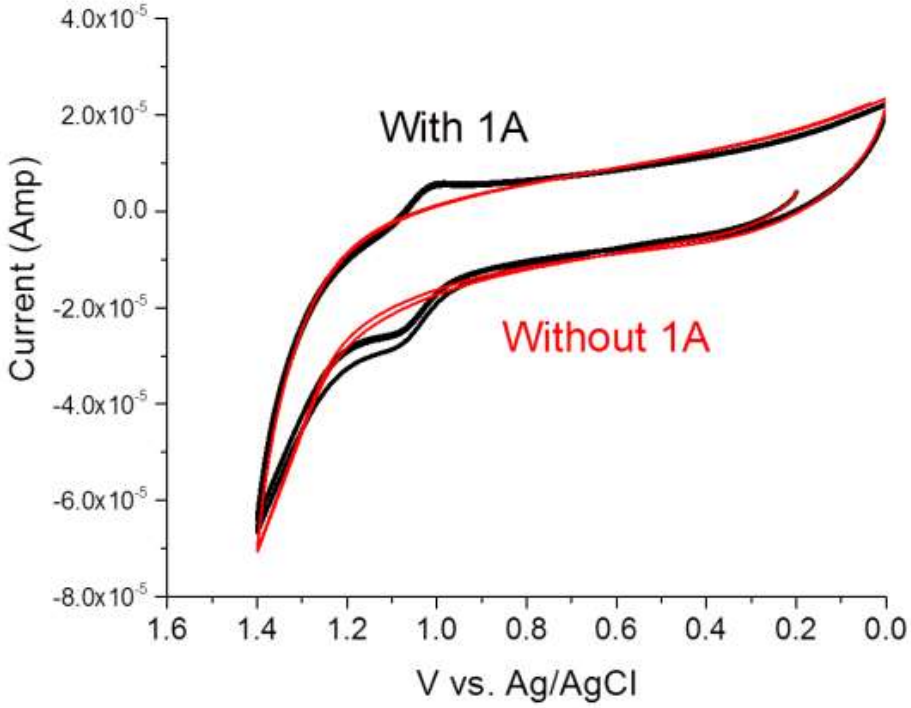

Figure 3.1. Cyclic voltammograms at a glassy carbon electrode in aqueous phosphate (0.1M, pH 7) with and without 500 μM of **1A.**

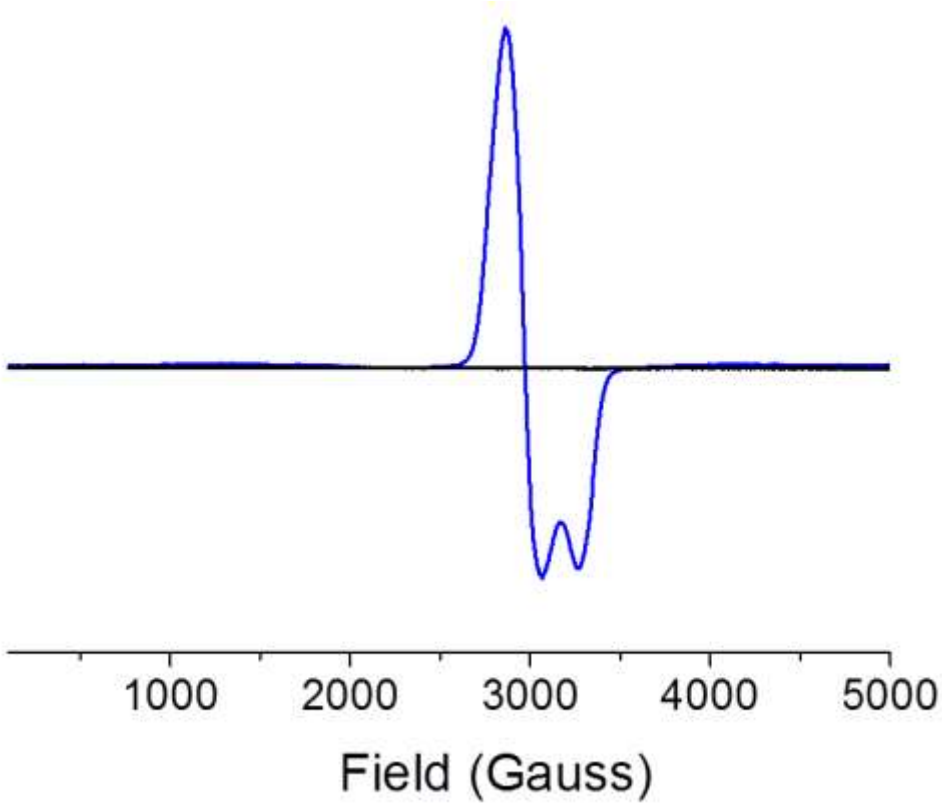

Figure 3.2. EPR spectrum at 10 K of 15 mM CH_3CN solutions of **1A(ClO_4)** without (blue) and with (black) 0.1 M NaOH.

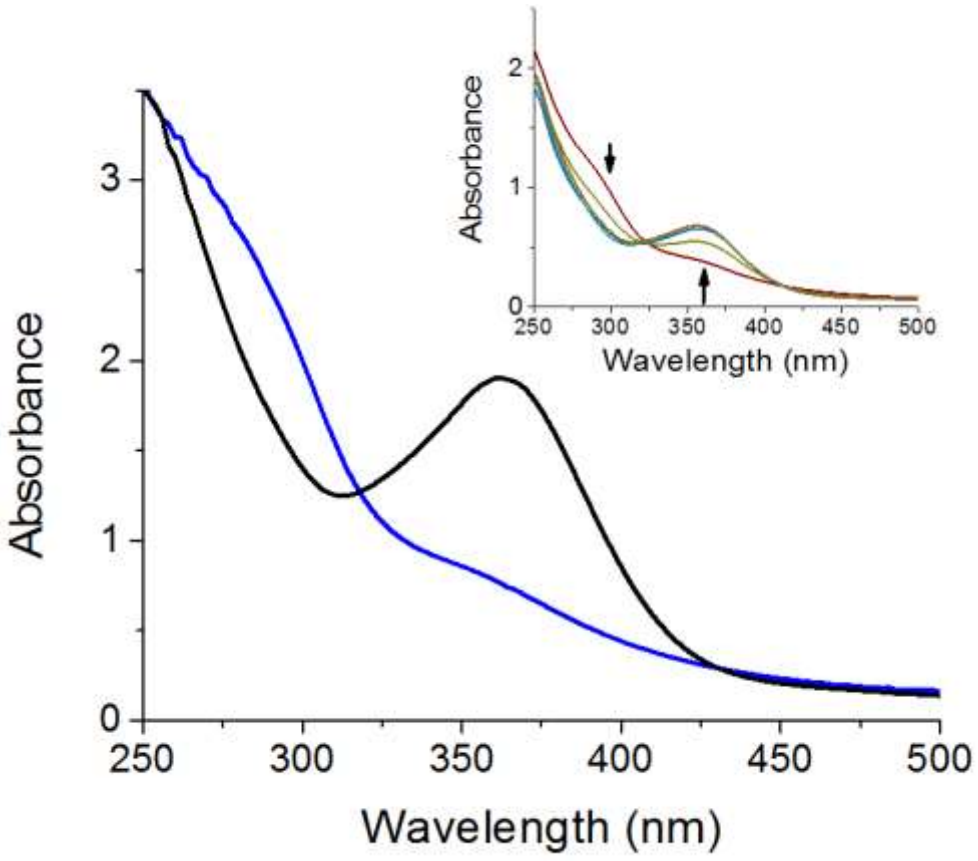

Figure 3.3. UV-Vis spectra of 170 μM CH_3CN solutions of $1A^+$ (blue) and 1A (black). Inset: Spectral changes following addi-tion of 4x0.5 eq. aliquots of OH- to 60 μM of $1A^+$.

UV-Vis titrations indicated 1:1 stoichiometry of cubium to hydroxide completes the reaction (Figure 3.3, inset, and Figure 3.4). Given that **1A**$^{+}$ precipitates from water in the last step of synthesis, no reaction with water was anticipated, as confirmed by control experiments over the time scale of several minutes (Figure 3.4). Control measurements without **1A**$^{+}$ or OH^{-} produced no measureable O_2 in all these trials.

Gas chromatography was used to quantify the O_2 produced upon complete dissolution of 2-2.5 µmol of **1A(ClO$_4$)** in 10 eq. aqueous NaOH. The amount of O_2 produced was quantitatively consistent with reduction of $4Co^{4+}$ to $4Co^{3+}$ (O_2:**1A**$^{+}$ ratio of 0.27 ±0.03). Consistent with this result, EPR spectroscopy of the reaction product solutions showed no identifiable paramagnetic Co^{2+} (Figure 2, black trace); suggesting only Co^{3+}in the product. We did not observe CO_2 or CO in the product gas above GC detection (< 10 nmol, 0.5%), consistent with no oxidation of substrates other than OH^{-}. Hence, the reaction stoichiometry is given by eqn (1):

$$4\ \mathbf{1A}^{+} + 4\ OH^{-} \rightarrow O_2 + 4\ \mathbf{1A} + 2\ H_2O \qquad (1)$$

As determined by Clark electrode, the method of initial rates indicates that the O_2 evolution reaction is first order in both cubium and OH^{-} over the concentration range 0-1 mM. (Figure 3.5). Rates decrease from linear dependence at $[OH^{-}]$> 1 mM. A plot of the pseudo-first order constants vs. $[OH^{-}]$ gives the bimolecular rate constant k= 1.1 $(M*s)^{-1}$ for the reaction, (eqn. 2).

$$d[O_2]/dt = k\ [\mathbf{1A}^{+}]\ [OH^{-}]\ ,\ k = 1.1\ /\ M*s \qquad (2)$$

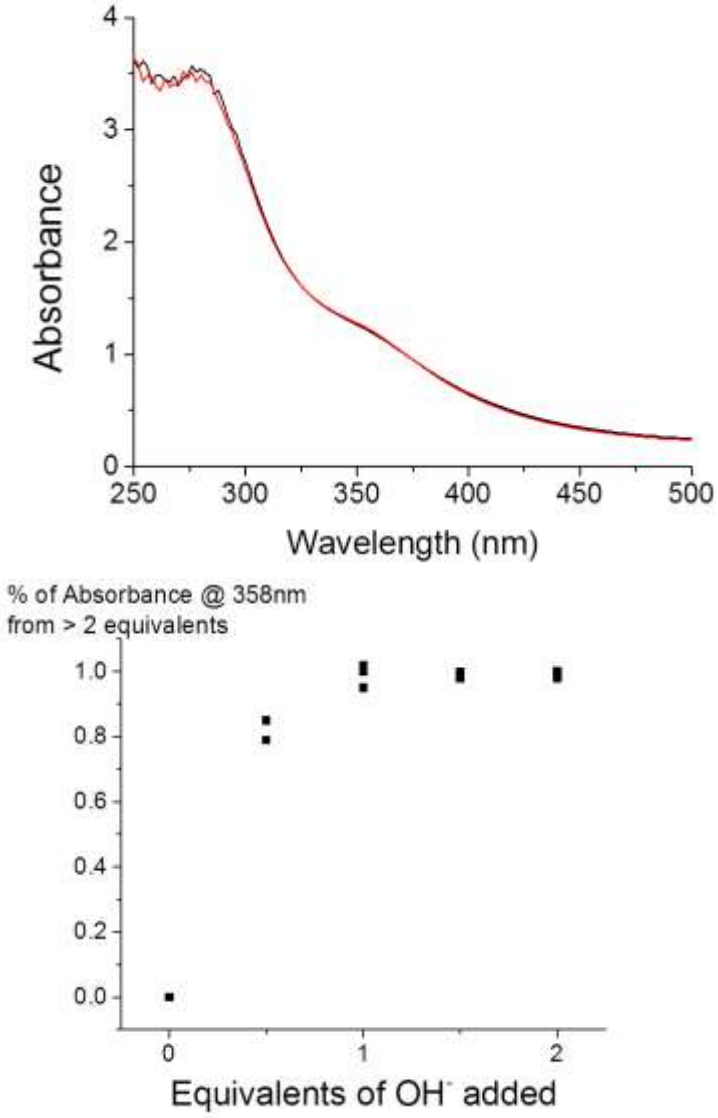

Figure 3.4: Top: Aging a solution of **1A**$^+$ in 1:1 CH_3CN:H_2O for 15 minutes (start=black, 15 minutes=red). Bottom: The percentage completion of the reaction as a function of equivalents of OH^- added, as measured by UV-Vis, 3 trials are plotted discretely. The reaction is assumed to have not started at 0 equivalents.

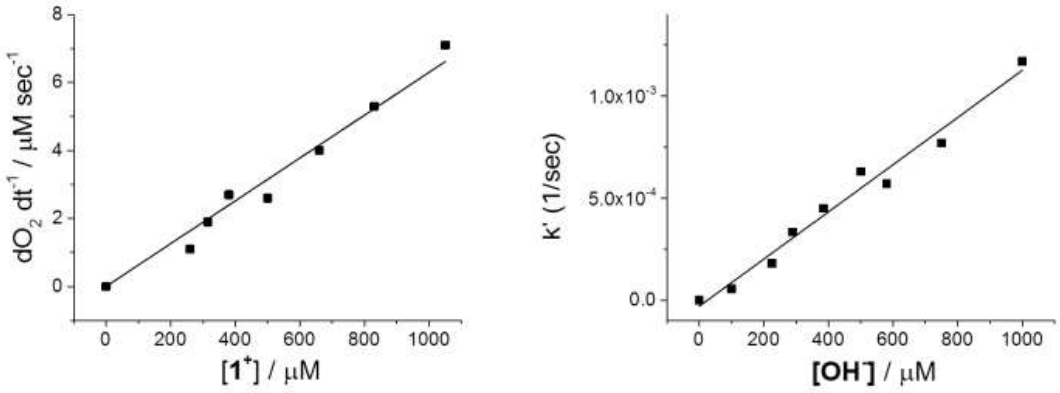

Figure 3.5. Left: Initial rate of O_2 production as a function of initial [**1A**$^+$] in the presence of 40 mM NaOH. Right: Pseudo-first order rate constants as a function of OH^-, [$1A^+$] =2mM.

The fates of the OAc^- and py ligands after reaction were monitored by ^{1}H-NMR spectroscopy. The pyridine region of the ^{1}H-NMR spectrum of **1A**$^+$ in CD_3CN consists of a single broad peak, owing to the paramagnetic broadening of this material (Figure 3.6A). Upon addition of 4 eq. hydroxide (Figure 3.6C) the resulting spectrum most prominently contains sharp pyridine resonances that match those of **1A** (Figure 3.6B). Free pyridine and acetate resonances are observed above NMR detection limit only when using 1.5 mM or higher cubium concentrations (Figure 3.6C and Figure 3.7 respectively). Integration of the free:bound ligand ratio indicated 99.5% of ligands (py and OAc) remain bound to cubane **1A**. Free ligands were not seen in previous studies, which utilized cubane concentrations 5-150x less than that used here[49,54]. Collectively, these data suggest that the stoichiometric reduction reaction between cubium and OH- proceeds via ligand dissociation or exchange of acetate and pyridine.

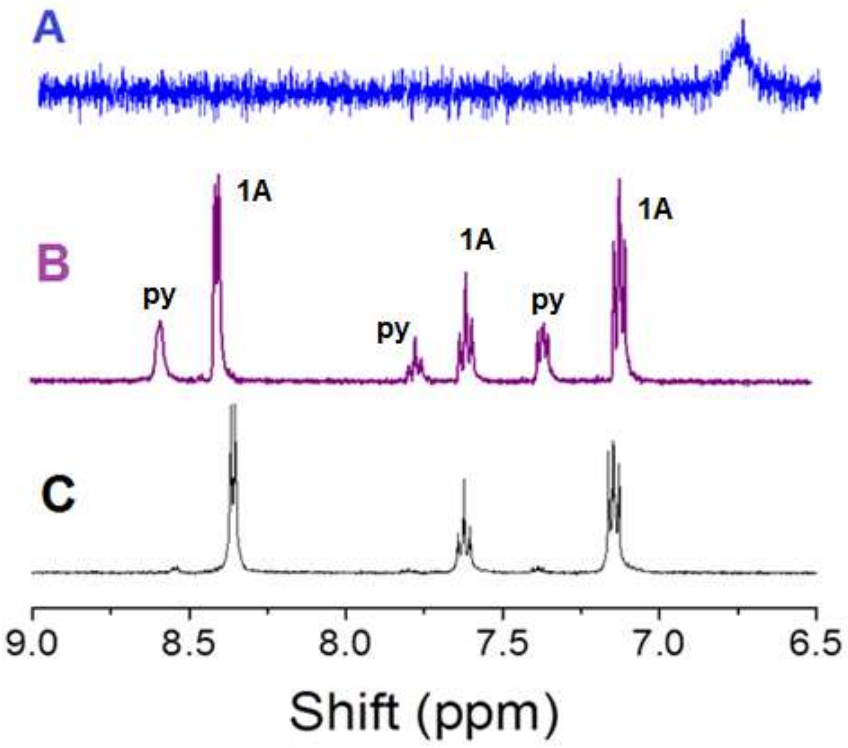

Figure 3.6. ^{1}H-NMR spectra of CD_3CN solutions of A) $\mathbf{1A}^{+}$ (blue), B) a mixture of pyridine and **1A** (purple), C) the reaction of 1.5 mM $\mathbf{1A}^{+}$ with 4 eq. OH^{-} (black).

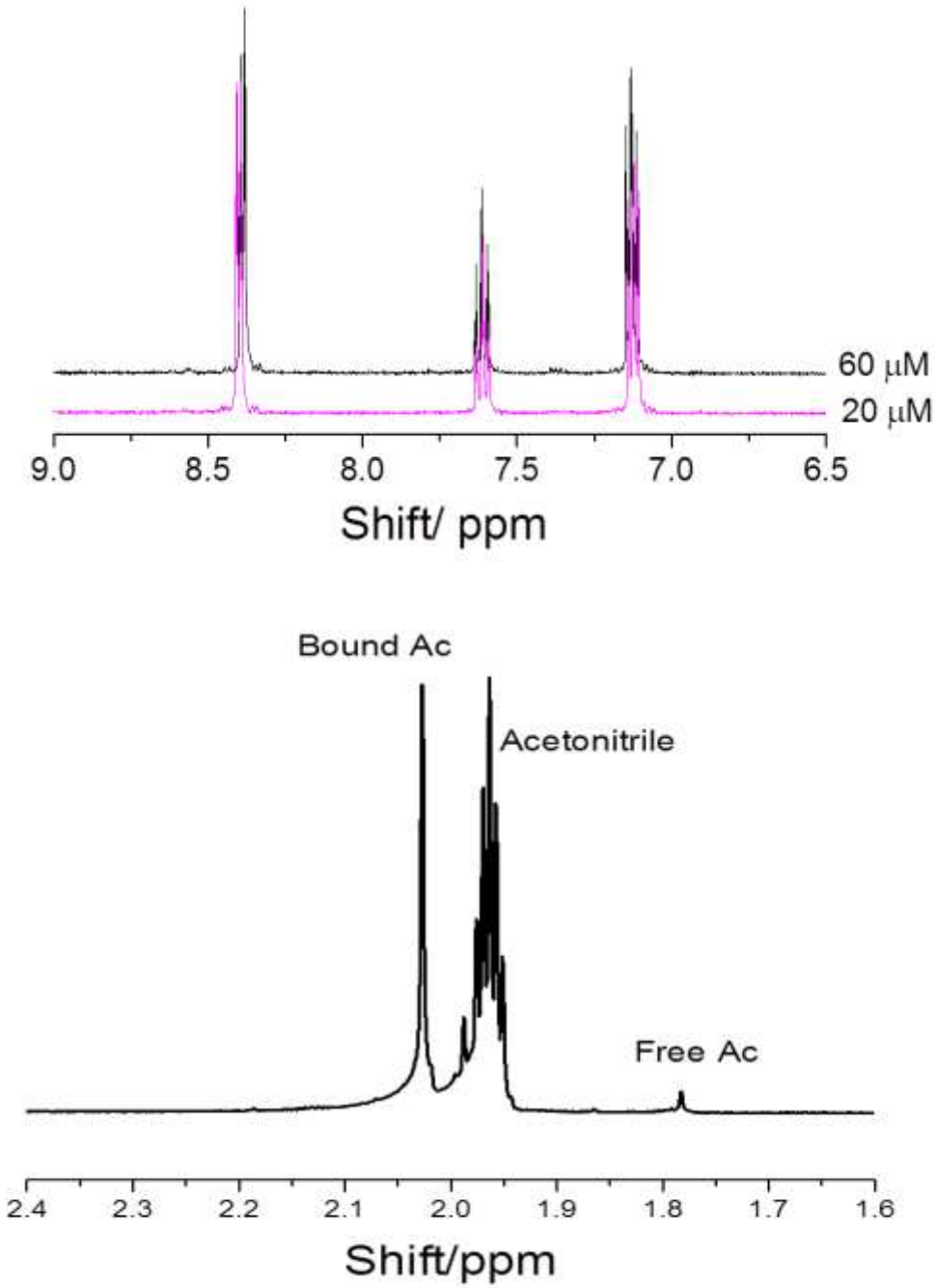

Figure 3.7: Top: ^{1}H-NMR titration studies of free pyridine, as next to 1 mM of **1A**. We note 0.5% decomposition of 1.4 mM would yield approximately 30 μM pyridine. Bottom: Acetate region from Figure 3.6.

High resolution mass spectrometry of the reaction products using ^{18}O-hydroxide were conducted to determine the origin of the evolved O_2. After dissolving **1A**$^+$ in water (79% ^{18}O) containing 0.3M sodium bicarbonate (100% ^{18}O), the product *solution* was analyzed by ESI-QTOF-MS in positive ion mode (No negative ion peaks were observed). The MS spectrum (Figure 3.8) consisted of peaks at 875 m/z (**1A** + ^{23}Na)$^+$, 853 (**1A**H)$^+$, 774 (**1A**-py + H$^+$) 796 (**1A**-py + ^{23}Na$^+$), and 793 (**1A**-OAc)$^+$, and no evidence for ^{18}O incorporation into any fragment. Peaks at M+1 and M+2 for each fragment quantitatively account for the natural abundance of ^{13}C in each product (± 1%) and were completely consistent with control MS spectra of **1A** in either ^{16}O or ^{18}O water, with and without added ^{18}O bicarbonate (Figures 3.8-3.10). Hence, **1A** is inert to μ-oxo/water exchange, and throughout the course of the O_2 evolving reaction of **1A**$^+$ in bicarbonate no ^{18}O was incorporated into the bridging oxos. This outcome dictates that the oxygen atoms in the product O_2 must *both* originate from hydroxide, a prediction that was subsequently confirmed by membrane inlet mass spectrometry (MIMS). MIMS allows real-time detection of O_2 produced from dissolution of **1A**$^+$ in alkaline solution. The O_2 product from the dissolution of **1A**$^+$ with ^{18}O bicarbonate in 97% ^{18}O-water under purged-Ar atmosphere was comprised of 75% $^{36}O_2$, 19% $^{34}O_2$ and 6% $^{32}O_2$ (Figure 3.11). The amount of $^{34}O_2$ detected is larger than what was expected given the high purity ^{18}O-labeled reagents used. Performing identical experiments with higher amounts of background air in the MS, we observed that the intensity of the $^{34}O_2$ signal increases while the $^{36}O_2$ signal decreases in direct correlation with one another (Figure 3.12). Therefore, we assign the $^{34}O_2$ signal as arising from scrambling of $^{36}O_2$ with atmospheric $^{32}O_2$ *via*: $^{32}O_2 + {}^{36}O_2 \rightarrow 2\ {}^{34}O_2$. The observed 75% $^{36}O_2$ signal is thus a lower bound

percentage of the total O_2 yield. The cumulative results suggest that the O_2 evolution reaction occurs by substitution of OH^- at acetate and/or pyridine sites of $\mathbf{1A^+}$, and that these sites are eventually evolved as O_2 following oxidation by the $\mathbf{1A^+/1A}$ couple (1.25 V vs. NHE). $\mathbf{1A^+}$ thus has unique, dual functionality depending on ligation, serving both as outer sphere oxidant and catalyst.

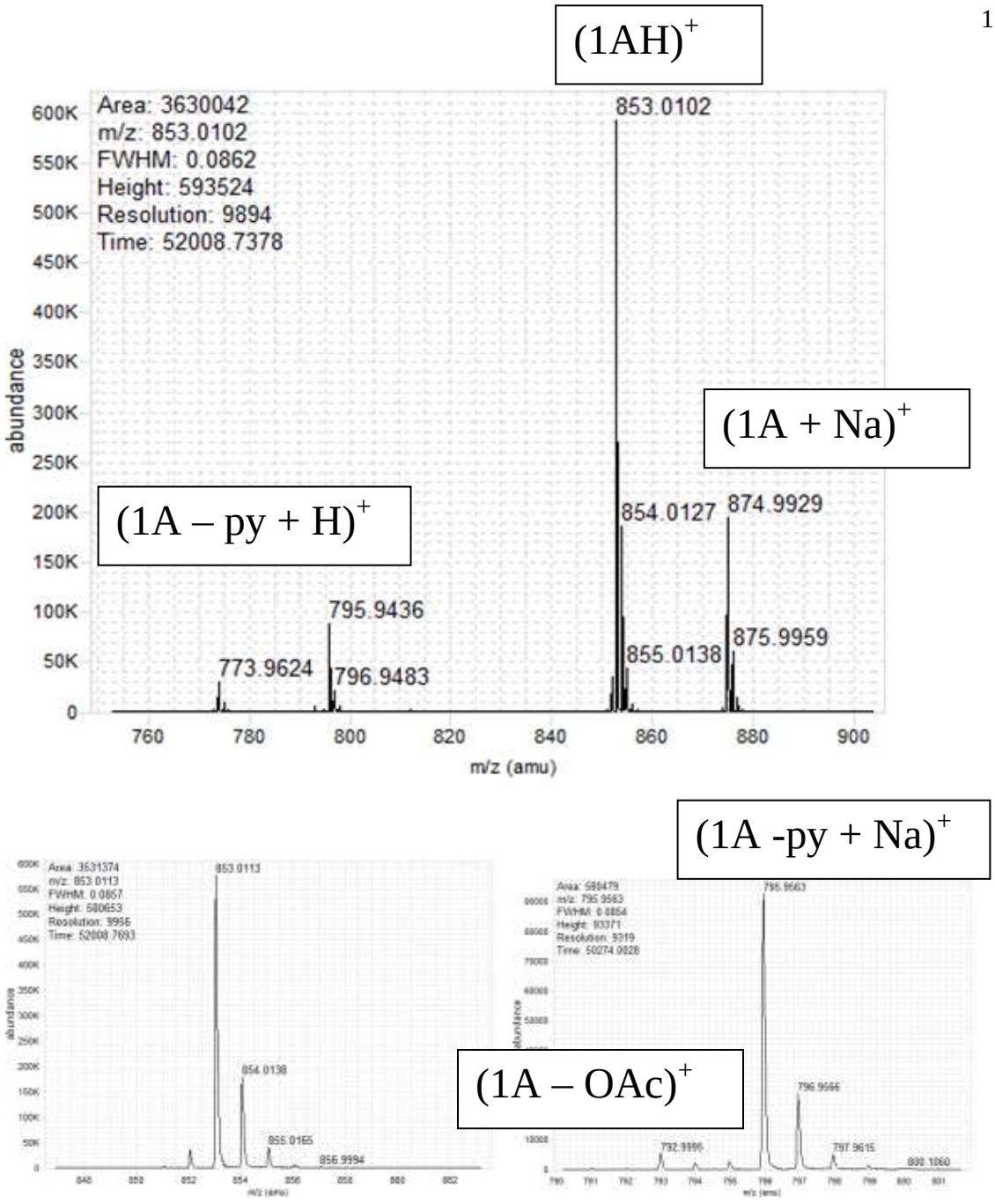

Figure 3.8: ESI-QTOF/MS spectra of the reaction products after **1A**(ClO_4) is dissolved in water (18O, 79%) containing 10 equivalents of sodium bicarbonate (100% ^{18}O).

equivalents of sodium bicarbonate (100% ^{18}O).

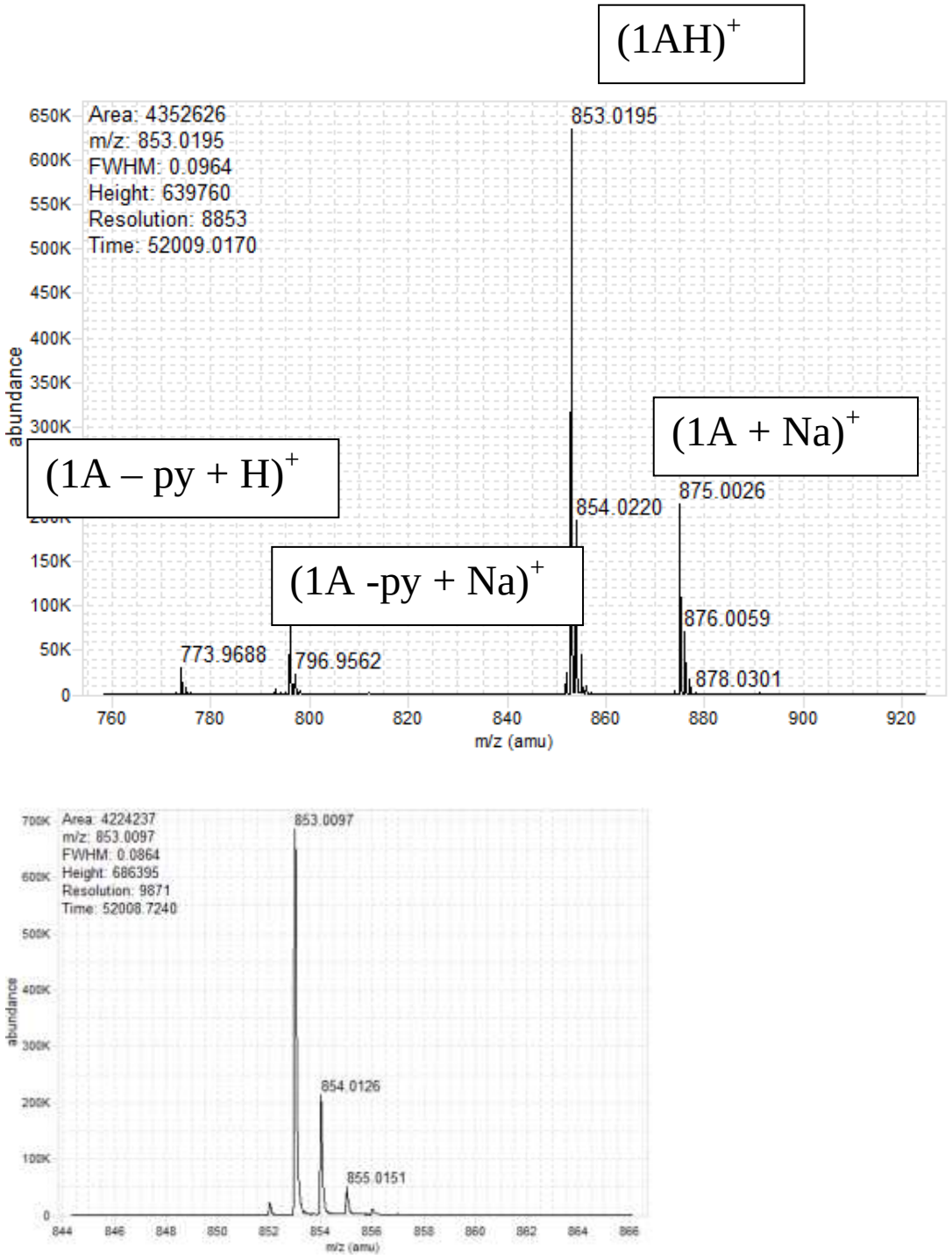

Figure 3.9: ESI-QTOF/MS spectra of **1A** in water, 18O (45%). Incubation time of 20 minutes prior to measurement.

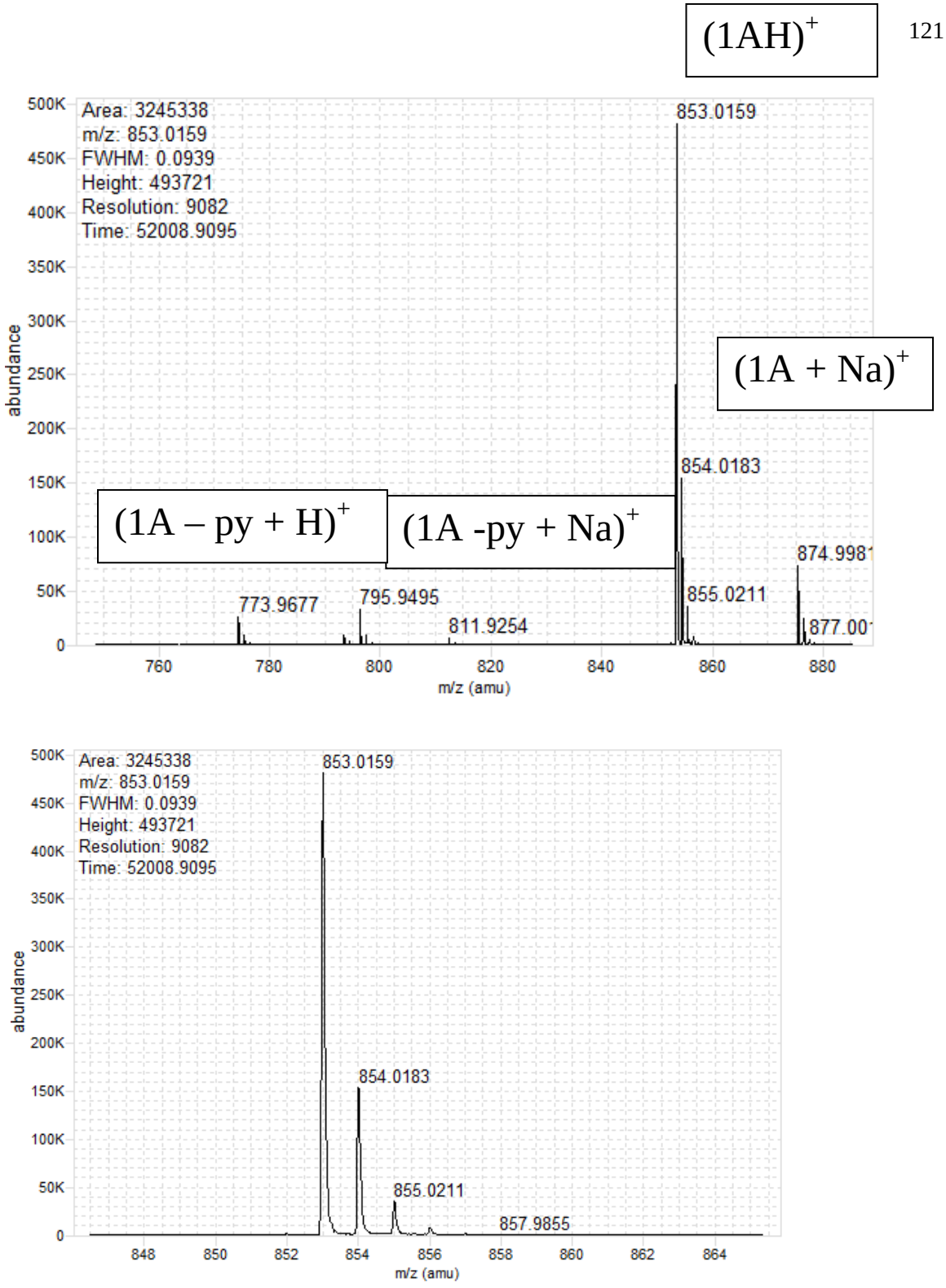

Figure 3.10: ESI-QTOF/MS spectra of **1A** in water, 16O.

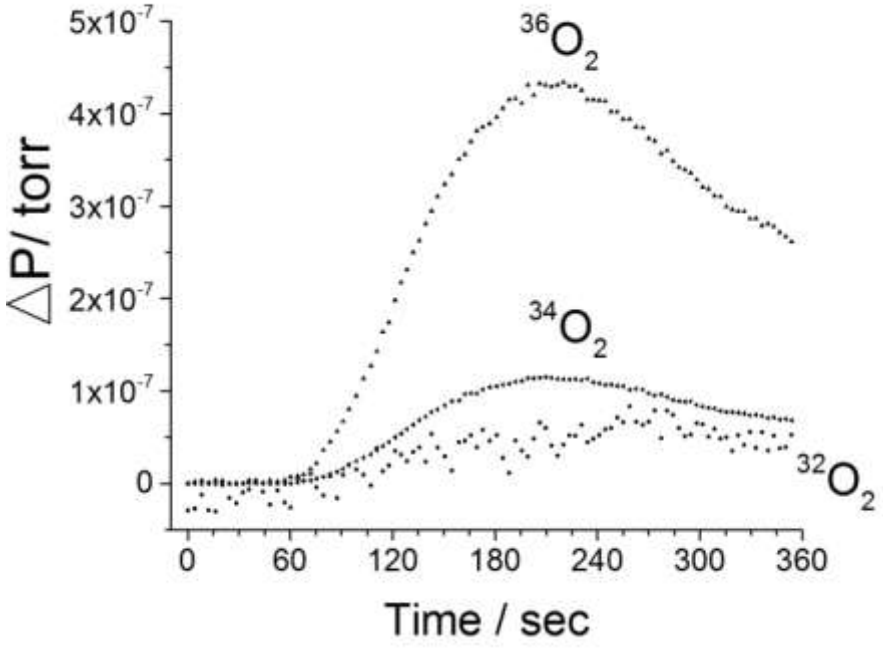

Figure 3.11. MIMS data for the reaction of **1A+** (8mM) with ^{18}O labeled sodium bicarbonate (0.15 M) in 97% ^{18}O water.

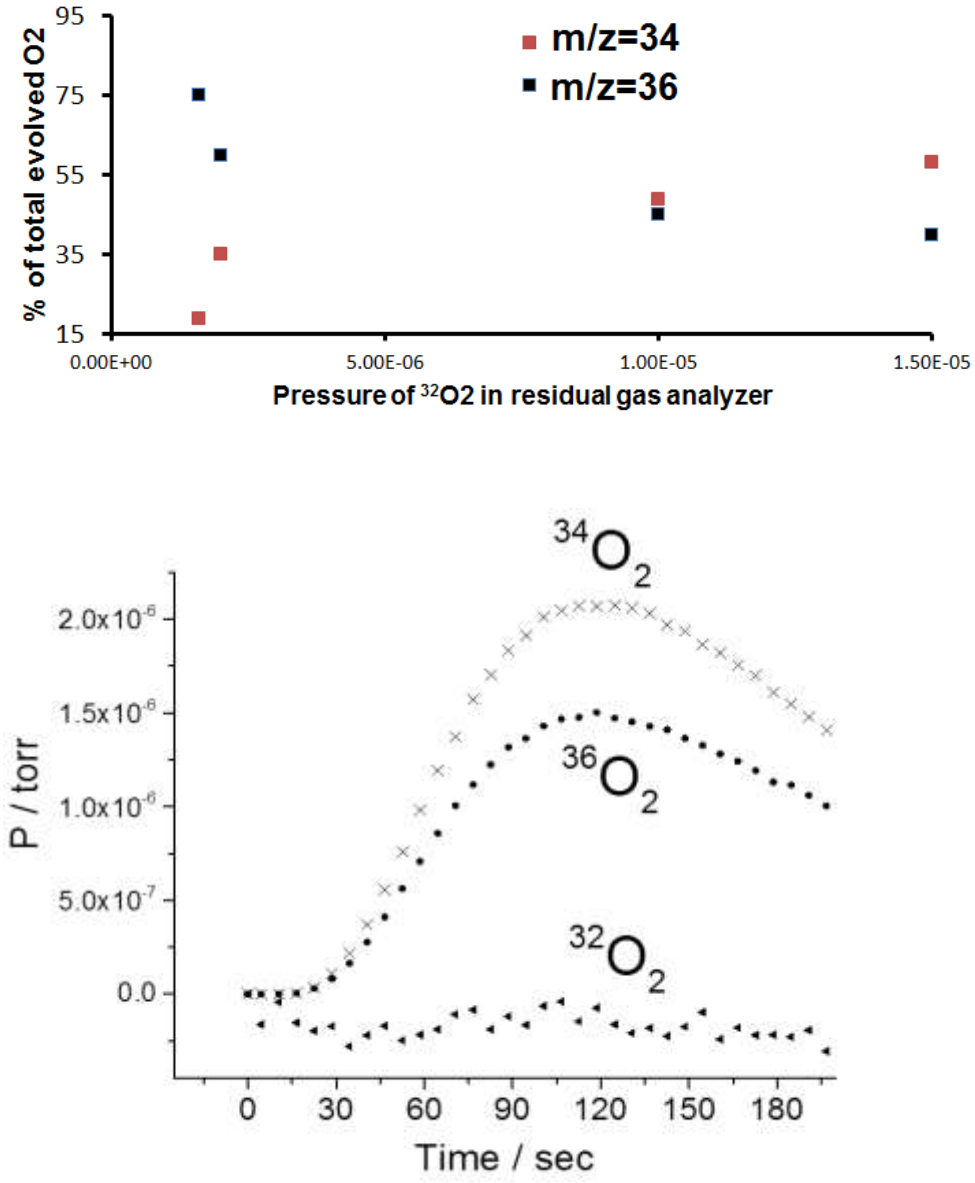

Figure 3.12: Top: Percentage of O_2 detected with m/z 36 (of total O_2) after reaction of **1A**$^+$ with 97% ^{18}O labeled water containing ^{18}O labeled sodium bicarbonate as a function of background atmospheric $^{32}O_2$ signal in the mass spec. Bottom: A representative MS from the reaction performed at ambient atmosphere.

For further insights, we pursued DFT calculations to predict the energetics of formation of intermediates with progressive addition or exchange of ligands for water and hydroxide. All the calculations were performed in acetonitrile solution on the geometries optimized in vacuo. To calculate the energetics of different reaction pathways, we employed fragments (OH^-, OAc^- and Py) solvated by four water molecules. The calculated oxidation potential of the **1A/1A$^+$** couple is 5.57 eV, vertical line in Figure 3.13, which nicely compares with the experimental oxidation potential of ~5.7 eV vs vacuum (i.e. 1.25 V vs. NHE +4.44 eV). The reactivity is likely initiated by OH^- binding to **1A/1A$^+$**. Here we consider two binding sites, i.e. exchange of OH- with a pyridine or insertion of OH^-into a Co-OAc bond to lead to a terminal hydroxo complex which is stabilized by a hydrogen bond to the monodentate acetate ligand, **1A(OH)** in Figure 3.13. OH- addition to the neutral **1A** cubane is thermodynamically not favored (Figure 3.14), while upon oxidation the lowest energy pathway is the one leading to **1A(OH)** rather than the pyridine exchange (-0.92 vs. -0.63 eV, respectively). Li and Siegbahn[56] have calculated this intermediate at the identical Co_4(3,3,3,4) level. Analogous bonding environments have been directly observed in Mn cubanes,[60] and correlated with water oxidation activity in cobalt hangman complexes.[22]

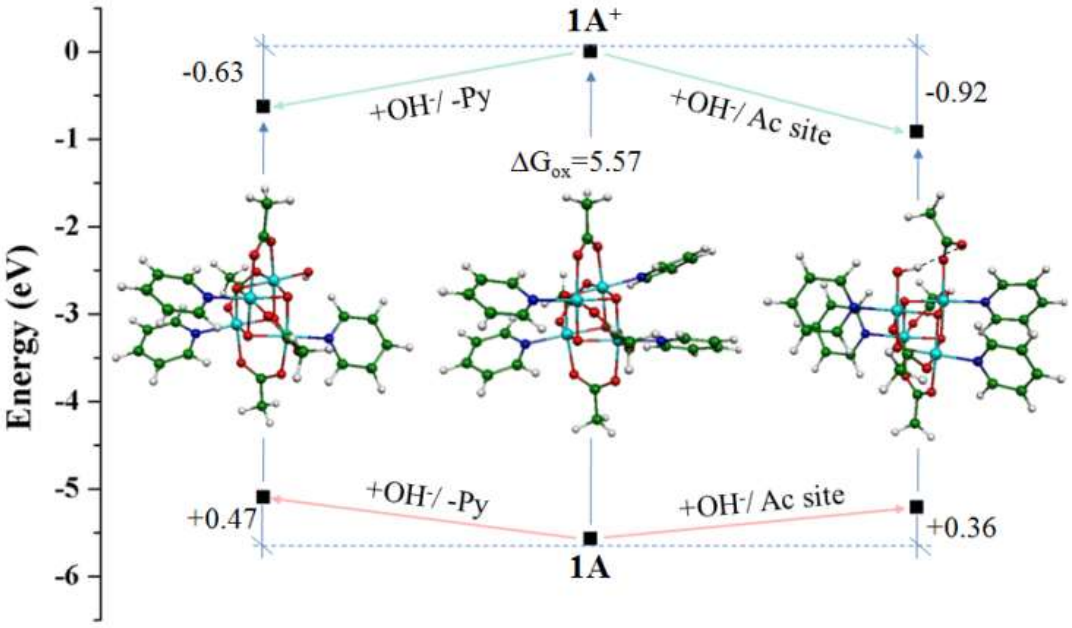

Figure 3.13. Energetics of intermediates for the first OH- binding site (intermediates 1A(OH)) from DFT calculations.

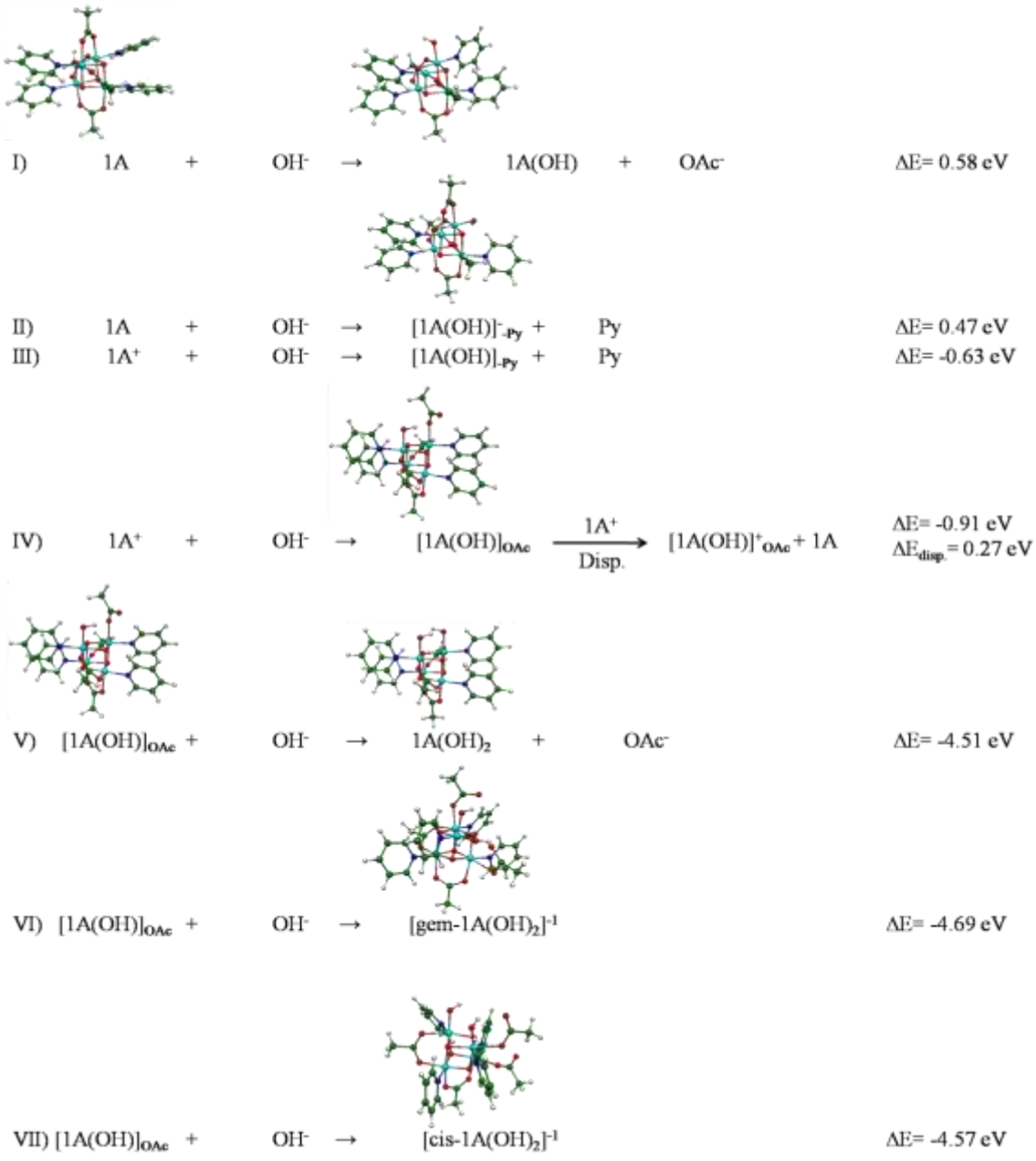

Figure 3.14: Calculated energies of different reaction pathways.

Li and Siegbahn assumed conditions of 1.43 V oxidizing potential[56] and calculated that the OH^-/acetate addition product **1A(OH)** is further oxidized to Co_4(3,3,4,4). This derivative undergoes O-O bond formation *via* water nucleophilic attack. By our calculations, the **1A+(OH)** reaction intermediate is not favorably oxidized by $\mathbf{1A^+}$ (+0.27 eV).We thus considered a 2nd OH^-/H_2O binding as the next step in the reaction mechanism. Our calculations find it unfavorable to replace a second pyridine ligand from Co_4(3,3,3,4) for OH^- (+0.07 eV) or H_2O (+0.05 eV). Thus, the cubium likely retains at least 3 pyridine ligands throughout the catalytic mechanism. This agrees with the studies of Bonchio, et. al., who observed a direct correlation of electron transfer rates with the Hammett values of pyridine substituents[51].

Starting from the $\mathbf{1A^+}$ cubium we find three doubly hydroxylated intermediates that are of comparable energy, depicted in Figure 3.15. In one species, two OH^- substitute for one OAc to form the neutral product, $\mathbf{[cis\text{-}1A(OH)_2]_{\text{-}OAc}}$. The other two species are negatively charged, retaining two monodentate acetates. These species differ in having the two hydroxyls ligated either as a 1,1-gem-diol, $\mathbf{[gem\text{-}1A(OH)_2]^{-1}}$ (on the same cobalt), or as a 1,2-cis-diol $\mathbf{[cis\text{-}1A(OH)_2]^{-1}}$ (on different cobalts). Of these three species, $\mathbf{[gem\text{-}1A(OH)_2]^{-1}}$ is the most stable product, lying 0.12 and 0.17 eV below $\mathbf{[cis\text{-}1A(OH)_2]^{-1}}$ and $\mathbf{[cis\text{-}1A(OH)_2]_{\text{-}OAc}}$, respectively (Figure 3.14).

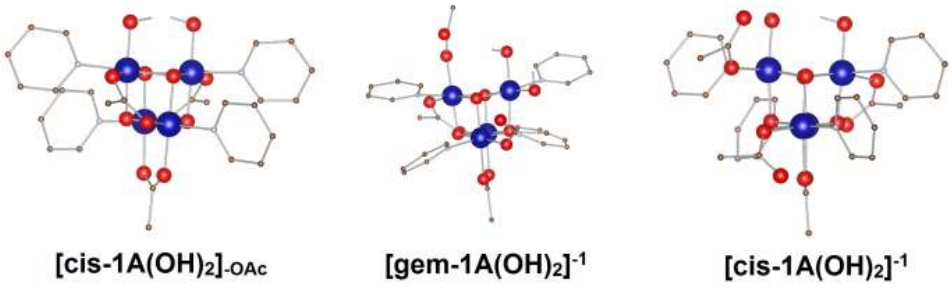

Figure 3.15. Lowest energy doubly hydroxylated intermediates.

All [**1A(OH)$_2$]** intermediates (with or without OAc^- dissociation) are favorably oxidized by **1A**$^+$, giving the catalytic center Co_4(3,3,4,4). Our calculations indicate the doubly oxidized **[cis-1A(OH)$_2$]** neutral complex to be the favored product of the disproportionation reaction with **1A**$^+$, with a favorable reaction energetics of 0.66 eV, followed by **[gem-1A(OH)$_2$]** and **[cis-1A(OH)$_2$]$^+$-OAc**, at 0.29 and 0.15 eV, respectively. Water oxidation through a 1,1-gem-diol was proposed by Mattioli et al.[61], while Wang and Van Voorhis[57] reported the reaction to occur via a 1,2-cis-diol. Notably, by including 4 water molecules in the solvation sphere of the reaction sites of the **[cis-1A(OH)$_2$]** and **[gem-1A(OH)$_2$]** neutral complexes we find these to be essentially isoenergetic. Assessing the full O-O bond formation mechanism is beyond the scope of this paper, but preliminary results indicate similar activation energies for the coupling reactions between the oxos on different Co atoms (cross-coupling) and the same Co atom (geminal).

We pursued analogous experimental testing of cubium **1B**$^{3+}$. This molecule features bpy ligated to two coordination sites of each Co, greatly limiting a potential geminal coupling mechanism.

Reported syntheses were used to isolate **1B**$(ClO_4)_3$ and **1B**$[Ce(NO_3)_6]$ salts according to Christou et. al.[34] To our knowledge, the EPR signal has not been previously published, but has been described as a broad resonance at g= 2.20 with no resolved hyperfine. Our EPR spectrum (Figure 3.16) supports this description and confirms the expected spin S = ½ ground state. The shift of the g value (g > 2.0023) arising from Co spin-orbit coupling indicates a greater than half-filled $3d^n$ valence shell (n > 5). Analogous to **1A**$^+$, the

absence of resolved ^{59}Co hyperfine splitting indicates the hole is delocalized onto the four μ_3-oxos of the $[Co_4O_4]^{5+}$ core.

In contrast to $\mathbf{1A}^{+}$, UV-Vis spectroscopy of aqueous $\mathbf{1B}^{3+}$ solutions after aging for 1 hr show 12±3% reduction to cubane $\mathbf{1B}^{2+}$ with no production of O_2 (Figure 3.17). The oxidized substrate is bpy, as evidenced by detection of CO_2. The identity of the counter anion strongly affected the extent to which this side reaction proceeded in experiments where $\mathbf{1B}^{3+}$ was dissolved in aqueous OH^-. In the case of $\mathbf{1B}[Ce(NO_3)_6]$, O_2 is produced in 23% yield, with the side reaction limited to 0.7% CO_2. In contrast, only CO_2 and no O_2 was observed from $\mathbf{1B}(ClO_4)_3$.

We derive three conclusions from these results. First, $\mathbf{1B}(ClO_4)_3$ serves as a negative control in which the hydrolytic or decomposed product is not a catalyst capable of driving water oxidation at 1.25 V ($\mathbf{1B}^{3+}/\mathbf{1B}^{2+}$). Second, the cerium anion promotes an O_2 evolution mechanism not obtainable from $\mathbf{1B}^{3+}$ otherwise. Finally, given that $\mathbf{1A}^{+}$ is capable of producing O_2 while $\mathbf{1B}^{3+}$ does not, we propose a geminal coupling mechanism occurs for **1A**.

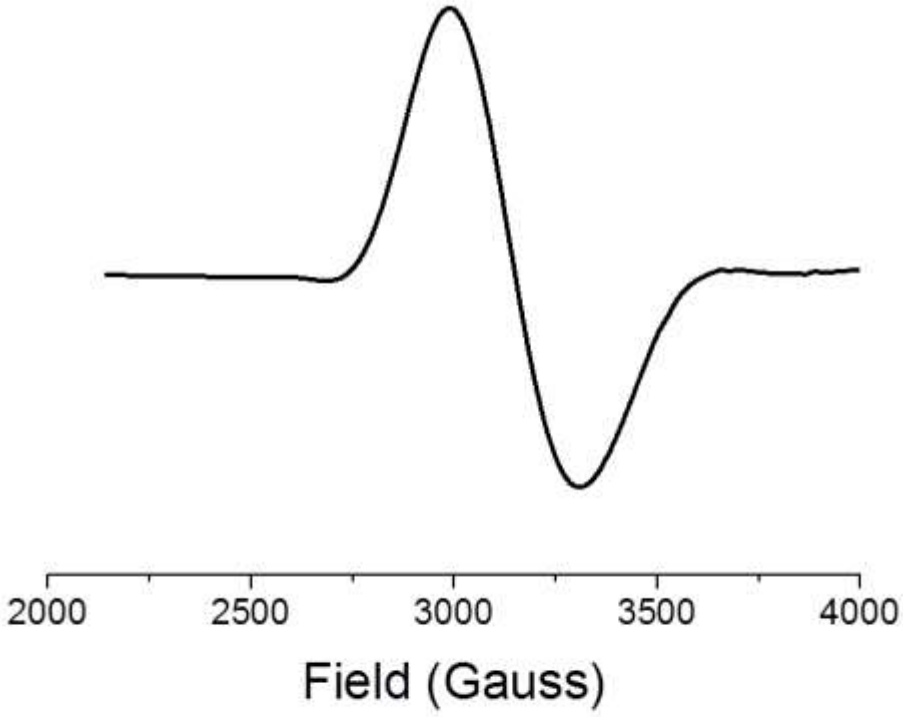

Figure 3.16: X-band EPR spectrum of **1B**$^{3+}$**,** g = 2.20.

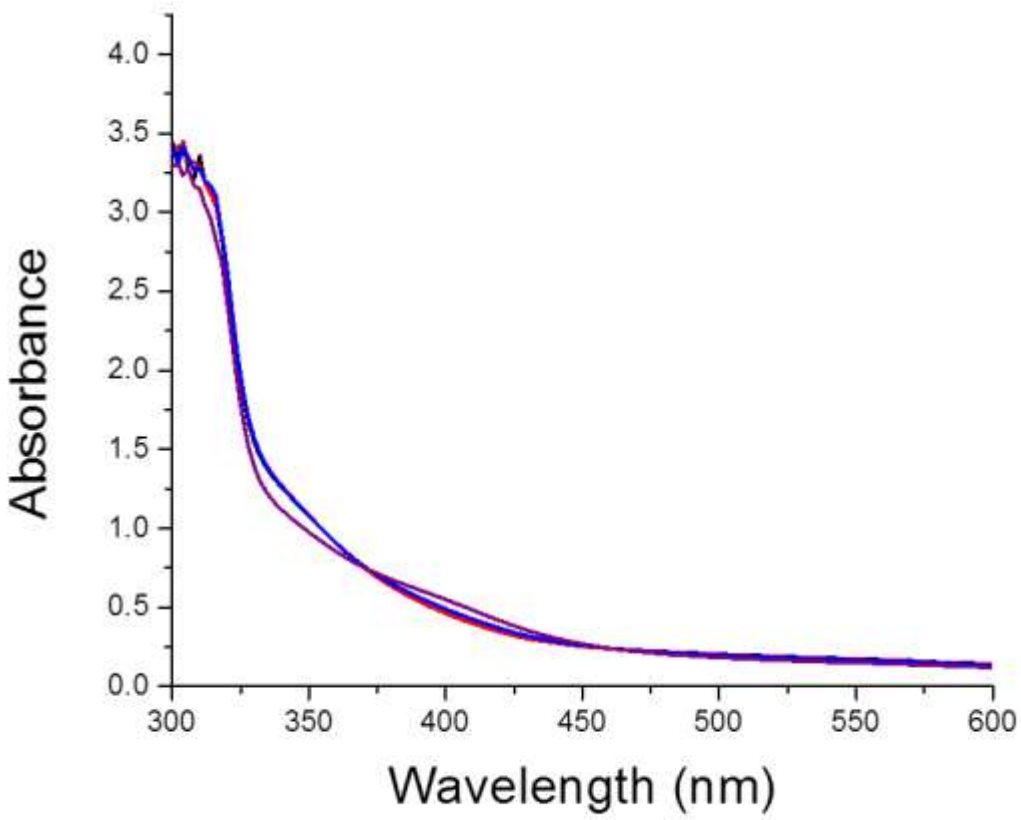

Figure 3.17: A solution of **1B**$^{3+}$ aged in water 0 (black), 1 (red), 10 (blue) and 60 minutes (purple).

3.5 Discussion

Both experimental results and calculations show that O_2 evolution occurs by an ordered sequence of OH^- addition to $\mathbf{1A}^+$ forming the catalytic precursor, followed by intermolecular electron transfer to 3 intact cubiums. Despite being inert for electrochemical water oxidation in aqueous phosphate buffer at pH 7, $\mathbf{1A}^+$ substitutes organic acetate and pyridyl ligands with strong selectivity for OH^-. As predicted by DFT calculations of Li and Siegbahn[56], as well as ours herein, insertion into Co-OAc sites is energetically preferred. Terminal sites for substrate oxos (not bridging oxo sites) are responsible for O_2 formation, as shown by ^{18}O-isotopic labeling. Outer sphere oxidation of the OH^- addition intermediate can occur only if the intermediate has an oxidation potential lower than that of the cubium/cubane reduction potential (1.25 V vs. NHE).

Our calculations show that sequential insertion of 2 OH^- into 2 Co-OAc^- sites, forming either 1,1(gem)-dihydro or 1,2-dihydroxo intermediates, are the energetically preferred pathways to form species that, thermodynamically, can be oxidized by $\mathbf{1A}^+$ to yield either side-on ($\eta^{1,1}$-) or bridging ($\eta^{1,2}$-)peroxo intermediates, respectively. The nature of the subsequent O_2 formation and release steps will be the subject of a future report.

Earlier reports[49–51,54] that O_2 evolution from water can be ascribed to cubane **1A** as the catalyst under photochemical conditions using photo-generated oxidants ($Ru(bpy)_3^{3+}$, 1.26 V, and persulfate radical, 2.4 V), gain further support from the present work. It is plausible that ligand dissociation to produce an available water binding site on cubane **1A** is more facile *under illumination*, rationalizing different observations seen recently in photochemical vs. electrochemical systems[58]. Precedence for this is known by the

$Mn_4O_4(O_2PPh_2)_6$ cubane, which photo-dissociates phosphinate anion upon UV irradiation[62–65].

Another strategy aimed at promoting water/OH^- binding to **1A** is aqueous aging, as has been reported recently[59]. This too correlated with water oxidation activity; after 24 hours of aging **1A** in water, 1% of total Co performs electrochemical catalysis. The active species characterized more favorably as **1A** minus an acetate ligand as opposed to a fully hydrolyzed, aqueous Co^{2+} product[59]. These results are overall consistent with slow kinetics anticipated for ligand exchange from low spin Co^{3+} centers. Our calculations confirm that the presence of ligands on the active catalyst is overall beneficial to promote stabilizing hydrogen-bonding environments around substrate OH^- groups. This utility is not available from heterogeneous cobalt oxide catalysts.

Our results also rationalize and provide updated context for other previous observations. Our data shows 0.5% ligand loss following a single turnover of $\mathbf{1A^+}/OH^-$, in excellent agreement with literature showing <5% photo-decomposition of **1A** after 6-12 turnovers using $Ru(bpy)_3^{3+}$ and persulfate radicals[49]. The lack of O_2 evolution at pH 7 in the absence of buffer in this latter system[54] is now rationalized by the insufficient concentration of necessary OH^- substrate.

Another result that the present work demonstrates is that O_2 evolution can occur using the $\mathbf{1A^+/1A}$ oxidant couple at standard potential of 1.25 V vs. NHE. This observation appears to contradict our previous data[54]- showing that $Ru(bpy)_3^{3+}$ alone (1.26 V) could not generate O_2 from **1A**. This is reinforced as well by the electrochemical results of several groups[49,51,58] (as well as Figure 3.1) which show little to no water oxidation current at

applied potentials in that region. This paradox is rationalized as follows: as measured here, pseudo-first order rate constants for hydroxide reaction with **1A**$^{+}$ are on the order of 10^{-4}-10^{-3} s^{-1} (Figure 3.5). Rates of $Ru(bpy)_3^{3+}$ decomposition by OH^- promoted hydrolysis are on the order of 10^{-3}-10^{-2} s^{-1}, as measured by Mallouk et al.[66]. Hence, hydroxide (if available) reacts with $Ru(bpy)_3^{3+}$ (typically in excess concentration) roughly an order of magnitude faster than with **1A**$^{+}$. When considering that all previous studies have utilized pH 7-8 (= 10^{-6}-10^{-7} M [OH^-]), millimolar concentrations of **1A**$^{+}$ would yield rates approximately 10^{-9}-10^{-10} s^{-1} for O_2 evolution, as estimated by eqn. 2. Such rates are likely to be additionally affected by the presence of buffers which have been reported to compete for cobalt binding sites[67]. In particular, phosphate has been shown to inactivate[68] and inhibit[20] homogeneous cobalt catalysts by binding at sites for substrate OH^-.

Lastly, when testing water oxidation catalysts with chemical oxidants, few are known[69] and each have tradeoffs: e.g., cerium ammonium nitrate has been challenged as noninnocent[70], sodium periodate may donate substrate oxos, and $Ru(bpy)_3^{3+}$ is unstable. Here, pristine **1A**$^{+}$ shows excellent aqueous stability at pH<7 (**1B**$^{3+}$<pH4). These cubiums may prove to be innocent, outer-sphere oxidants to drive candidate water oxidation catalysts under acidic conditions.

3.6 Conclusion

Effective heterogeneous oxidation catalysts such as spinel Co_3O_4 and cubic $LiCoO_2$ have lattices built around a Co_4O_4 cubane type structure[2,4,71]. These water oxidation catalysts, at an oxidizing potential of 1.26 V ($Ru(bpy)_3^{3+}$), have pseudo-first order rate constants for O_2 evolution on the order of 10^{-2}-10^{-1}/s*Co (e.g, 0.019 for $LiCoO_2$[4], 0.01 for Co_3O_4[2], 0.5 for Co-M2P[15]). Compared to constants obtained here at 1.25 V (10^{-4}-10^{-3}), faster catalysis of 1-3 orders of magnitude are afforded by efficient water binding. This architecture is known to be important to allow thermodynamically accessible oxidation to Co^{4+}. This same feature is also seen in the favorable oxidation potentials of the molecular clusters, **1A/1A$^+$** and **1B^{2+}/1B^{3+}**, in contrast to the much higher Co^{III}/Co^{IV} oxidation potentials (~ 1 V higher) for incomplete cubane complexes $[Co_3O_4]^{2+}$ and dinuclear complexes $[Co_2O_2]^{+}$.[54] This comparison suggests that a molecular metal-oxo cubane architecture, if synthesized inside an oxidatively stable ligand environment, that allows accessible water binding sites on Co, could achieve even faster turnover rates as homogeneous catalyst.

While cubium **1B^{3+}** did not have stable organic ligand architecture, the acetates and pyridines are not oxidized in the case of **1A$^+$**. Hence, this offers an optimistic future that molecular cobalt catalysts with organic ligands- if designed appropriately- may tolerate the harsh conditions needed to oxidize water and remain stable over useful lifetimes.

3.7 Acknowledgment

This work was supported by the Air Force Office of Scientific Research (FA9550-11-1-0231). Fellowships were provided by NSF-IGERT (P.F.S., DGE 0903675), NSF CLP #1213772 (S.K.), Rutgers University (A.L.) the Lawrenceville School, Lawrenceville, NJ (L.H.), CAPES Brazil 13386/13-1 (K.U.D.C), and BASF (V.S.). We are grateful to Drs. A. Ermakov, G. K. Kumaraswamy and A. Tyryshkin for instrumentation support and to Dr. Y. Geletii, Dr. M. Symes, G. Gardner, and C. Kaplan for helpful discussions. The authors declare no competing financial interests.

3.8 References

(1) Shafirovich, V. Y.; Strelets, V. V. Nouv. J. Chim. 1977, 2, 199–201.
(2) Jiao, F.; Frei, H. Angew. Chemie-International Ed. 2009, 48, 1841–1844.
(3) Brunschwig, B. S.; Chou, M. H.; Creutz, C.; Ghosh, P.; Sutin, N. J. Am. Chem. Soc. 1983, 105, 4832–4833.
(4) Gardner, G. P.; Go, Y. B.; Robinson, D. M.; Smith, P. F.; Hadermann, J.; Abakumov, A.; Greenblatt, M.; Dismukes, G. C. Angew. Chemie 2012, 124, 1648–1651.
(5) Suzuki, O.; Takahashi, M.; Fukunaga, T.; Kuboyama, J. No Title. US Patent 3399966, 1968.
(6) El Wakkad, S. E. S.; Hickling, A. Trans. Faraday Soc. 1950, 46, 820–824.
(7) Kanan, M. W.; Nocera, D. G.; Kana, M. W. Science (80-.). 2008, 321, 1072–1075.
(8) Hutchings, G. S.; Zhang, Y.; Li, J.; Yonemoto, B. T.; Zhou, X.; Zhu, K.; Jiao, F. J. Am. Chem. Soc. 2015, 137, 4223–4229.
(9) Gerken, J. B.; McAlpin, J. G.; Chen, J. Y. C.; Rigsby, M. L.; Casey, W. H.; Britt, R. D.; Stahl, S. S.; Rigsby, L.; Casey, W. H.; Britt, R. D.; Stahl, S. S. J. Am. Chem. Soc. 2011, 133, 14431–14442.
(10) Nocera, D. G. Acc. Chem. Res. 2012.
(11) Risch, M.; Ringleb, F.; Chernev, P.; Zaharieva, I.; Dau, H. Energy Environ. Sci. 2015, 661–674.
(12) Risch, M.; Klingan, K.; Ringleb, F.; Chernev, P.; Zaharieva, I.; Fischer, A.; Dau, H. ChemSusChem 2012, 5, 542–549.
(13) Du, P.; Kokhan, O.; Chapman, K. W.; Chupas, P. J.; Tiede, D. M. J. Am. Chem. Soc. 2012, 134, 11096–11099.
(14) Zhong, M.; Hisatomi, T.; Kuang, Y.; Zhao, J.; Liu, M.; Iwase, A.; Jia, Q.; Nishiyama, H.; Minegishi, T.; Nakabayashi, M.; Shibata, N.; Niishiro, R.; Katayama, C.; Shibano, H.; Katayama, M.; Kudo, A.; Yamada, T.; Domen, K. J. Am. Chem. Soc. 2015, 137, 5053–5060.
(15) Koroidov, S.; Anderlund, M. F.; Styring, S.; Thapper, A.; Messinger, J. Energy Environ. Sci. 2015, 8, 2492–2503.
(16) Li, Y.; Zhang, L.; Torres-Pardo, A.; González-Calbet, J. M.; Ma, Y.; Oleynikov, P.; Terasaki, O.; Asahina, S.; Shima, M.; Cha, D.; Zhao, L.; Takanabe, K.; Kubota, J.; Domen, K. Nat Commun 2013, 4.
(17) Kanan, M. W.; Surendranath, Y.; Nocera, D. G. Chem. Soc. Rev. 2009, 38, 109–114.
(18) Zhong, D. K.; Cornuz, M.; Sivula, K.; Gratzel, M.; Gamelin, D. R. Energy Environ. Sci. 2011, 4, 1759–1764.
(19) Han, X. B.; Zhang, Z. M.; Zhang, T.; Li, Y. G.; Lin, W.; You, W.; Su, Z. M.; Wang, E. B. J. Am. Chem. Soc. 2014, 136, 5359–5366.
(20) Wang, D.; Groves, J. T. Proc. Natl. Acad. Sci. 2013, 110 , 15579–15584.
(21) Wasylenko, D. J.; Ganesamoorthy, C.; Borau-Garcia, J.; Berlinguette, C. P. Chem. Commun. 2011, 47, 4249–4251.
(22) Dogutan, D. K.; McGuire, R.; Nocera, D. G. J. Am. Chem. Soc. 2011, 133, 9178–9180.

(23) Shevchenko, D.; Anderlund, M. F.; Thapper, A.; Styring, S. Energy Environ. Sci. 2011, 4, 1284–1287.
(24) Rigsby, M. L.; Mandal, S.; Nam, W.; Spencer, L. C.; Llobet, A.; Stahl, S. S. Chem. Sci. 2012, 3, 3058.
(25) Evangelisti, F.; Güttinger, R.; Moré, R.; Luber, S.; Patzke, G. R. J. Am. Chem. Soc. 2013, 135, 18734–18737.
(26) Yin, Q.; Tan, J. M. J. M.; Besson, C.; Geletii, Y. V; Musaev, D. G.; Kuznetsov, A. E.; Luo, Z.; Hardcastle, K. I.; Hill, C. L. Science (80-.). 2010, 328, 342–345.
(27) Pizzolato, E.; Natali, M.; Posocco, B.; Montellano Lopez, A.; Bazzan, I.; Di Valentin, M.; Galloni, P.; Conte, V.; Bonchio, M.; Scandola, F.; Sartorel, A.; Montellano López, A. Chem. Commun. 2013, 49, 9941–9943.
(28) Leung, C.-F.; Ng, S.-M.; Ko, C.-C.; Man, W.-L.; Wu, J.; Chen, L.; Lau, T.-C. Energy Environ. Sci. 2012, 5, 7903.
(29) Lv, H.; Song, J.; Geletii, Y. V; Vickers, J. W.; Sumliner, J. M.; Musaev, D. G.; Kögerler, P.; Zhuk, P. F.; Bacsa, J.; Zhu, G.; Hill, C. L. J. Am. Chem. Soc. 2014, 136, 9268–9271.
(30) Swiegers, G. F.; Clegg, J. K.; Stranger, R. Chem. Sci. 2011, 2, 2254–2262.
(31) Sartorel, A.; Bonchio, M.; Campagna, S.; Scandola, F. Chem. Soc. Rev. 2013, 42, 2262–2280.
(32) Dismukes, G. C.; Brimblecombe, R.; Felton, G. A. N.; Pryadun, R. S.; Sheats, J. E.; Spiccia, L.; Swiegers, G. F. Acc. Chem. Res. 2009, 42, 1935–1943.
(33) Blakemore, J. D.; Crabtree, R. H.; Brudvig, G. W. Chem. Rev. 2015. DOI: 10.1021/acs.chemrev.5b00122.
(34) Dimitrou, K.; Brown, A. D.; Concolino, T. E.; Rheingold, A. L.; Christou, G. Chem. Commun. 2001, 1284–1285.
(35) Dimitrou, K.; Folting, K.; Streib, W. E.; Christou, G. J. Am. Chem. Soc. 1993, 115, 6432–6433.
(36) Dimitrou, K.; Sun, J.-S. S.; Folting, K.; Christou, G. Inorg. Chem. 1995, 34, 4160–4166.
(37) Dimitrou, K.; Folting, K.; Streib, W. E.; Christou, G. J. Chem. Soc. Chem. Commun. 1994, 838, 1385–1386.
(38) Chakrabarty, R.; Bora, S. J.; Das, B. K. Inorg. Chem. 2007, 46, 9450–9462.
(39) Chakrabarty, R.; Sarmah, P.; Saha, B.; Chakravorty, S.; Das, B. K. Inorg. Chem. 2009, 48, 6371–6379.
(40) Sarmah, P.; Chakrabarty, R.; Phukan, P.; Das, B. K. J. Mol. Catal. A Chem. 2007, 268, 36–44.
(41) Das, B. K.; Chakrabarty, R. J. Chem. Sci. 2011, 123, 163–173.
(42) Symes, M. D.; Surendranath, Y.; Lutterman, D. a.; Nocera, D. G. J. Am. Chem. Soc. 2011, 133, 5174–5177.
(43) Symes, M. D.; Lutterman, D. A.; Teets, T. S.; Anderson, B. L.; Breen, J. J.; Nocera, D. G. ChemSusChem 2013, 6, 65–69.
(44) McAlpin, J. G.; Stich, T. A.; Ohlin, C. A.; Surendranath, Y.; Nocera, D. G.; Casey, W. H.; Britt, R. D. J. Am. Chem. Soc. 2011, 133, 15444–15452.
(45) Stich, T.; Krzystek, J.; Mercardo, B. Q.; McAlpin, J. G.; Ohlin, C. A.; Olmstead, M. M.; Casey, W. H.; Britt, R. D. Polyhedron 2013, 64, 304–307.

(46) McAlpin, J. G.; Surendranath, Y.; Dincă, M.; Stich, T. A.; Stoian, S. A.; Casey, W. H.; Nocera, D. G.; Britt, R. D. J. Am. Chem. Soc. 2010, 132, 6882–6883.
(47) Beattie, J. K.; Hambley, T. W.; Klepetko, J. a.; Masters, A. F.; Turner, P. Polyhedron 1998, 17, 1343–1354.
(48) Sumner, C. E. Inorg. Chem. 1988, 27, 1320–1327.
(49) McCool, N. S.; Robinson, D. M.; Sheats, J. E.; Dismukes, G. C. J. Am. Chem. Soc. 2011, 133, 11446–11449.
(50) La Ganga, G.; Puntoriero, F.; Campagna, S.; Bazzan, I.; Berardi, S.; Bonchio, M.; Sartorel, A.; Natali, M.; Scandola, F. Faraday Discuss. 2012, 155, 177.
(51) Berardi, S.; Natali, M.; Bazzan, I.; Puntoriero, F.; Sartorel, A.; Scandola, F.; Campagna, S.; Bonchio, M. J. Am. Chem. Soc. 2012, 134, 11104–11107.
(52) Zhang, B.; Li, F.; Yu, F.; Wang, X.; Zhou, X.; Li, H.; Jiang, Y.; Sun, L. ACS Catal. 2014, 804–809.
(53) Zhou, X.; Li, F.; Li, H.; Zhang, B.; Yu, F.; Sun, L. ChemSusChem 2014, 7, 2453–2456.
(54) Smith, P. F.; Kaplan, C.; Sheats, J. E.; Robinson, D. M.; McCool, N. S.; Mezle, N.; Dismukes, G. C. Inorg. Chem. 2014, 53, 2113–2121.
(55) La Ganga, G.; Nardo, V. M.; Cordaro, M.; Natali, M.; Vitale, S.; Licciardello, A.; Nastasi, F.; Campagna, S. Dalt. Trans. 2014, 43, 14926–14930.
(56) Li, X.; Siegbahn, P. E. M. J. Am. Chem. Soc. 2013, 135, 13804–13813.
(57) Wang, L. P.; Van Voorhis, T. J. Phys. Chem. Lett. 2011, 2, 2200–2204.
(58) Ullman, A. M.; Liu, Y.; Huynh, M.; Bediako, D. K.; Wang, H.; Anderson, B. L.; Powers, D. C.; Breen, J. J.; Abruña, H. D.; Nocera, D. G. J. Am. Chem. Soc. 2014, 136, 17681–17688.
(59) Sartorel, A.; Genoni, A.; LaGanga, giuseppina; Volpe, A.; Puntoriero, F.; Di Valentin, M.; Bonchio, M.; Natali, M. Faraday Discuss. 2015. doi:10.1039/C5FD00076A.
(60) Wu, J. Z.; Sellitto, E.; Yap, G. P. A.; Sheats, J.; Dismukes, G. C. Inorg. Chem. 2004, 43, 5795–5797.
(61) Mattioli, G.; Giannozzi, P.; Amore Bonapasta, A.; Guidoni, L. J. Am. Chem. Soc. 2013, 135, 15353–15363.
(62) Ruettinger, W.; Yagi, M.; Wolf, K.; Bernasek, S.; Dismukes, G. C. J. Am. Chem. Soc. 2000, 122, 10353–10357.
(63) Wu, J. Z.; De Angelis, F.; Carrell, T. G.; Yap, G. P. A.; Sheats, J.; Car, R.; Dismukes, G. C. Inorg. Chem. 2006, 45, 189–195.
(64) Brimblecombe, R.; Swiegers, G. F.; Dismukes, G. C.; Spiccia, S. Angew. Chem. Int. 2008, 47, 7335–7338.
(65) Brimblecombe, R.; Kolling, D. R. J.; Bond, A. M.; Dismukes, G. C.; Spiccia, L.; Swiegers, G. F. Inorg. Chem. 2009, 48, 7269–7279.
(66) Hara, M.; Waraksa, C. C.; Lean, J. T.; Lewis, B. A.; Mallouk, T. E. J. Phys. Chem. A 2000, 104, 5275–5280.
(67) Liu, H.; Schilling, M.; Yulikov, M.; Luber, S.; Patzke, G. R. ACS Catal. 2015, 4994–4999.
(68) Davenport, T. C.; Ahn, H. S.; Ziegler, M. S.; Tilley, T. D. Chem. Commun. 2014, 50, 6326–6329.

(69) Parent, A. R.; Crabtree, R. H.; Brudvig, G. W. Chem. Soc. Rev. 2013, 42, 2247–2252.
(70) Demars, T. J.; Bera, M. K.; Seifert, S.; Antonio, M. R.; Ellis, R. J. Angew. Chemie Int. Ed. 2015, 54, 7534–7538.
(71) Cady, C. W.; Gardner, G.; Maron, Z. O.; Retuerto, M.; Go, Y. B.; Segan, S.; Greenblatt, M.; Dismukes, G. C. ACS Catal. 2015, 3403–3410.
(72) Frisch, M. J.; Trucks, G. W.; Schlegel, H. B.; Scuseria, G. E.; Robb, M. A.; Cheeseman, J. R.; Scalmani, G.; Barone, V.; Mennucci, B.; Petersson, G. A.; Nakatsuji, H.; Caricato, M.; Li, X.; Hratchian, H. P.; Izmaylov, A. F.; Bloino, J.; Zheng, G.; Sonnenberg, J. L.; Hada, M.; Ehara, M.; Toyota, K.; Fukuda, R.; Hasegawa, J.; Ishida, M.; Nakajima, T.; Honda, Y.; Kitao, O.; Nakai, H.; Vreven, T.; Montgomery, J. A., Jr.; Peralta, J. E.; Ogliaro, F.; Bearpark, M.; Heyd, J. J.; Brothers, E.; Kudin, K. N.; Staroverov, V. N.; Kobayashi, R.; Normand, J.; Raghavachari, K.; Rendell, A.; Burant, J. C.; Iyengar, S. S.; Tomasi, J.; Cossi, M.; Rega, N.; Millam, J. M.; Klene, M.; Knox, J. E.; Cross, J. B.; Bakken, V.; Adamo, C.; Jaramillo, J.; Gomperts, R.; Stratmann, R. E.; Yazyev, O.; Austin, A. J.; Cammi, R.; Pomelli, C.; Ochterski, J. W.; Martin, R. L.; Morokuma, K.; Zakrzewski, V. G.; Voth, G. A.; Salvador, P.; Dannenberg, J. J.; Dapprich, S.; Daniels, A. D.; Farkas, Ö.; Foresman, J. B.; Ortiz, J. V.; Cioslowski, J.; Fox, D. J. Gaussian 09, Revision A.1; Gaussian, Inc.: Wallingford, CT, 2009.
(73) Becke, A. D. J. Chem. Phys. 1993, 98, 5648-5652.
(74) McLean, A. D.; Chandler, G. S. J. Chem. Phys. 1980, 72, 5639-5648.
(75) Krishnan, R.; Binkley, J. S.; Seeger, R.; Pople, J. A. J. Chem. Phys. 1980, 72, 650-654
(76) Cossi, M.; Rega, N.; Scalmani, G.; Barone, V. J. Comput. Chem. 2003, 24, 669–681.
(77) Cossi, M.; Barone, V. J. Chem. Phys. 2001, 115, 669-681.

Chapter 4 Water Oxidation Activity by Manganite (γ-MnOOH) Occurs Exclusively via Corner Sharing $Mn^{3+}O_6$ Octahedra

4.1 Abstract

In both photochemical and electrochemical testing assays, corner-sharing octahedra of Mn^{3+} and Mn^{4+} show different activity for water oxidation. This is realized herein, where we compare pure phase oxides consisting of Mn sites in either +3 (manganite, γ-MnOOH) or +4 (pyrolusite, β-MnO_2) oxidation states located above 1x1 tunnel vacancies. Like all other crystalline Mn^{4+} oxides, pyrolusite exhibits poor catalytic activity, while manganite shows significantly higher activity that deactivates in parallel with the appearance of Mn^{4+} and disappearance of crystallographically defined Mn^{3+} corner-sharing octahedra. In extension to crystalline 2D-layered birnessites (δ-MnO_2), the hexagonal structural archetype, containing out-of-layer corner-sharing Mn^{3+} octahedra, shows higher photoactivity than the triclinic polymorph containing in-plane edge-sharing Mn^{3+}. This difference is only seen at high mass loading, as both crystalline birnessites exhibit much lower activity than γ-MnOOH and other polymorphs containing high Mn^{3+} content (Mn_2O_3, Mn_3O_4). These electronic and structural correlations point towards the more flexible topologies for catalysis and enabled water binding by Mn^{3+} sites, in contrast to rigid layered topologies that are more conducting and thus unsuited, by design, to localize four holes necessary for water oxidation.

4.2 Introduction

The omnipresent $CaMn_4O_5$ catalyst for water oxidation in natural photosynthesis has inspired the development of Mn-oxides as artificial catalysts. From multiple reports, there exists a correlation between Mn^{3+} content and catalytic activity for the oxygen evolution reaction (OER).[1–11] Strategies to improve activity from Mn-oxides thus must consider stabilizing Mn^{3+} against the disproportionation reaction into Mn^{4+} and Mn^{2+} (eqn. 1).

$$2Mn^{3+}OOH + 2H+ \leftrightarrow Mn^{4+}O_2 + Mn^{2+} + 2H_2O \qquad (1)$$

This reversible equilibrium has been studied by a number of groups independent of catalysis applications, and commonly, $Mn^{3+}OOH$ polymorphs have been reported at least as intermediates[12] and often as products.[13–17] These compounds allow testing whether Mn^{3+} in some crystallographically defined structures is more active than in others. We sought to pursue this line of research as we have shown $LiMn_2O_4$ (~50% Mn^{3+}) is an exception to the general trend: it is a poor water oxidation catalyst both in photochemical[18] and electrochemical[6] assays. The most stable MnOOH is manganite (γ-MnOOH). The manganite structure consists of corner-linked $Mn^{3+}O_6$ octahedral chains that form proton-containing 1x1 tunnel units (Figure 4.1). Manganite can be considered as a 1 e^- reduced, distorted derivative of pyrolusite (β-MnO_2), with elongated octahedra as a result of Jahn-Teller distortions and hydrogen bonding.[19] In each octahedron, two long (2.27 Å) and four short (1.93 Å) Mn-O bonds reflect an average of 2.04 Å; an 8% increase over the symmetrical Mn^{4+} sites in β-MnO_2 (1.89 Å. average). The Mn-Mn distance is also elongated, though more so for corner-sharing octahedra (9%, 3.76 vs. 3.42 Å) than for octahedra in the same chain (2.88 vs. 2.87 Å).

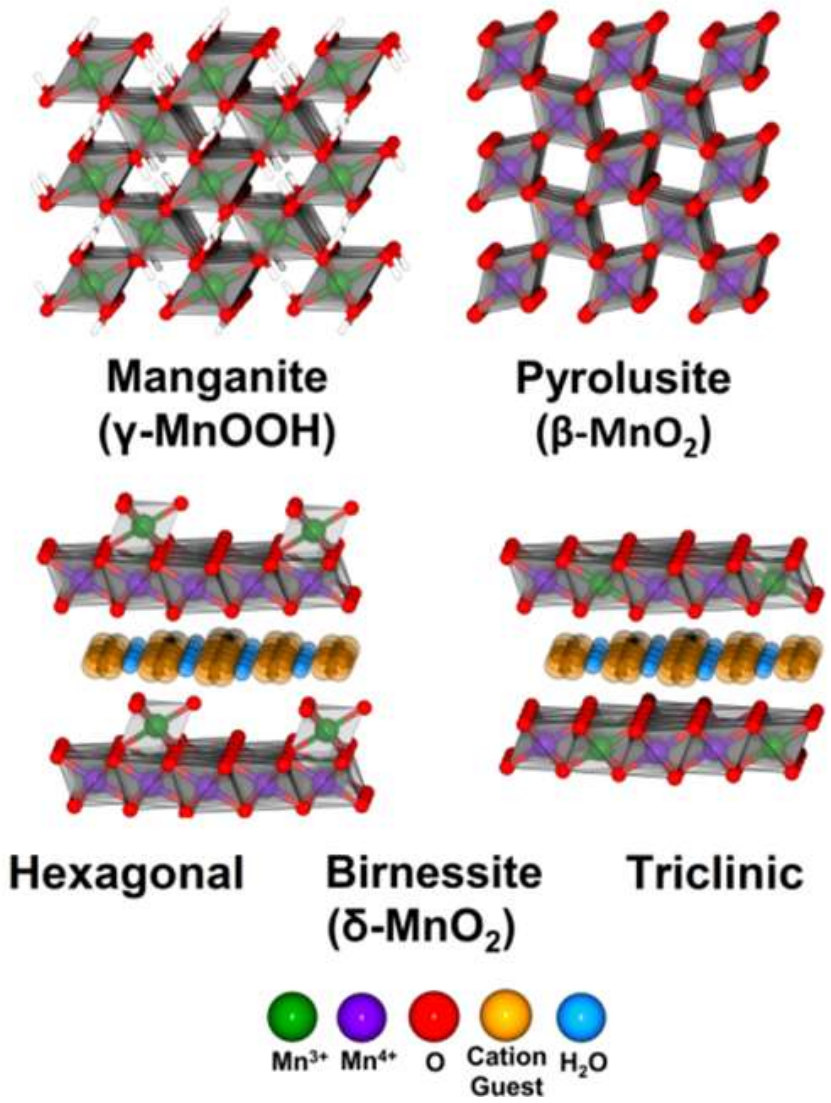

Figure 4.1. Structural depictions of several Mn-oxides.

The presence of corner-sharing Mn octahedra in amorphous electrodeposited manganese oxides (sometimes referred to loosely as birnessite-like) has been correlated with water oxidation activity in the EXAFS studies by Dau and coworkers.[20] Crystallographically defined birnessites having long range order provide a complementary approach for studying corner-shared Mn^{3+} octahedra, as there exist two structural archetypes: hexagonal (HexBir) and triclinic (TriBir). Both materials consist of sheets of edge-sharing MnO_6 octahedra separated by interstitial hydrated cations (Figure 4.1). TriBir contains Mn^{3+} octahedra within the MnO_2 sheets, while the reduced charge is compensated by interlayer spectator cations (here, K^+). In contrast, HexBir does not stabilize Mn^{3+} within sheets; instead these sites are vacancies with Mn^{3+} located above or below the vacancy in the interlayer (or surface) bonded *via* corner-sharing bridges. Hexagonal birnessites are, in general, poorly crystalline due to the potential build-up of disordered vacancies. Poorly crystalline birnessites correlate with higher catalytic activity in multiple studies,[21–25] in contrast to triclinic birnessites which are reported to exhibit low (or zero) activity for water oxidation.[4,21,26] Collectively, these results predict corner-sharing Mn^{3+} are highly active catalytic sites.

We report here the results of three investigations of corner-shared Mn^{3+} polytypes as an effective structural motif for water oxidation above pH 7. In the first two series of experiments, γ-MnOOH shows a significantly lower overpotential than β-MnO_2 for both electrocatalytic and photocatalytic water oxidation. In the third investigation, a crystalline hexagonal structural archetype of birnessite shows significantly higher photolytic water oxidation than the triclinic form. Collectively, these results clearly demonstrate corner-sharing Mn^{3+} octahedra are the main predictor for water oxidation catalysis, while edge-

sharing Mn^{3+} and corner-sharing Mn^{4+} are not significant contributors. Few reports are available that test $Mn^{3+}O_6$ polytypes in structurally well-defined (crystalline) materials,[4,26] and only one report has examined pure phase manganite for water oxidation (though structural characterization was absent in that case).[27]

4.3 Experimental

Materials. All solutions were prepared with reagent grade water (18 MΩ, Hydro Picopure). All solvents and reagents were reagent grade, purchased commercially and used without further purification. This study utilized bixbyite (Mn_2O_3, 16.3 m^2/g), pyrolusite (β-MnO_2, 14.9 m^2/g), and hausmannite (Mn_3O_4, 27.2 m^2/g) which have been described previously[4]. Tested birnessites for this study included triclinic δ-MnO_2 (17.9 m^2/g) (ref. 4) and HexBir (5 m^2/g) (ref. 25). 20% Ir@C (vulcanized) was purchased from Premetek.

Preparation of Manganite. The literature procedure[28] was adapted as follows. 1 M HNO_3 (40 mL) containing 2 g sucrose was stirred at room temperature, and 200 mL of water containing 5.89 g $KMnO_4$ was added, followed by 4.4 g of $MnSO_4 \bullet H_2O$. The solution was refluxed for 6 hr. Hot filtration recovered a brown solid which was washed with water and air dried. Note: Manganite is not stable above 250°C.

Electrochemistry. A CH Instruments Electrochemical Workstation was used. Working electrodes were prepared as follows: A solution of Nafion (5%) was brought to pH 7 by addition of ~½ volume equivalent 0.1 M NaOH. This Nafion was diluted with ethanol and water in a volume ratio of 4:4:5. To this solution, acetylene black (1 mg/mL) and Mn-oxide (20 mg/mL) were added and dispersed via sonication. For most measurements, 5 µL of suspension were dropcast on a 5mm diameter glassy carbon electrode. The resulting electrochemical current from these catalyst-film electrodes was normalized to the geometric area. For large scale measurements of Faradaic efficiency, and to isolate the post-reaction product, 200 µL were dropcast onto 1.5x1.5 cm stainless steel mesh (pretreated in 30% HNO_3 for 30 min), connected via Cu tape to Ti wire. Following

analysis, films were sonicated into ethanol; water was added and then the sample was centrifuged. Upon assembly all electrodes had less than 10 Ω resistance at pH 14, and 20 Ω resistance at pH 7. CV's were IR-corrected (95%), initiated at the open circuit potential, and performed at 10 mV/s scan rate with vigorous stirring. Ti wire was used as a counter electrode. Reference electrodes were Ag/AgCl (pH 7) and Hg/HgO (pH 14). Silver reference electrodes were externally calibrated against SCE and did not deviate by more than 5 mV. Overpotentials were calculated by Overpotential = Measured potential – (1.23 V – (0.059*pH)-E (ref. electrode)) using +0.100 V for Hg/HgO and +0.240 V for SCE.

Powder X-ray Diffraction (PXRD). Patterns were recorded on a Rigaku Ultima IV X-ray diffractometer, using Cu Kα radiation (λ=1.5406 Å). A graphite monochromator was used and the generator power settings were set to 40 kV and 44 mA. Data were collected between 2θ of 3-50° with a step size of 0.02° and a scan speed of 2.5 deg/min.

BET. Surface area measurements were made by N_2 gas adsorption at 77K on a volumetric gas sorption analyser (Autosorb-1 MP, Quantachrome Instruments). 100 mg of sample was prepared by outgassing under vacuum at 120°C for 1 hour.

Xray Photoelectron Spectroscopy (XPS). A Thermo K-Alpha spectrometer was used with charge compensation; spectra were calibrated against adventitious carbon. Solid samples were fixed on carbon tape and a beam of 150 μm diameter was focused on an area covered by the powdered sample. Deconvolution was performed as previously described.

Scanning and Transmission Electron Microscopy (SEM, TEM). A JOEL 2010F TEM/STEM with EDS and EELS attachments was used for the high resolution (HRTEM) and electron diffraction (SAED) microscopy observations. The scope was operated at 200KeV with resolution better than 1.5 Angstrom in both imaging and scanning modes. SEM measurements were performed on a FEI Quanta 200 FEG Environmental- Scanning Electron Microscope. ICP analysis was performed on a Perkin Elmer Optima 7300 ICP-OES.

O_2 Evolution. A Clark type oxygen electrode (Hansatek Ltd) was used to obtain oxygen evolution data, and calibrated daily using N_2 deoxygenated and oxygen saturated atmospheric solutions. Manganese oxides were dispersed into solution with final concentrations 0.5 mM $Ru(bpy)_3^{2+}$, 10 mM $Na_2S_2O_8$, 0.1 M pH 7 bicarbonate buffer and subjected to visual light illumination (light profile is described in ref[29]).

4.4 Results and Discussion

Of several techniques examined, successful synthesis of γ-MnOOH was best reproduced from the method described by Suib, et. al[28]. Figure 4.2B shows that the PXRD pattern agrees, both in peak positions and intensities, with a MnOOH structural reference (ICSD-84949).[19] High-resolution transmission electron microscopy (HRTEM) and SAED patterns further confirm manganite lattice spacings (Table 4.1) and structural homogeneity extending over the entire nanocrystallite domain size (Figure 4.2A and Figure 4.3). Consistent with the report of Suib et. al., SEM images indicated a nanostructured powder with pill-shape morphology of average dimensions 150 nm x 30 nm (Figure 4.2A and Figure 4.3). The sample has a surface area of 50 m^2/g as determined by BET N_2 gas absorption (Figure 4.4).

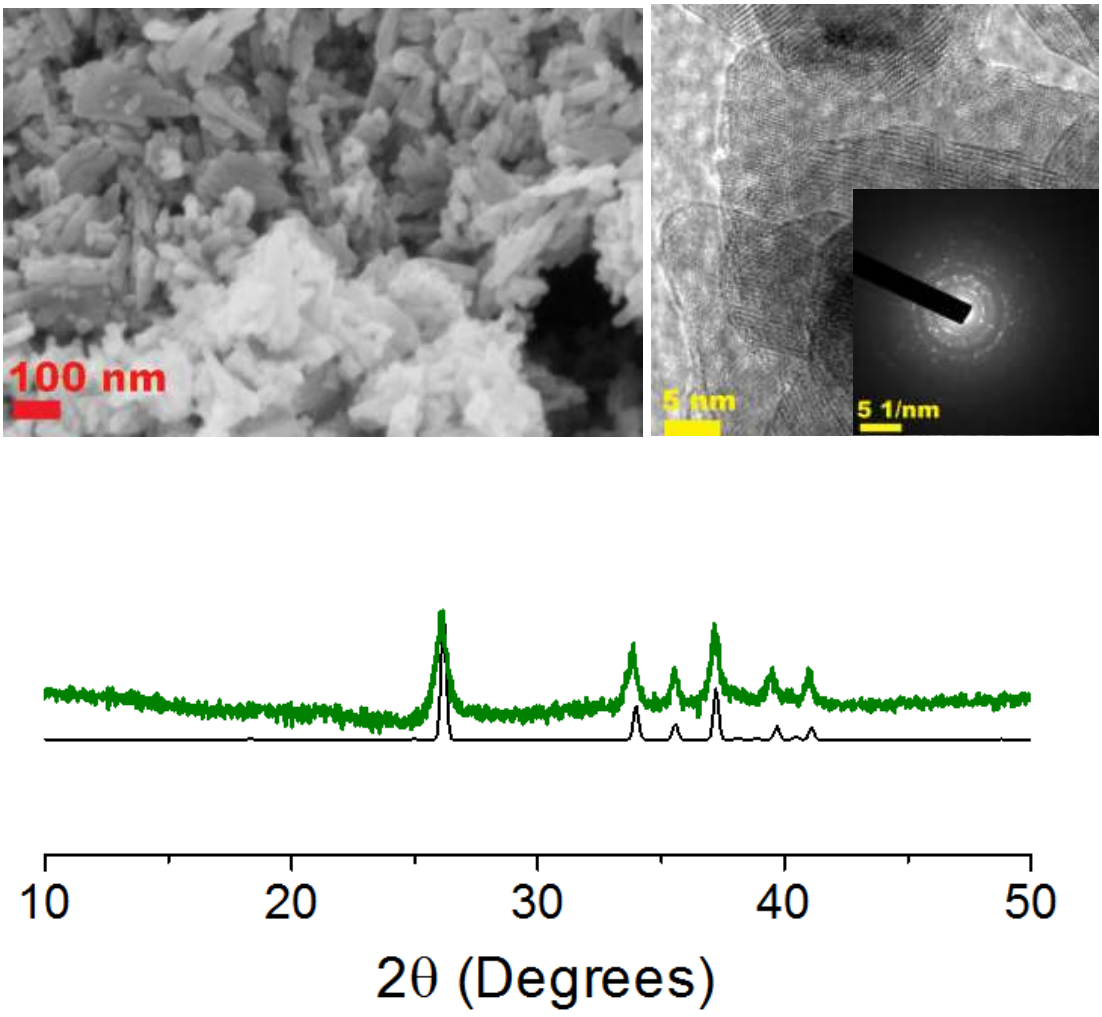

Figure 4.2. Characterization of γ-MnOOH: SEM (top left), TEM and SAED (top right) and PXRD **(**green**)** with structural reference[16] (black).

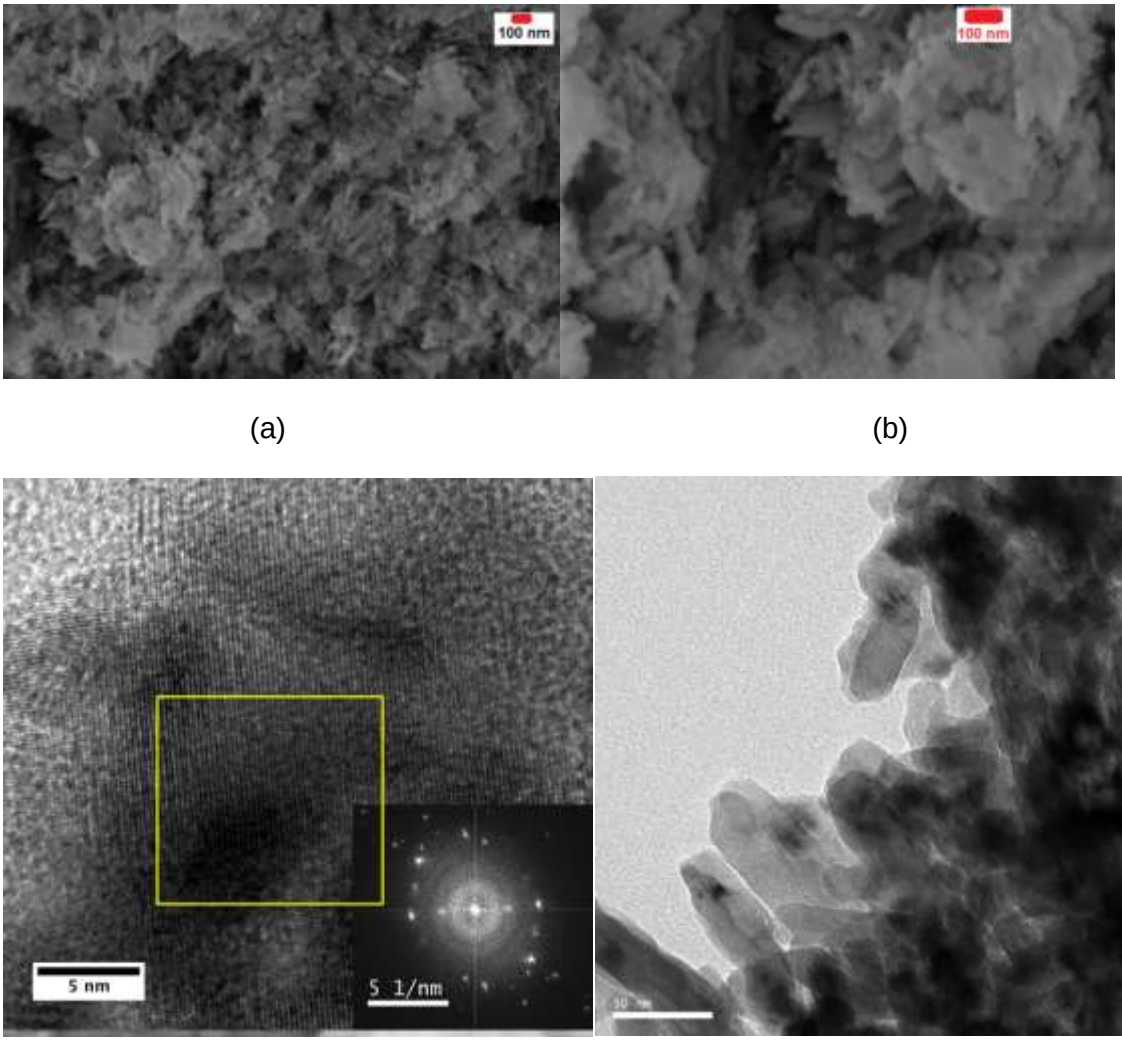

Figure 4.3: Electron Microscopy images for manganite as-prepared. (a) and (b) are SEM micrographs. (c) High resolution TEM micrograph with corresponding fourier transform pattern (inset). (d) low magnification TEM micrograph showing elongated nanostructured morphology (pill-shape)

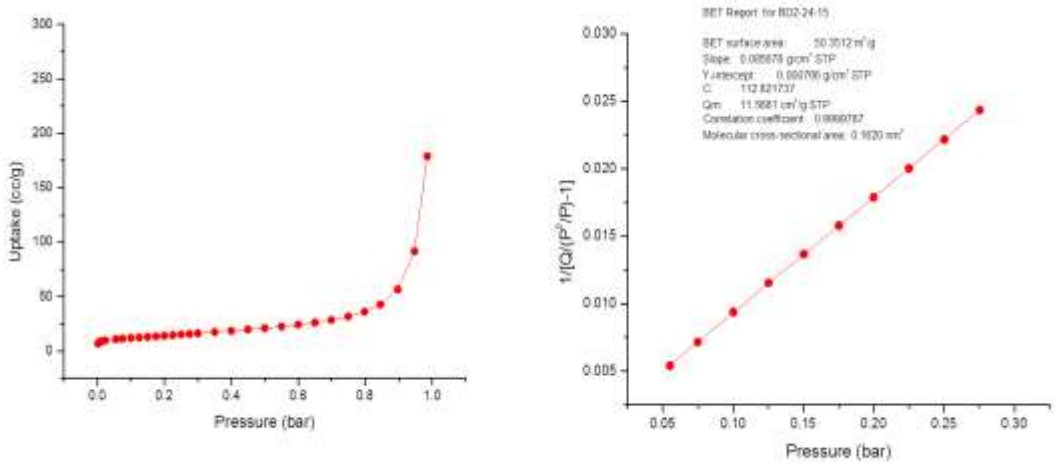

Figure 4.4: N_2 adsorption data for as-made manganite.

OER activity of this phase was tested *via* electrochemical techniques (pH 7 and 14), and by using a well-known assay based on photooxidation of $Ru(bpy)_3^{2+}$ (bpy= 2,2' bipyridine) in buffered persulfate (pH 7).[30] Manganite is known to disproportionate to MnO_2 below pH 6,[31–34] hence no assays below this pH were pursued. Figure 4.5 shows that thin films of γ-MnOOH nanoparticles (supported within pH-neutralized Nafion) on glassy carbon electrodes exhibit significant catalytic activity for water oxidation at pH 7 and 14. We adopt as benchmark the overpotential required for 10 mA/cm^2 current density,[35,36] which γ-MnOOH electrodes with 0.5 mg/cm^2 loading achieved at η = 530 mV (1 M NaOH) and 680 mV (1 M phosphate buffer). The observed catalytic wave (Figure 4.5) produces O_2 as measured by gas chromatography (Figure 4.6). A Faradaic efficiency of 97% was obtained after 50 C charge passed, as calibrated against O_2 produced from Ir/C (Premetek).

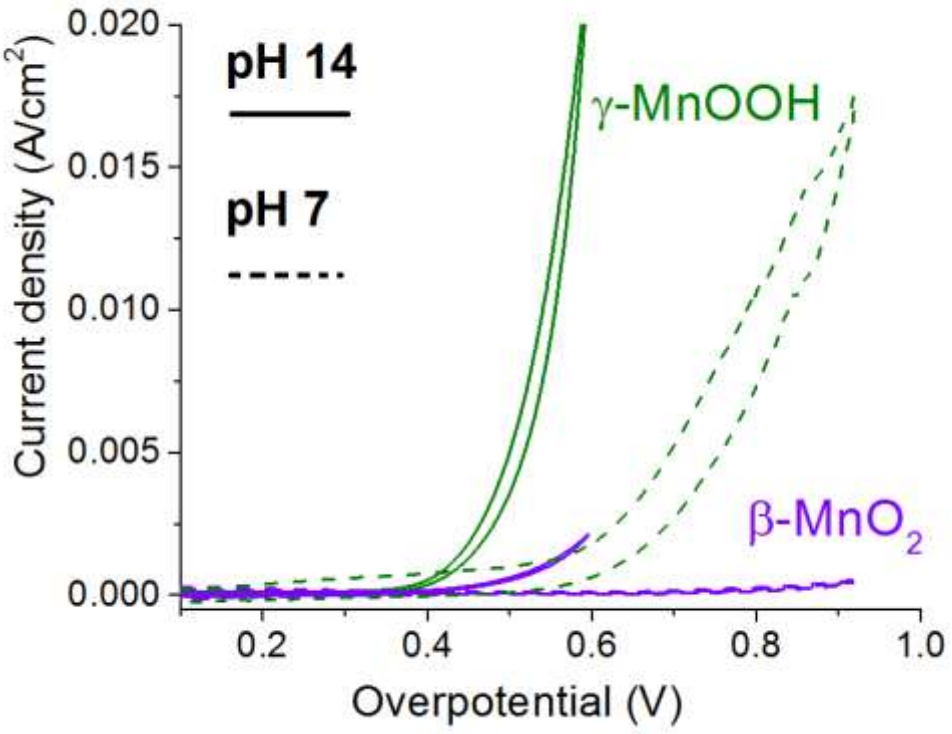

Figure 4.5. Cyclic voltammograms (10 mV/s, IR-corrected) for the 1x1 tunnel manganese oxides of Figure 1 in 1 M NaOH or 1 M phosphate buffer, loading =0.5 mg/cm^2. Conditions: 5mm glassy carbon working electrode, Ti counter electrode, reference electrodes Hg/HgO (pH 14, E_{ref} = +0.100 V vs. NHE) and Ag/AgCl ref (pH 7). The silver reference electrode was externally calibrated vs SCE (E_{ref} = +0.240 V vs. NHE). Overpotentials are corrected for the pH dependence of water oxidation and given relative to each reference electrode using the expression: Measured potential – (1.23 V – (0.059*pH)-E_{ref}). Current is normalized to geometric electrode area.

Measured (A^o)	(facet)	84949 Std (A^o)
4.394	(100)	4.83
3.524	(111)	3.41
2.762	(020)	2.64
2.497	(002)/(200)	2.42
2.309	(12-1)	2.27
1.834	(022)/(220)	1.78
1.726	(11-3)/(31-1)	1.67
1.548	(131)	1.50
1.474	(202)	1.44
1.361	(113)	1.32

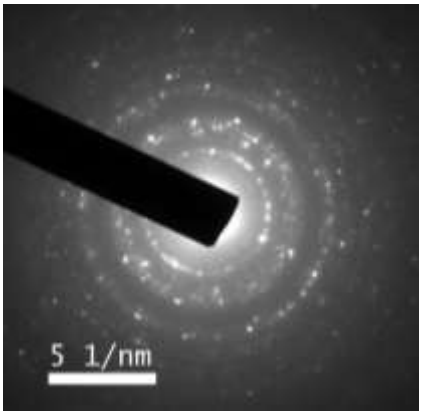

Table 4.1: Selected Area Electron Diffraction (SAED) pattern with corresponding measured d-spacings of the as prepared Manganite.

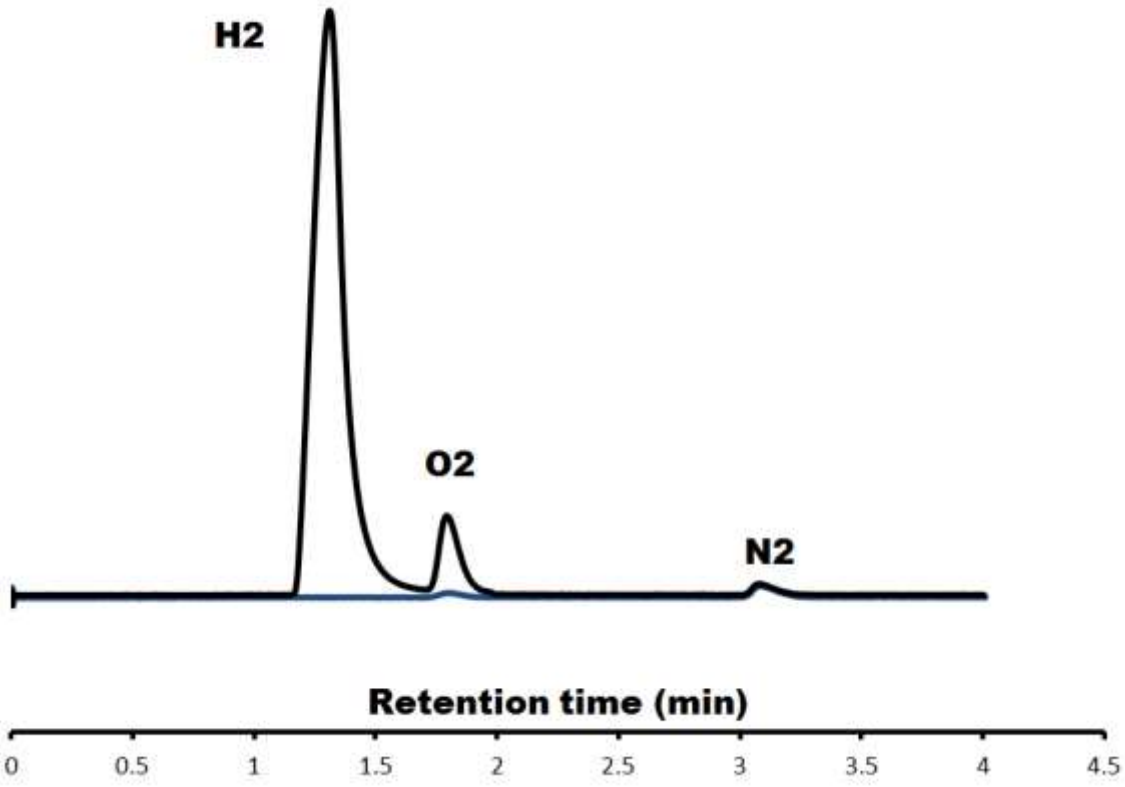

Figure 4.6: Representative gas chromatograms from headspace gas above water splitting cells (MnOOH anode, Ti cathode) from pH 14 solution. Blue: Ar-purged chamber before, black: following bulk electrolysis at 600 mV overpotential.

The application of oxidizing potential to γ-MnOOH sufficient to form Mn^{4+} could be hypothesized to form β-MnO_2 (see structures, Figure 1). Literature is divided over the efficacy of β-MnO_2 to catalyze water oxidation,[4,23,37–39] though this can be ascribed to different testing conditions, as recently concluded by Stahl et. al.[26] The β-MnO_2 we isolated previously only demonstrated activity in the presence of an Mn_2O_3 impurity.[4]

Figure 4.5 shows that under electrochemical conditions employed herein, an identical mass loading of pure phase β-MnO_2 could not account for activity exhibited by γ-MnOOH. Further, no apparent $Mn^{3+} \rightarrow Mn^{4+}$ feature is seen before the catalytic wave of γ-MnOOH. This analysis suggests that the Mn^{3+} oxidation lies within the catalytic wave and thus involves removal of electrons from a hybridized Mn-oxide band.

The performance of the γ-MnOOH film electrode gradually deactivates during repetitive CV cycling through the catalytic wave or during bulk electrolysis at O_2 evolving potentials (Figure 4.7). At pH 14 and 500 mV overpotential, films which passed 2-3 electrons/Mn showed a gradual, continuous decrease in activity from 5 mA/cm^2 to 1.9±0.4 mA/cm^2 over 20 minutes. This gradual loss of 60% activity was due to catalyst deactivation and not film delamination as current densities obtained from films prepared identically except containing stable catalysts were sustained.[6] Intentional mechanical delamination of catalyst films instead showed sharp, sudden drops in current (Figure 4.7). Even sonication of electrode films in water failed to remove samples from the electrode (sonication in ethanol allowed isolation of postreaction samples, see below). Further, ICP analysis of the post-reaction electrolyte (either pH 7 or 14) revealed only minor quantities (between 0.02 - 0.1%) of the total Mn originally loaded onto the electrode. While we do not exclude the possibility of some Mn leeching, this quantity cannot account for 60%

deactivation. As described next, we identified structural changes consistent with disordering of the starting γ-MnOOH in parallel with buildup of Mn^{4+}.

We compared films before and after passing 4 charge equivalents/Mn in 1 M NaOH at 550 mV overpotential. Despite positive detection of γ-MnOOH by PXRD in unreacted films (Figure 4.8), this technique indicated no identifiable crystalline phase in the postreaction sample. For greater sensitivity, HRTEM was pursued. Micrographs of individual postreaction particles revealed a high degree of uniformly spaced 2-D layers within individual domains and with random orientations (semi-crystalline) and sizes (Figure 4.9-4.10). Lattice fringes showed significant curvature. The crystalline domains were smaller in size relative to the starting γ-MnOOH, and these regions showed increases in measured d-spacings (Figure S6). The most prominent SAED spacing observed (the 111 facet) increased from 3.52 to 3.58 Å; a ~2% increase. This facet refers to the plane containing the protons within the tunnels (Figure 4.9), and its increase in size suggests protons are removed during catalysis, leaving behind an elongated tunnel structure absent of any hydrogen bonding. We note that the MnO_2 2x1 tunnel structure (ramsdellite) is accessible from manganite both by protonation,[31] and natural oxidation/weathering processes.[40] Hence, there is precedence that manganite tunnel size may increase.

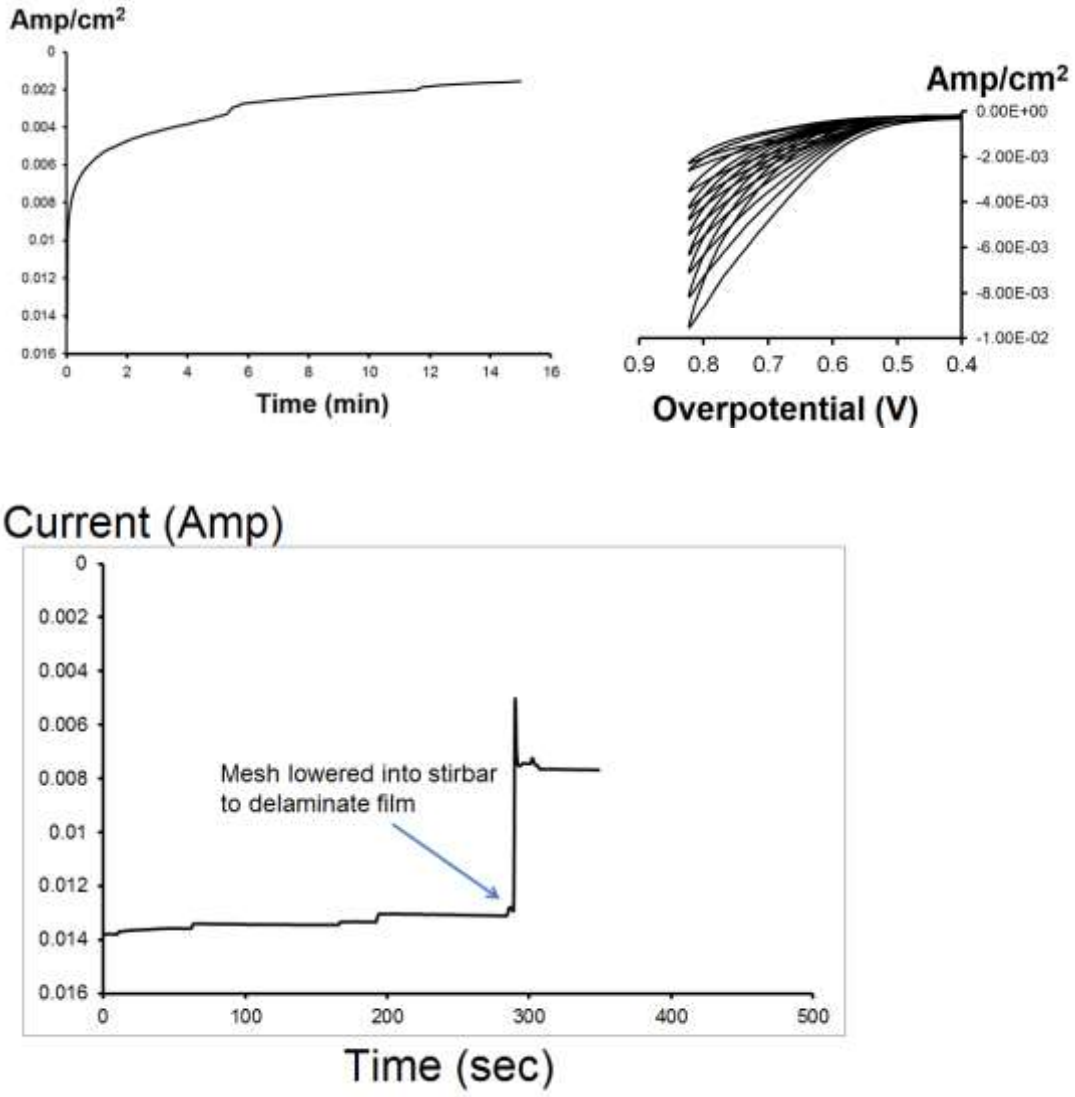

Figure 4.7: Representative data showing deactivation of γ-MnOOH electrodes. Top left: bulk electrolysis at η=500 mV, pH 14. Top right: subsequent CV scans at pH 7 (trend indicated by red arrow). Bottom: Representative manganite sample affected by film delamination.

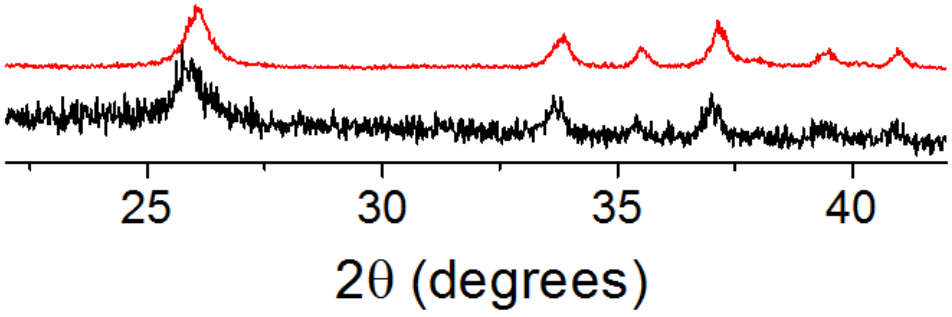

Figure 4.8: Positive detection of as prepared manganite (red) in unreacted nafion films (black).

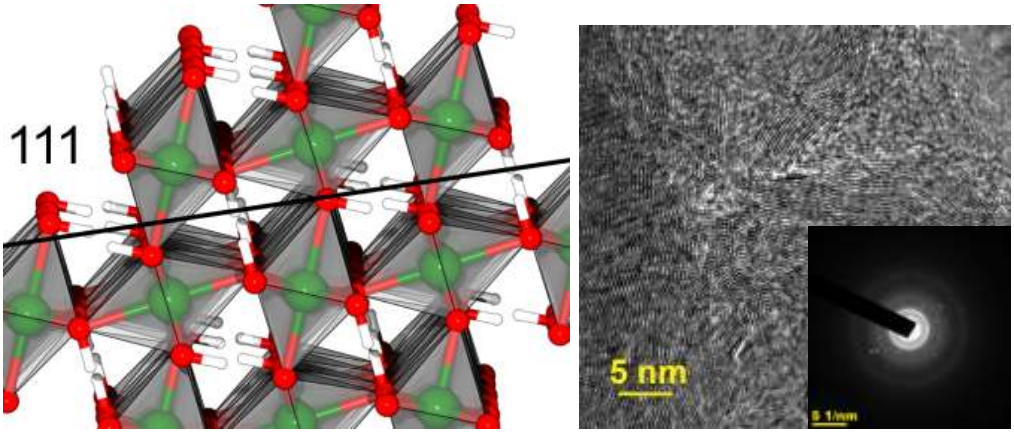

Figure 4.9. Postreaction characterization of electrochemically oxidized γ-MnOOH. Left: The 111 cut plane containing the protons. Oxygen=red, Manganese= purple. Right: Sample HRTEM and SAED pattern.

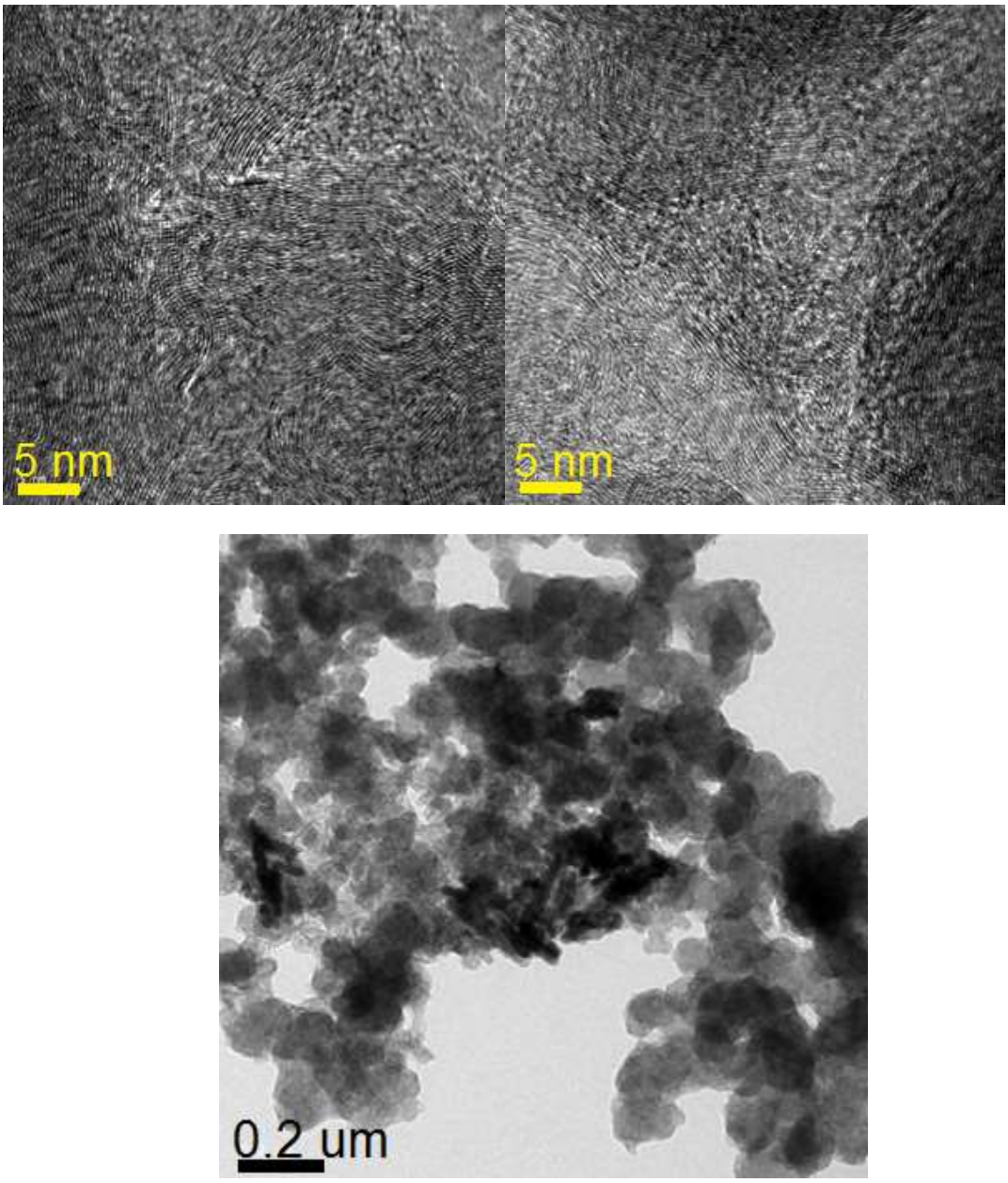

Figure 4.10: Low and High magnification Transmission Electron Microscopy Micrographs for manganite post-electrochemical bulk electrolysis, pH 14, 500 mV overpotential.

X-ray photoelectron spectroscopy (XPS) was used to examine the surface Mn oxidation states. For as-made γ-MnOOH, the experimentally obtained $Mn2p_{3/2}$ peak binding energy of 641.8 eV agrees excellently with literature values obtained for Mn^{3+} (Mn_2O_3, 641.7-641.9 eV)[41]. We obtained an identical peak using Mn^{3+} acetate (Sigma-Aldrich), and this peak was retained after loading into Nafion (Figure 4.11). Following electrocatalysis, the binding energy shifts to a higher value (642.2 eV), indicating a higher average oxidation state. This lies within the range (641.9-642.6 eV) commonly ascribed to Mn^{4+}.[41] Consistent with this assignment, pure phase β-MnO_2 exhibits a prominent shoulder peak at 642.7 eV (Figure 4.12). We thus assign the appearance of Mn^{4+} in the post-reaction sample. For a more quantifiable surface average oxidation state (AOS), we deconvoluted the $Mn2p_{3/2}$ peak into Mn^{2+}, Mn^{3+} and Mn^{4+} components. Our curve fitting procedure by the method of Nesbitt and Banerjee[42] as described previously[25] gives AOS values of 2.9 and 3.0 for manganite with and without Nafion respectively vs. 3.2 for electrochemically cycled manganite, indicative of Mn^{4+} (see Table S2). We could not gain information from the O_{1s} signal due to interference from the Nafion SO_4 groups.

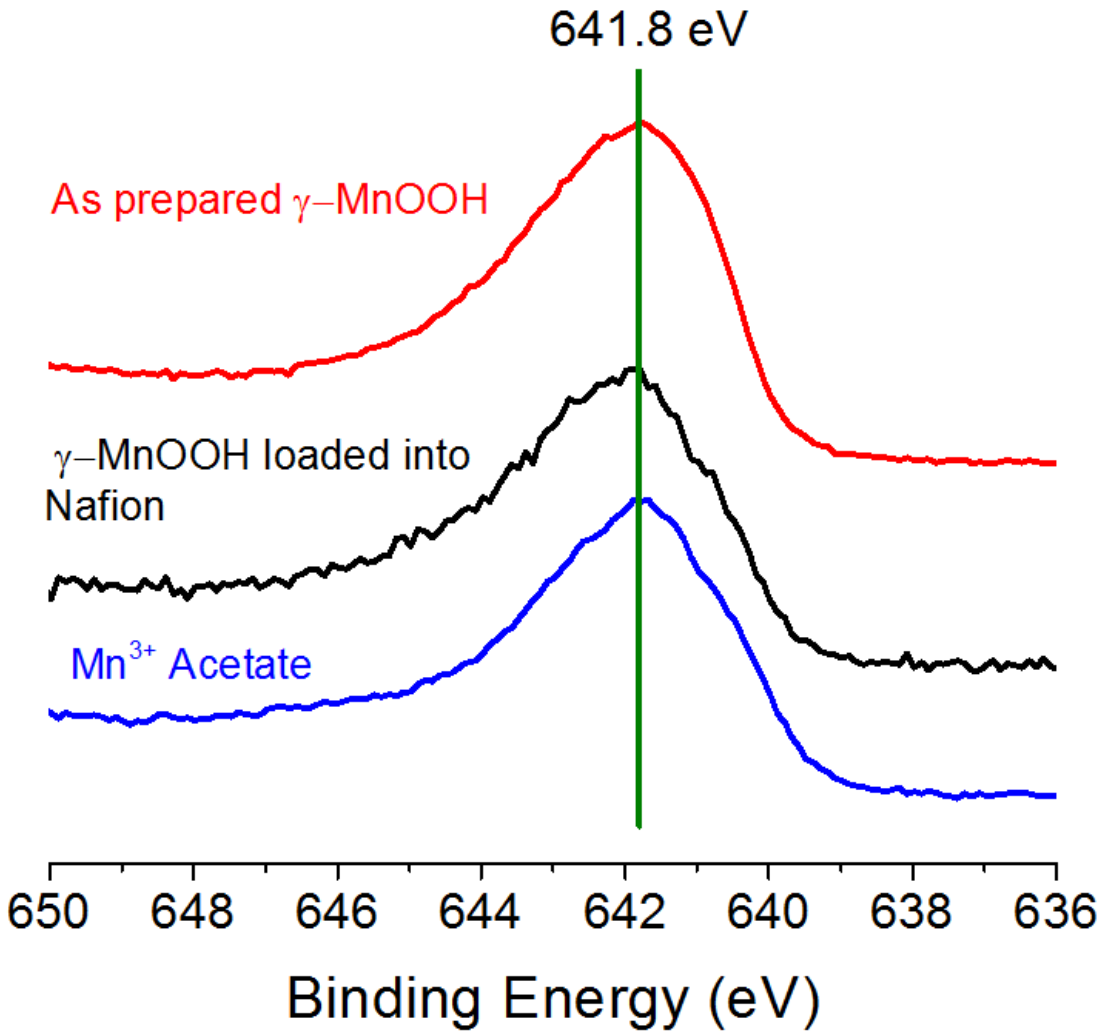

Figure 4.11: $Mn2p_{3/2}$ XPS spectra for as synthesized manganite, unreacted manganite loaded into Nafion, and Mn^{3+} reference.

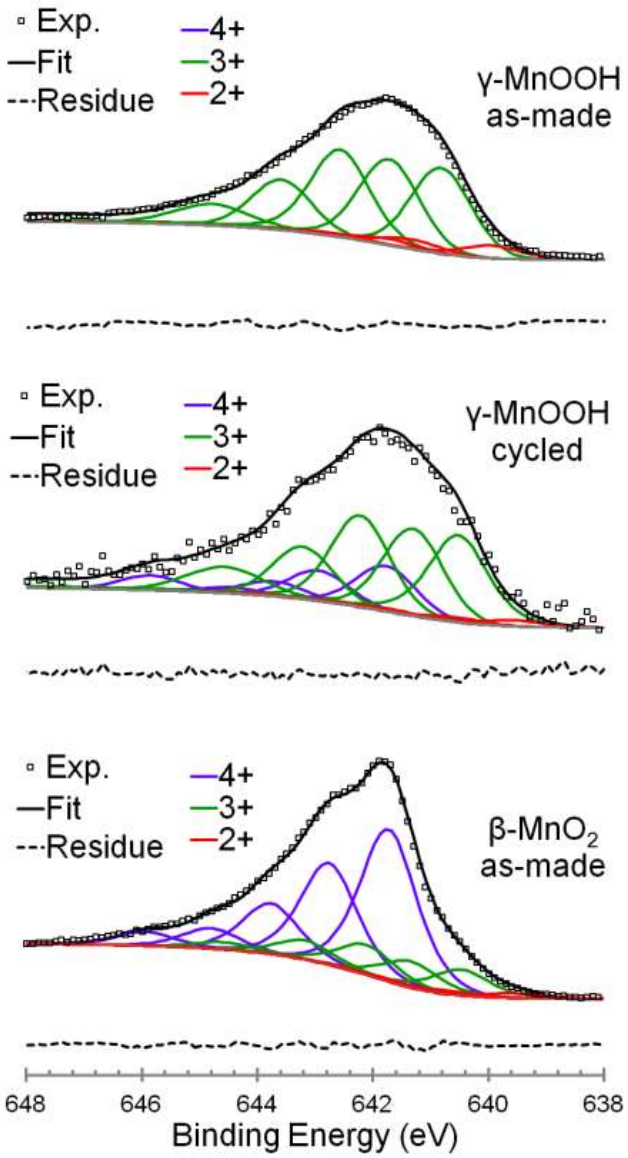

Figure 4.12. Mn 2p3/2 region of XPS spectra comparing γ-MnOOH, β-MnO2, and electrochemically oxidized γ –MnOOH. These spectra are deconvoluted into contributions from Mn^{4+} (purple), Mn^{3+} (green) and Mn^{2+} (red) via the method of Nesbitt and Banerjee[38] as described previously[22].

Sample	Mn4+ (%)	Mn3+ (%)	Mn2+ (%)	Peak binding energy (eV)
MnOOH as made	0	92	8	641.8
MnOOH loaded into Nafion	9	86	5	641.8
MnOOH with $4e^-$ /Mn passed, electrochemically	23	72	5	642.2
MnOOH reacted with $Ru(bpy)_3^{3+}$ for 30 min	46	49	5	642.0

Table 4.2: Estimated relative abundances of Mn oxidation states on depicted surfaces as measured by XPS.

In order to eliminate unknown complications from the polymer component, we expanded our study to γ-MnOOH particles suspended in homogeneous aqueous solutions, using an established photochemical assay to generate photooxidant (0.5 mM $Ru(bpy)_3^{2+}$, 10 mM $Na_2S_2O_8$, 0.1 M pH 7 bicarbonate buffer).[4] The results closely paralleled the electrochemical results from above. Specifically, Clark electrode experiments confirm that γ-MnOOH catalyzes O_2 evolution under these conditions (Figure 4.13). After 30 minutes of illumination, the post-catalysis PXRD pattern indicates an obvious loss of crystallinity, seen as peak broadening, yet with overall retention of the underlying structure (Figure 4.14). This is consistent with the inaccessibility of the $Ru(bpy)_3^{3+}$ cation (~11 Å diameter) into the bulk material.

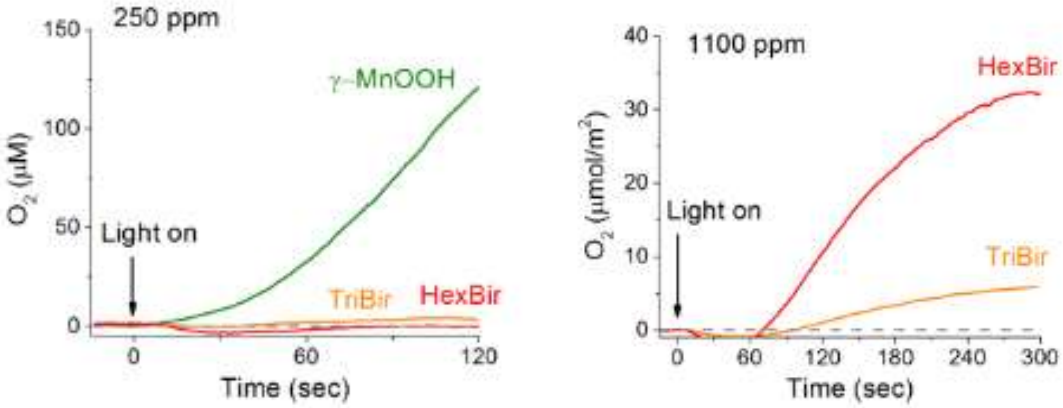

Figure 4.13. Photoinduced O2 production from chemical oxidation of Mn-oxides. Conditions: 0.5 mM $Ru(bpy)_3^{2+}$, 10 mM $Na_2S_2O_8$, 0.1 M pH 7 bicarbonate buffer. The gray line indicates extrapolated baseline.

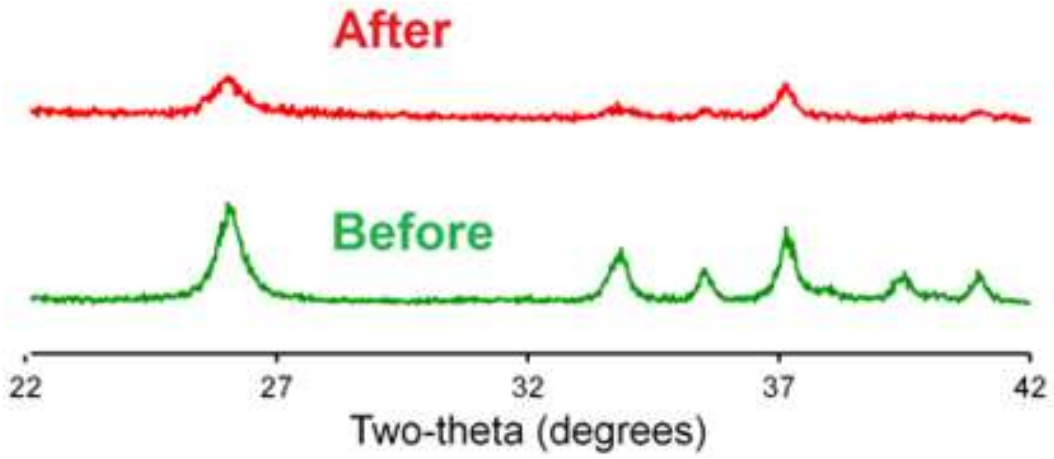

Figure 4.14: PXRD of manganite before and after photochemical water splitting using $Ru(bpy)_3^{3+}$ oxidant.

XPS of the post-reaction manganite from this photochemical assay (Figure 4.15) indicated an AOS increase to 3.4. Consistent with this assignment, the $Mn2p_{3/2}$ binding energy shifts positively from 641.8 to 642.0. As this sample lacks a Nafion component, we were also able to measure the binding energy separation ($\Delta E_{Mn2p3/2\text{-}O1s}$), for which Mn oxides of higher AOS show larger values than more reduced species due to 1) shift of Mn to higher binding energies and 2) growth of O^{2-} at lower binding energies.[43] The increase of ΔE from 110.5 eV (before) to 112.8 eV (after) further verifies the postreaction sample as having a higher AOS. The higher AOS obtained for the photochemical assay at pH 7 vs. electrochemically at pH 14 is rationalized both by the higher stability of Mn^{3+} with increasing pH as well as the method of charge delivery in both assays: in an electrochemical system, electrons follow the path of least resistance and may tunnel through the bulk material, whereas the photochemical reaction depends upon physical collisions of oxidant molecules with the catalyst surface. Regardless, across two charge delivery assays the γ-MnOOH post-catalysis sample indicates formation of a disordered material with more Mn^{4+} comprising the surface. Again, pure phase β-MnO_2 under the same conditions was inactive,[4] and cannot account for the activity ascribed to γ-MnOOH.

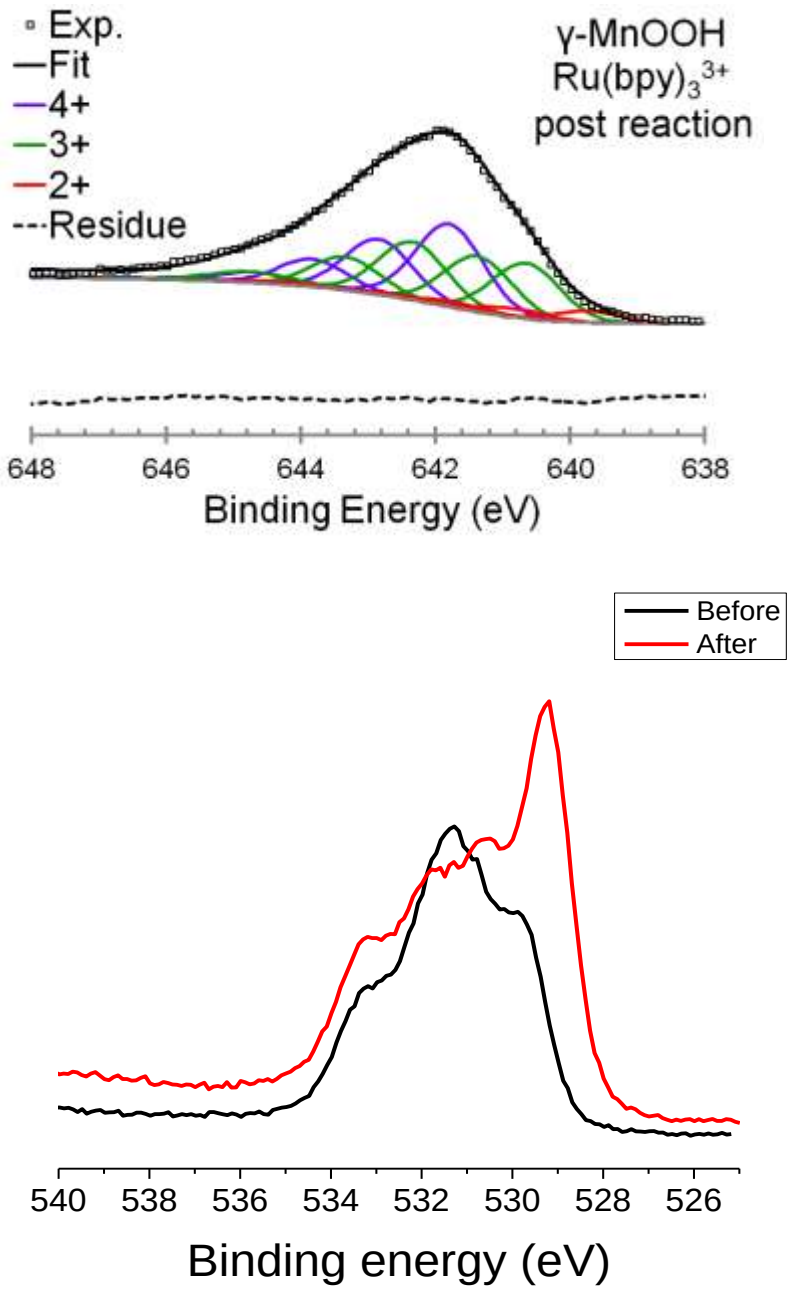

Figure 4.15: XPS spectra for manganite following 30 minute reaction with light-generated Ru(bpy)33+. Deconvoluted $Mn2p_{3/2}$ region (top) and O1s spectrum (bottom) compared to unreacted sample.

The turnover frequency (TOF)/m^2 of γ-MnOOH is comparable to phase pure Mn_3O_4 (hausmannite) from our previous report.[4] Our photochemical and electrochemical results show a striking similar trend in performance across 6 manganese-oxide compounds (Figure 4.16A). This holds true for electrodes at both pH 7 and 14 (Figure 4.16B). Despite having a lower surface area than γ-MnOOH, Mn_2O_3 is once again the most highly active compound. Current density measurements at pH 14 of this compound attains 10 mA/cm^2 at only η=450 mV (Figure 4.17). This value agrees with the results of Ramirez and Fiechter, et. al.,[44] and compares favorably to the report of Suib, et. al. at pH 13 (η = 507 mV)[3]. Like γ-MnOOH this activity is not maintained over time (Figure 4.17).[4,44] The electrochemical activity of Mn_3O_4 (Figure 4.18) is similar to γ-MnOOH at pH 7, while manganite is superior at pH 14 (Figure 4.16B).

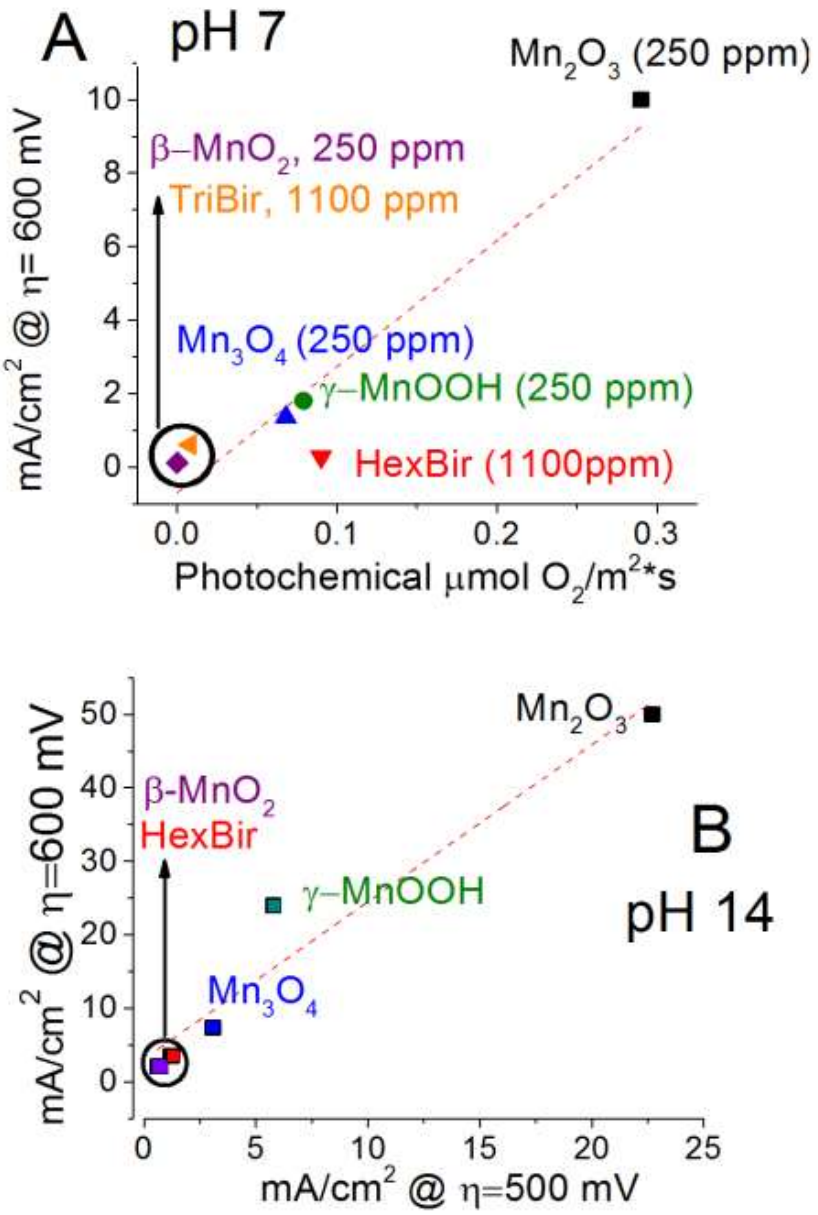

Figure 4.16. Current densities of Mn-oxide compounds obtained from CV's at 0.5 mg/cm^2 electrode loading. Electrochemical conditions are described in Figure 3. **A**: At pH 7, plotted as function of photochemical O_2 generation rates derived either in this work or in ref[4] with depicted loading. **B**: At pH 14 (1M NaOH).

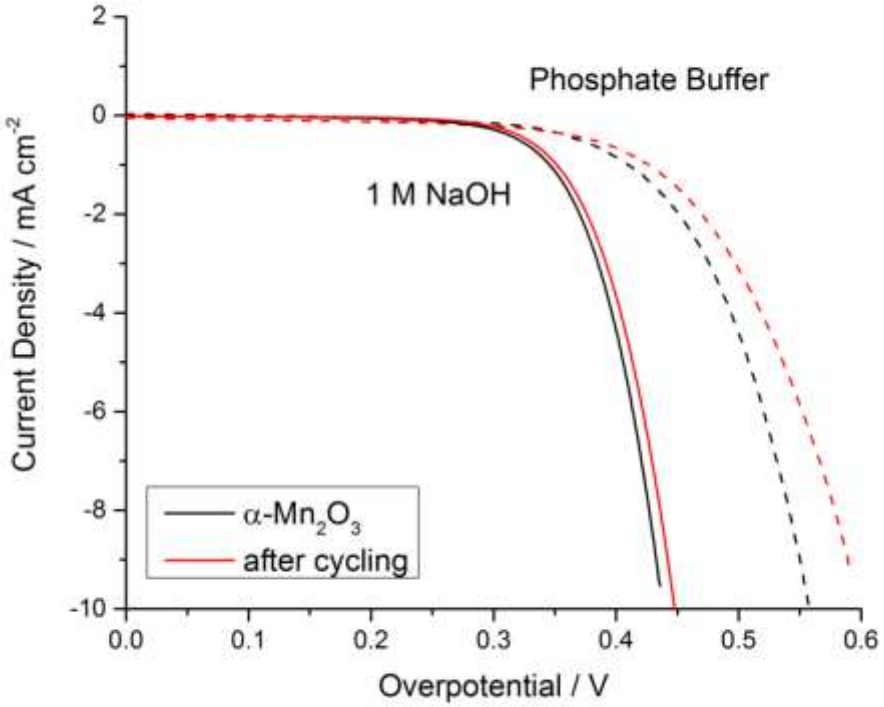

Figure 4.17: Linear voltammetry of Mn_2O_3

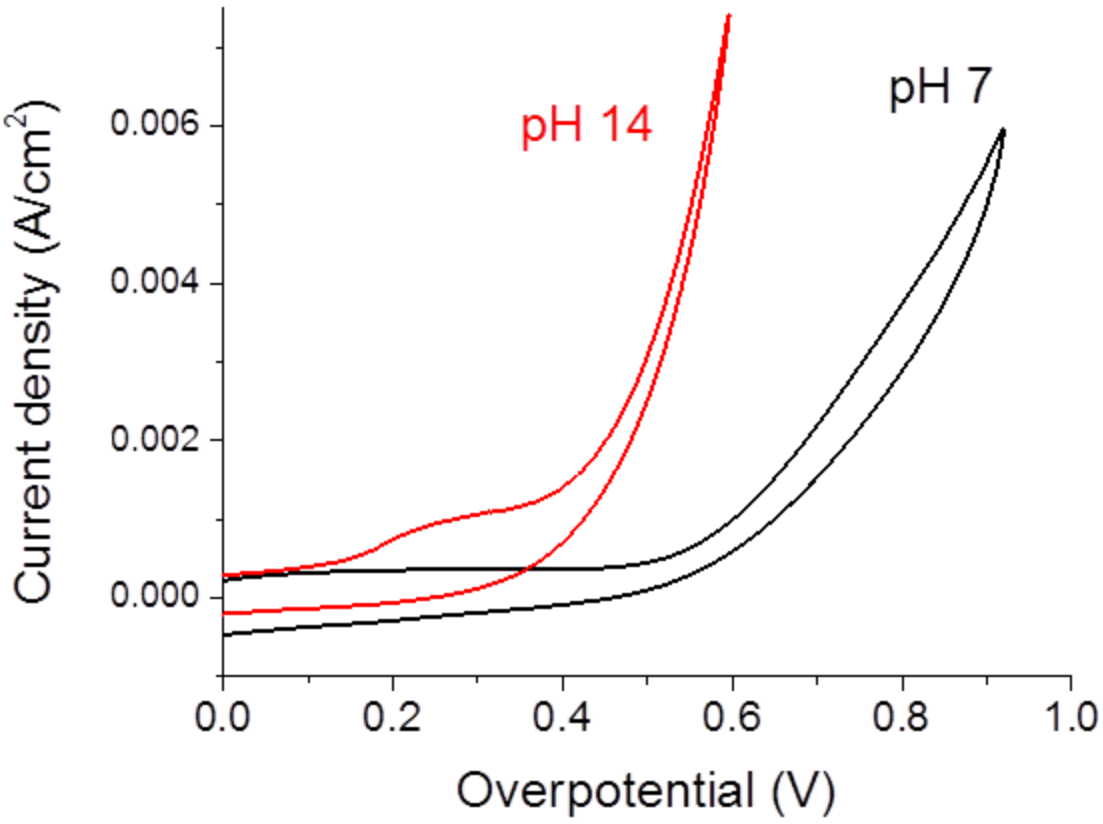

Figure 4.18: Cyclic voltammetry of Mn_3O_4

For our third investigation of corner-shared Mn^{3+}, we pursued comparative studies of crystalline HexBir and TriBir samples which have been previously characterized by our

group in separate reports.[4,25] When compared to manganite under photochemical assay conditions at 250 ppm loading, neither birnessite produces O_2 above baseline (Figure 4.13), consistent with our previous reports.[4,25] Electrochemically, this trend persisted: both birnessites were poor electrocatalysts below 600 mV overpotential in neutral pH (Figure 4.16A and Figure 4.19) and on par with β-MnO_2. Despite our attempts to discern a difference between the two birnessites by electrochemical measurements, neither birnessite could produce 10 mA/cm^2 below 600 mV overpotential, even in alkaline pH. To our knowledge, no layered Mn-oxide achieves this performance, suggesting edge- and face-shared octahedra are not viable catalytic sites.

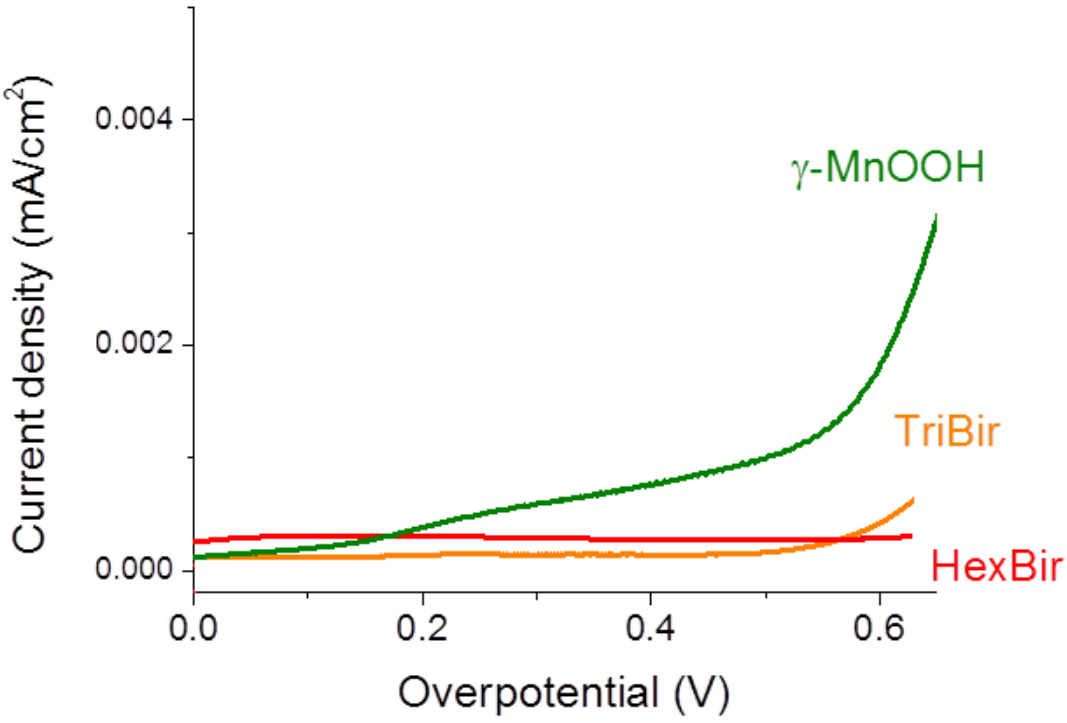

Figure 4.19. Linear voltammograms of birnessites and manganite (0.5 mg/cm^2 loading, pH 7 (1 M phosphate).

The most prominent difference in activity between these birnessites was seen using the photochemical assay and only at high loading to promote O_2 evolution above limit of detection. At ~4.5 fold higher loading (1100 ppm), and following a ~60 second lagtime for both materials, HexBir noticeably produced more O_2 than TriBir normalized to surface area (Figure 4.13). This data thus supports the correlation of corner-sharing Mn^{3+} with activity, and shows that birnessites are more active if Mn^{3+} can be destabilized from the edge-sharing sheets (triclinic type) into the interlayer/surface (hexagonal type). The light-driven system appears to be valuable to demonstrate activity from crystalline birnessite, as several layered materials are known to be active only under illumination.[45,46] While the mechanism of birnessite photoreduction is not well understood, recent data suggests more corner-sharing Mn^{3+} are formed in the process.[47]

Scheme 1 depicts the birnessite/manganite equilibrium.[13] Notably, formation of manganite is known to occur more rapidly on disordered, poorly crystalline layered

materials than rigid, crystalline materials.[17] This property is highlighted in the manganite synthesis procedure described by Suib, et. al, who reported that a poorly crystalline Mn^{4+}-oxide is the product unless Mn^{2+} is added as a final step.[28]

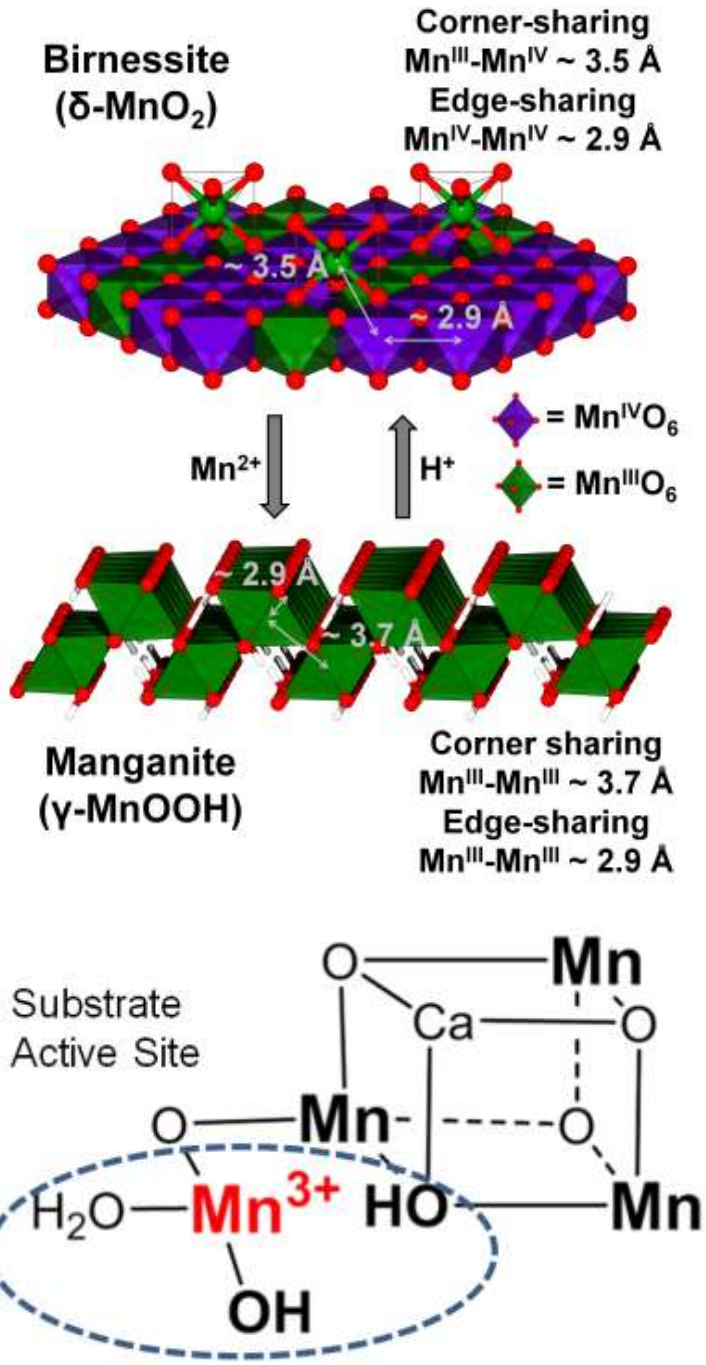

Scheme 1. Depiction of corner-shared Mn^{3+} octahedra: **top**, in hexagonal birnessites, **bottom**, in the S2 state spin=5/2 tautomer of natural photosynthesis.

We envision surface directed, corner-shared Mn^{3+} is significantly more effective than planar Mn at facilitating the binding of water. Studies of HexBir $K_{0.231}Mn^{3+}_{0.077}(Mn^{4+}_{0.885}\ \square_{0.115})O_2 \bullet 0.6\ H_2O$ (□ represents lattice vacancies) by Lanson and coworkers assigned 0.24 (40%) of the formula water units as bound to interlayer (corner-shared) Mn^{3+}, despite being present as only 9% of the total Mn.[48] This assignment is paralleled in Photosystem II. While two possible oxidation state paradigms exist, supporters of *both* assignments have offered the S_2 state as containing a dangler Mn^{3+} in the "closed cubane", spin=5/2 tautomer (Scheme 1).[49,50] This corner shared species contains the only Mn-bound waters in the entire catalyst. Taken in context with the aforementioned results, it is clear that preventing planarization of Mn and making available water coordination sites are two essential properties of viable Mn-based water oxidation catalysts.

4.5 Conclusion

In conclusion, we have elucidated a definitive advantage for corner sharing Mn^{3+} as water oxidation catalytic sites as opposed to edge sharing Mn^{3+} and Mn^{4+} in either coordination. Our data shows that manganite, which consists of corner sharing Mn^{3+} sites over 1x1 tunnel vacancies, has much higher activity than analogous corner sharing Mn^{4+} sites (β-MnO_2). This structural requirement reconciles the description of Mn^{3+} content,[11] layer vacancies,[21] and 3.45 Å Mn-Mn distances[20] previously proposed as activity descriptors in other Mn-oxides. Further, nature's use of only four terminal water ligands (on Ca or Mn^{3+}, Scheme 1 bottom) in conjunction with eight amino acid ligands (on other Mn) highlights an effective strategy to prevent catalyst hydrolysis into poorly active Mn^{4+}-oxides. A successful water oxidation catalyst made from manganese must therefore prevent Mn^{3+} from oxidizing to Mn^{4+} at the substrate water binding site, a seemingly paradoxical finding considering the need to accumulate four holes for O_2 evolution. The simplest way to prevent Mn^{3+} oxidation is by preventing formation of short Mn-O bonds needed to stabilize Mn^{4+}. This structural feature is indeed found in the dangler Mn site.[49,51]

4.6 Acknowledgment

This work was supported by NSF CLP #1213772. We are grateful to NSF DGE0903675 for IGERT fellowships (P.F.S, G.G.). B.J.D., H.W. and J.L. would like to thank the partial support by the U.S. Department of Energy, Office of Basic Energy Sciences, Materials Sciences and Engineering Division through grant DE-FG02-08ER46491 for materials characterization including PXRD, XPS and BET surface area analysis. We thank Dr. Anders B. Laursen for valuable discussions and SEM images, and Karin Calvinho for ICP measurements. The authors declare no competing financial interests.

4.7 References

(1) Yamaguchi, A.; Inuzuka, R.; Takashima, T.; Hayashi, T.; Hashimoto, K.; Nakamura, R. Nat Commun 2014, 5.
(2) Park, J.; Kim, H.; Jin, K.; Lee, B. J.; Park, Y.-S.; Kim, H.; Park, I.; Yang, K. D.; Jeong, H.-Y.; Kim, J.; Hong, K. T.; Jang, H. W.; Kang, K.; Nam, K. T. J. Am. Chem. Soc. 2014, 136, 4201–4211.
(3) Kuo, C.-H.; Mosa, I. M.; Poyraz, A. S.; Biswas, S.; El-Sawy, A. M.; Song, W.; Luo, Z.; Chen, S.-Y.; Rusling, J. F.; He, J.; Suib, S. L. ACS Catal. 2015, 1693–1699.
(4) Robinson, D. M.; Go, Y. B.; Mui, M.; Gardner, G.; Zhang, Z.; Mastrogiovanni, D.; Garfunkel, E.; Li, J.; Greenblatt, M.; Dismukes, G. C. J. Am. Chem. Soc. 2013, 135, 3494–3501.
(5) Gorlin, Y.; Jaramillo, T. F. J. Am. Chem. Soc. 2010, 132, 13612–13614.
(6) Cady, C. W.; Gardner, G.; Maron, Z. O.; Retuerto, M.; Go, Y. B.; Segan, S.; Greenblatt, M.; Dismukes, G. C. ACS Catal. 2015, 3403–3410.
(7) Morita, M.; Iwakura, C.; Tamura, H. Electrochim. Acta 1979, 24, 357–362.
(8) Mattioli, G.; Zaharieva, I.; Dau, H.; Guidoni, L. J. Am. Chem. Soc. 2015, 137, 10254–10267.
(9) McKendry, I. G.; Kondaveeti, S. K.; Shumlas, S. L.; Strongin, D. R.; Zdilla, M. J. Dalt. Trans. 2015, 44, 12981–12984.
(10) Jeong, D.; Jin, K.; Jerng, S. E.; Seo, H.; Kim, D.; Nahm, S. H.; Kim, S. H.; Nam, K. T. ACS Catal. 2015, 5, 4624–4628.
(11) Takashima, T.; Hashimoto, K.; Nakamura, R. J. Am. Chem. Soc. 2012, 134, 1519–1527.
(12) Luo, J.; Zhang, Q.; Suib, S. L. Inorg. Chem. 2000, 39, 741–747.
(13) Elzinga, E. J. Environ. Sci. Technol. 2011, 45, 6366–6372.
(14) Portehault, D.; Cassaignon, S.; Baudrin, E.; Jolivet, J.-P. Cryst. Growth Des. 2010, 10, 2168–2173.
(15) Luo, J.; Huang, A.; Park, S. H.; Suib, S. L.; O'Young, C.-L. Chem. Mater. 1998, 10, 1561–1568.
(16) Lefkowitz, J. P.; Rouff, A. A.; Elzinga, E. J. Environ. Sci. Technol. 2013, 47, 10364–10371.
(17) Elzinga, E. J.; Kustka, A. B. Environ. Sci. Technol. 2015, 49, 4310–4316.
(18) Robinson, D. M.; Go, Y. B.; Greenblatt, M.; Dismukes, G. C. J. Am. Chem. Soc. 2010, 132, 11467–11469.
(19) Kohler, T.; Armbruster, T.; Libowitzky, E. J. Solid State Chem. 1997, 133, 486–500.
(20) Zaharieva, I.; Chernev, P.; Risch, M.; Klingan, K.; Kohlhoff, M.; Fischer, A.; Dau, H. Energy Environ. Sci. 2012, 5, 7081–7089.
(21) Iyer, A.; Del-Pilar, J.; King'ondu, C. K.; Kissel, E.; Garces, H. F.; Huang, H.; El-Sawy, A. M.; Dutta, P. K.; Suib, S. L. J. Phys. Chem. C 2012, 160, 6474–6483.
(22) Wiechen, M.; Zaharieva, I.; Dau, H.; Kurz, P. Chem. Sci. 2012, 3, 2330–2339.
(23) Zaharieva, I.; Najafpour, M. M.; Wiechen, M.; Haumann, M.; Kurz, P.; Dau, H. Energy Environ. Sci. 2011, 4, 2400–2408.
(24) Menezes, P. W.; Indra, A.; Littlewood, P.; Schwarze, M.; Göbel, C.; Schomäcker, R.; Driess, M. ChemSusChem 2014, 7, 2202–2211.

(25) Deibert, B. J.; Zhang, J.; Smith, P. F.; Chapman, K. W.; Rangan, S.; Banerjee, D.; Tan, K.; Wang, H.; Pasquale, N.; Chen, F.; Lee, K.-B.; Dismukes, G. C.; Chabal, Y. J.; Li, J. Chem. Eur. J. DOI: 10.1002/chem.201501930
(26) Pokhrel, R.; Goetz, M. K.; Shaner, S. E.; Wu, X.; Stahl, S. S. J. Am. Chem. Soc. 2015, 137, 8384–8387.
(27) El-Deab, M. S.; Awad, M. I.; Mohammad, A. M.; Ohsaka, T. Electrochem. commun. 2007, 9, 2082–2087.
(28) Crisostomo, V. M. B.; Ngala, J. K.; Alia, S.; Dobley, A.; Morein, C.; Chen, C.-H.; Shen, X.; Suib, S. L. Chem. Mater. 2007, 19, 1832–1839.
(29) Smith, P. F.; Kaplan, C.; Sheats, J. E.; Robinson, D. M.; McCool, N. S.; Mezle, N.; Dismukes, G. C. Inorg. Chem. 2014, 53, 2113–2121.
(30) Morris, N. D.; Suzuki, M.; Mallouk, T. E. J. Phys. Chem. A 2004, 108, 9115–9119.
(31) Ramstedt, M.; Sjöberg, S. Aquat. Geochemistry 2005, 11, 413–431.
(32) Ramstedt, M.; Shchukarev, A. V; Sjöberg, S. Surf. Interface Anal. 2002, 34, 632–636.
(33) Ramstedt, M.; Andersson, B. M.; Shchukarev, A.; Sjöberg, S. Langmuir 2004, 20, 8224–8229.
(34) Bricker, O. Am. Miner. 1965, 50, 1296–1354.
(35) McCrory, C. C. L.; Jung, S.; Peters, J. C.; Jaramillo, T. F. J. Am. Chem. Soc. 2013, 135, 16977–16987.
(36) McCrory, C. C. L.; Jung, S.; Ferrer, I. M.; Chatman, S. M.; Peters, J. C.; Jaramillo, T. F. J. Am. Chem. Soc. 2015, 137, 4347–4357.
(37) Boppana, V. B. R.; Jiao, F. Chem. Commun. 2011, 47, 8973–8975.
(38) Meng, Y.; Song, W.; Huang, H.; Ren, Z.; Chen, S.-Y.; Suib, S. L. J. Am. Chem. Soc. 2014, 136, 11452–11464.
(39) Fekete, M.; Hocking, R. K.; Chang, S. L. Y.; Italiano, C.; Patti, A. F.; Arena, F.; Spiccia, L. Energy Environ. Sci. 2013, 6, 2222–2232.
(40) Ramdohr, P. The Ore Minerals and Their Intergrowths; Pergamon Press Ltd: Oxford, 2013.
(41) Bulavchenko, O. A.; Vinokurov, Z. S.; Afonasenko, T. N.; Tsyrul'nikov, P. G.; Tsybulya, S. V; Saraev, A. A.; Kaichev, V. V Dalt. Trans. 2015, 44, 15499–15507.
(42) Nesbitt, H. W. W.; Banerjee, D. Am. Miner. 1998, 83, 305–315.
(43) Toupin, M.; Brousse, T.; Bélanger, D. Chem. Mater. 2004, 16, 3184–3190.
(44) Ramírez, A.; Hillebrand, P.; Stellmach, D.; May, M. M.; Bogdanoff, P.; Fiechter, S. J. Phys. Chem. C 2014, 118, 14073–14081.
(45) Singh, A.; Hocking, R. K.; Chang, S. L.-Y.; George, B. M.; Fehr, M.; Lips, K.; Schnegg, A.; Spiccia, L. Chem. Mater. 2013, 25, 1098–1108.
(46) Hocking, R. K.; Brimblecombe, R.; Chang, L.-Y.; Singh, A.; Cheah, M. H.; Glover, C.; Casey, W. H.; Spiccia, L. Nat. Chem. 2011, 3, 461–466.
(47) Marafatto, F. F.; Strader, M. L.; Gonzalez-Holguera, J.; Schwartzberg, A.; Gilbert, B.; Peña, J. Proc. Natl. Acad. Sci. 2015, 112 , 4600–4605.
(48) Gaillot, A.-C.; Flot, D.; Drits, V. a.; Manceau, A.; Burghammer, M.; Lanson, B. Chem. Mater. 2003, 15, 4666–4678.
(49) Vinyard, D. J.; Ananyev, G. M.; Dismukes, G. C. Annu. Rev. Biochem. 2013, 82, 577–606.

(50) Krewald, V.; Retegan, M.; Cox, N.; Messinger, J.; Lubitz, W.; DeBeer, S.; Neese, F.; Pantazis, D. a. Chem. Sci. 2015, 6, 1676–1695.
(51) Petrie, S.; Pace, R. J.; Stranger, R. Angew. Chemie 2015, 127, 7226–7230.

Chapter 5 Entropy and Enthalpy Contributions to the Kinetics of Proton Coupled Electron Transfer to the $Mn_4O_4(O_2PPh_2)_6$ Cubane

5.1Abstract

The dependence of rate, entropy of activation, and ($^1H/^2H$) kinetic isotope effect for H-atom transfer from a series of p-substituted phenols to cubane $Mn_4O_4L_6$ ($L=O_2PPh_2$) (**1**) reveals the activation energy to form the transition state is proportional to the phenolic O-H bond dissociation energy. New implications for water oxidation and charge recombination in photosystem II are described.

5.2 Introduction

The interdependence of proton and electron transfer kinetics, termed proton-coupled electron transfer (PCET), is common in chemical and biological redox reactions. This coupling is manifested in kinetics being controlled by the free energy difference and nuclear reorganization barrier between redox reaction partners[1]. A prominent example of PCET occurs in natural photosynthesis, in which water is oxidized by a $CaMn_4O_5$ "heterocubane" cluster (water oxidation complex, WOC) located in photosystem II (PSII). The cluster is capable of breaking four water O-H bonds (119 kcal/mol) via successive or concerted PCET reactions, many of which are believed to involve separate sites for the proton and electron. The $Mn_4O_4(O_2PPh_2)_6$ cubane (**1**) (Scheme 5.1A) is a related model compound that can dehydrogenate C-H, N-H, and O-H bonds and thus is useful for understanding successive PCET reactions[2,3]. Mechanistic studies have shown initial H-atom abstraction to form $Mn_4O_3(OH)(O_2PPh_2)_6$ (**1H**), which was isolated and characterized[4,5]. Depending upon reductant, three additional H equivalents can be removed to form the "butterfly" $Mn_4O_2(O_2PPh_2)_6$ (**2**) and release two water molecules (Scheme 5.1B). The O-H bond dissociation energy (BDE) of **1H** was previously estimated from such studies.

Herein, we have extended this work to examine the reaction kinetics and H/D kinetic isotope effect (KIE) between **1** and a series of para-substituted phenols of known O-H BDEs. The reaction between 1 and phenol has been previously reported and is summarized in Scheme 5.1[5].

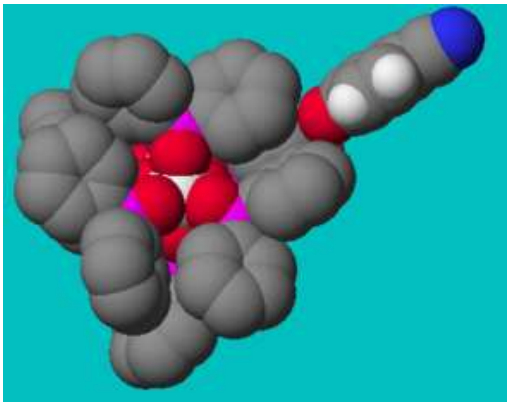

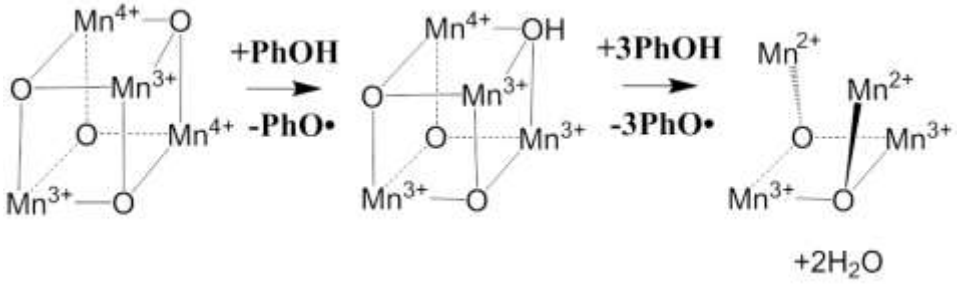

Scheme 5.1: (A, top) Postulated docking configuration of 4-methylphenol to the atomic structure of **1** taken from single crystal Xray diffraction. Image along one of the four body diagonals depicting Mn on top. Red = O, Purple = P, Silver = Mn, Gray = Phenyl ring, Blue = para-substituent. (**B, bottom**) Reactions of the $Mn_4O_4^{6+}$ cubane core with hydrogen atom donors.

5.3Experimental

Materials. $Mn_4O_4(O_2PPh_2)_6$ (**1**) was prepared as described elsewhere[3]. All other materials were of analytical purity from commercial sources and were used as received. Monodeuterated phenols were prepared by exchange using CD_3OD in approximately 500-fold excess in CH_2Cl_2 solution.

Kinetic Measurements. The reactions of phenols with **1** were monitored by UV-Vis spectrophotometry on an HP-8452A spectrophotometer in CH_2Cl_2 solution. Constant temperature was maintained using a Neslab Endocal RTE-5DD circulating water bath. All measurements were made at 25.0 ±0.1ºC unless otherwise stated. The change in the absorbance at 342 nm was monitored. This wavelength reflects the change in concentration of **1** and is located in the center of a region of the spectrum that bleaches upon reaction of phenols with **1**.

Data analysis. All data points represent an average of five separate experimental trials. Initial rates were calculated directly from the initial slopes of the absorbance vs. time traces, yielding (-dA/dt). The pseudo-first order rate constant k_{obs} was determined by fitting the slope from a plot of $\ln(A_t-A_\infty)$ vs. time:

$$\ln(A_t-A_\infty) = -k_{obs}*t + \text{constant}$$

The second order rate constant is obtained by fitting the corresponding equation:

$$K_{obs} = k_2\,[\text{phenol}]$$

5.4 Results and Discussion

The phenoxyl radical product R-PhO● is highly reactive and, depending on R, can further react to give a variety of radical coupling products. For phenol (R=H), this product is commonly biphenoquinone, but for p-substituted phenols, products may not easily be identified[5,6]. In our case, reaction of 1 with excess 4-methylphenol resulted in uniform spectral bleaching (Figure 5.1). Spectral bleaching is fully consistent with proton-coupled reduction of **1,** as previously observed by electrochemical methods[7]. The rate of bleaching is first order in [**1**] (Figure 5.1, inset), and can be fit to integrated first-order kinetics to determine the pseudo-first order constant. A plot of pseudo-first order rate constants vs. concentration of 4-methylphenol gives clean second order kinetics over ten-fold concentration range, R^2= 0.94 (Figure 5.2), and a second order rate constant of 4.80 $(M*s)^{-1}$. Eyring analysis (Figure 5.3) of the temperature dependence of the rate constant (10-30 ºC) gives the activation enthalpy and entropy of reaction ($\Delta H^{\ddagger}$ =2.8 kcal/mol and $\Delta S^{\ddagger}$ =-46 cal/mol*K, respectively). Thus, it follows that the activation energy at 298 K is $\Delta G^{\ddagger}$ = 16.5 kcal/mol.

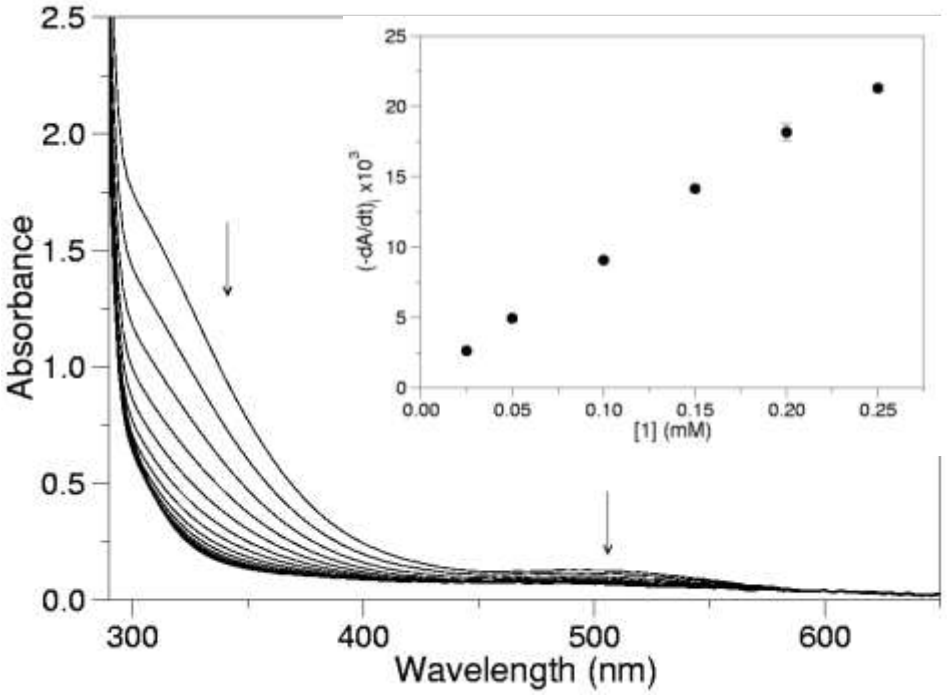

Figure 5.1: Spectral changes observed during the reaction of p-Me-phenol with 1 at 25.0ºC. Conditions: [**1**] = 0.10 mM in CH_2Cl_2; [*p*-Me-phenol] = 3.0 mM; spectra were collected in 20 second intervals. Inset: Initial rate $(-dA/dt)_i$ (at 342 nm) is a linear function of the concentration of **1** (R^2=0.99).

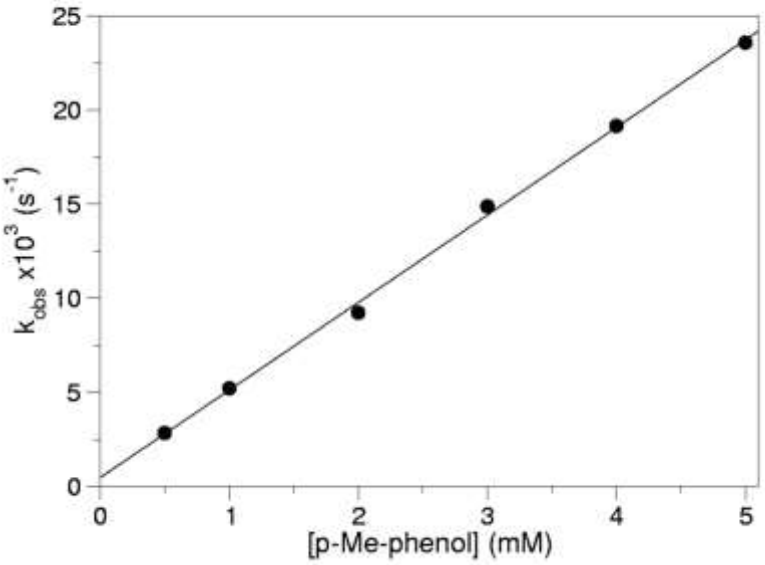

Figure 5.2: Pseudo-first order rate constant kobs as a function of the concentration of p-Me-phenol for the reaction between 1 and p-Me-phenol at 25.0ºC. Conditions: [**1**] = 0.10 mM in CH_2Cl_2; [*p*-Me-phenol] = 0.50-5.0 mM.

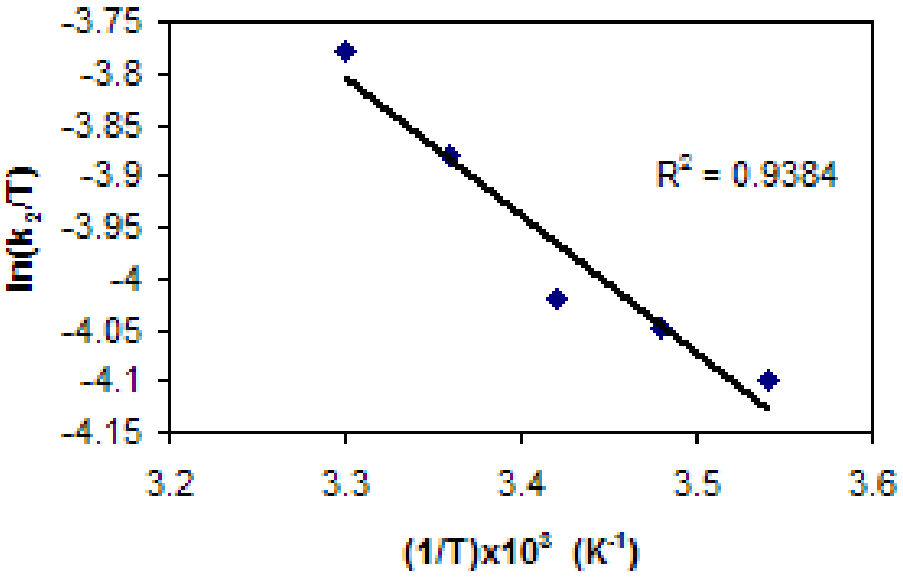

Figure 5.3: Temperature dependence of the reaction between 1 and p-Me-phenol. Conditions: [**1**] = 0.10 mM in CH_2Cl_2; [*p*-Me-phenol] = 3.0 mM.

Extending this workup to other para-substituted phenols (R= Ph, H, CN, tBu, Br), we obtain second order rate constants that cover four orders of magnitude and associated activation energies ($\Delta G^{\ddagger}$) within the range 15.5-20 kcal/mol (Table 5.1). Kinetic isotope effects (k_H/k_D) were measured at 298 K for monodeuterated p-Me and p-CN phenols, obtained by prior exchange in CH_3OD yielding values of 2.0±0.2 and 2.1 ±0.3, respectively. This implies KIE is essentially independent of BDE (Table 5.1).

R	$k, M^{-1}s^{-1}$	k_H/k_D	$\Delta G^{\ddagger a}$	$\Delta G^{o}_{CT}{}^{b}$	$\Delta G^{o}_{PT}{}^{b}$	$\Delta G^{o}_{ET}{}^{b}$	*O-H BDE*[c]
Me	4.80	2.0	16.5	≤4.7	≥21.8	45.4	88.7
H	0.71	n/a	18	≤5.9	≥20.5	47.9	89.8
Ph	27.5	n/a	15.5	≤3.6	≥19.3	42.4	87.6
tBu	6.53	n/a	16.3	≤4.8	≥21.9	45.6	88.7
Br	2.44	n/a	16.9	≤6.8	≥18.3	49.8	90.7
CN	0.004	2.1	20	≤10.3	≥13.9	58.8	94.2

Table 5.1. Rate constants and linear free energy parameters for the reaction of 1 + 4-R-phenol.

a. Experimentally measured, kcal/mol.

b. Calculated from thermochemical cycle, kcal/mol.

c. Phenol O-H bond dissociation energy, ref. [8]

Quantitative analysis shows that proton and electron transfer occur in a concerted mechanism, not successive stepwise pathways, as detailed next. The thermochemical cycle given in Scheme 5.2 depicts the contributions from pKa values[5] and reduction potentials[7] that convert the cubane **1** to its protonated (**1H**$^+$), reduced (**1**$^-$), and hydrogenated (**1H**) products. The reduction potential for **1H**$^+$/**1H** is at least equal that of **1**$^+$/**1**, because **1H**$^+$ quantitatively oxidizes **1** to **1**$^+$ as described previously[9]. The parameters from this cycle are converted to Gibbs energy using eqns (1-3)[10]:

$$\Delta G^{o}_{PT} = 1.37[pK_a(\text{Ph-OH}) - pK_a(\mathbf{1H}^+)] \quad (1)$$

$$\Delta G^{o}_{ET} = 23.06[E^{o}(\text{Ph-OH}\bullet/\text{Ph-OH}) - E^{0}(\mathbf{1/1}^-)] \quad (2)$$

$$\Delta G^{0}_{PCET} = 23.06[E^{o}(\text{Ph-OH}\bullet/\text{Ph-OH}) - E^{o}(\mathbf{1/1}^-)]$$

$$+ 1.37[pKa(\text{Ph-OH}\bullet) - pKa(\mathbf{1H})] \quad (3)$$

The calculated thermodynamic driving force for the first proton transfer from the phenol to **1** (ΔG^{o}_{PT}) is proportional to the difference between the pK_a values of the phenol (ca. 19 for 4-methylphenol)[8] and **1**, which can be protonated only by strong acids. Thus, the first proton transfer from 4-methylphenol to **1** is uphill by at least 1.37*(16) = 21.8 kcal/mol. This thermodynamic barrier is larger than the kinetic activation energy measured experimentally. Likewise, the necessary driving force for initial electron transfer (ΔG^{o}_{ET}) is proportional to the difference in the one-electron reduction potentials. The first electron transfer step from 4-methylphenol ($E_{1/2}$ = 1.865 V vs. SHE)[8] to **1** (-0.105 V vs. SHE) is uphill by 45.4 kcal/mol, which is again larger than the experimental activation energy. For all phenols studied, the measured $\Delta G^{‡}$ is lower than the values expected if either the proton or electron were transferred individually (Table 5.1), with one exception (proton

transfer from 4-CN-phenol, ΔG^{o}_{PT}). This data strongly infers that stepwise PCET does not occur in this system.

Scheme 5.2: Thermochemical cycle for 1.

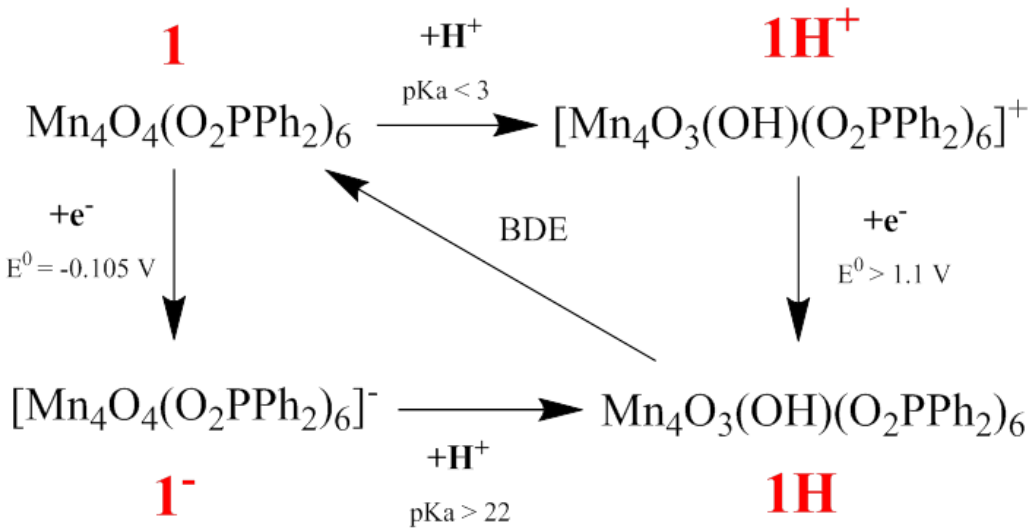

For concerted transfer (ΔG^o_{CT}), the change in free energy is calculated as the sum of two processes- first, electron transfer from 4-methylphenol to **1**, and second, proton transfer from the resulting radical cation to the reduced cube (eqn 3). The latter process has a very negative Gibbs energy, because the 4-methylphenol radical cation (Ph-OH●, pKa = -7.1)[8] transfers a proton to the strongly basic $\mathbf{1}^-$ at least 29 pK units. As a result, ΔG^o_{CT} is much lower than the calculated ΔG^o_{PT} and ΔG^o_{ET} values; CT from 4-methylphenol to **1** is calculated as $\leq$ 45.4-1.37*(29) = 4.7 kcal/mol. For all phenols, we find $\Delta G^o_{CT} <\leq \Delta G^{\ddagger}$. Thus, CT is not only the thermodynamically favored pathway; it is also the *only* pathway with a calculated driving force lower than the measured activation energy. This approach allows an estimation of the O-H BDE of **1H** via eqn (4)[11]. From the reaction with 4-methylphenol:

$$4.7 \leq \Delta G^o_{rxn} = (BDE_{1H} - BDE_{phenol}) - T(\Delta S^o)_{rxn} \qquad (4)$$

$$BDE_{1H} = BDE_{phenol} + \Delta G^o_{rxn} + T\Delta S^o_{rxn} \leq 88.7 + 4.7 + T\Delta S^o_{rxn}$$

Where the subscript rxn denotes the measured reaction:

1 + PhOH → (**1H**●OPh) → **1H** + ●OPh

Ignoring the entropy term, this gives $BDE_{1H} \leq 93.4$ kcal/mol. The highest upper bound obtained in this way is $\leq$ 98.9 kcal/mol (R = CN). The actual BDE is likely lower due to the negative TΔS term (see below). We note that a lower bound can be calculated by adapting the common thermodynamic cycle[5,8,12–14]:

$$BDE = 23.06E_{1/2} + 1.37\ pK_a + 56\ (kcal/mol) \qquad (5)$$

Using $E_{1/2}$(**1**/**1**$^-$) and pKa (**1H**/**1**$^-$) in eqn(5) gives a lower bound BDE ≥ 84 kcal/mol. Combining these results, the homolytic BDE lies in the range of 84-98.9 kcal/mol. The range for heterolytic BDE (**1H** → **1**$^+$ + H$^-$) is likewise determined by adding 23.06($E_{1/2}$(**1**$^+$/**1**))[5], yielding 109.4-124.3 kcal/mol. This range compares to the heterolytic BDE of 122 kcal/mol for $[L_2Mn(\mu\text{-}O)(\mu\text{-}OH)MnL_2]^{3+}$ (L=1,10-phenanthroline)[15,16], which has a higher average Mn oxidation state (3.5 vs. 3.25 in **1H**).

For PCET reactions from a class of similar substrates, Bell-Evans-Polanyi kinetics predict linear correlation between activation energy (proportional to ln(k)) and homolytic bond dissociation energy of the PhO-H bond[10,13,17]. As Figure 5.4 illustrates, this correlation (R^2 = 0.97) is indeed present for all the phenols studied, including the N-H bond of phenothiazine (pzH). This correlation covers seven orders of magnitude and strongly implies that H-atom transfer to **1** proceeds by a similar mechanism from all these H-donors. As expected, linear correlations also exist with the donor reduction potential (R^2 = 0.94) and pK_a (R^2 = 0.80), although neither fits as well as the BDE (Figure 5.5).

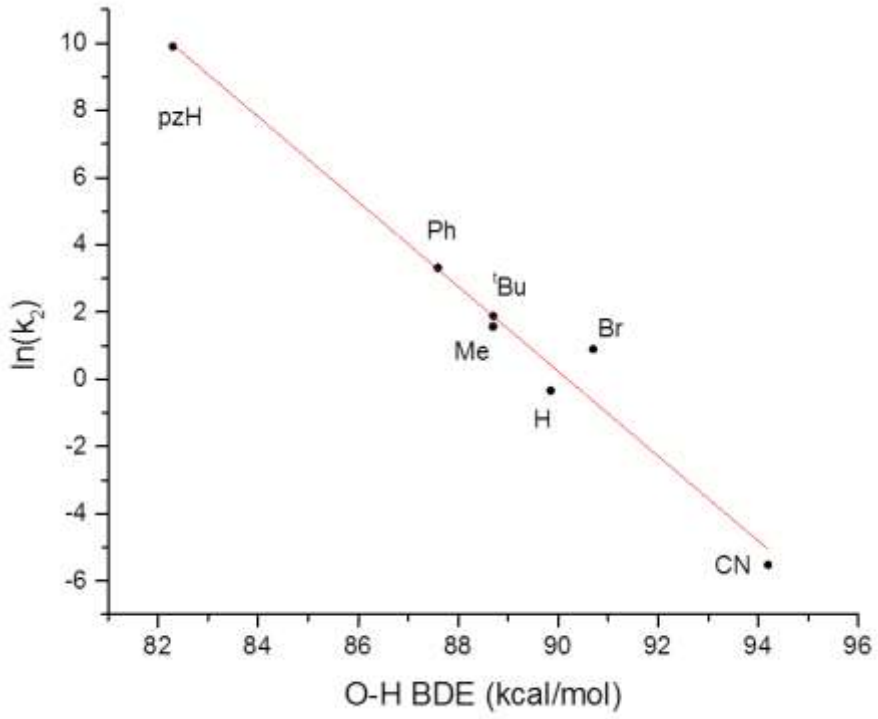

Figure 5.4: Dependence of $\ln(k_2)$ on the homolytic bond dissociation energy.

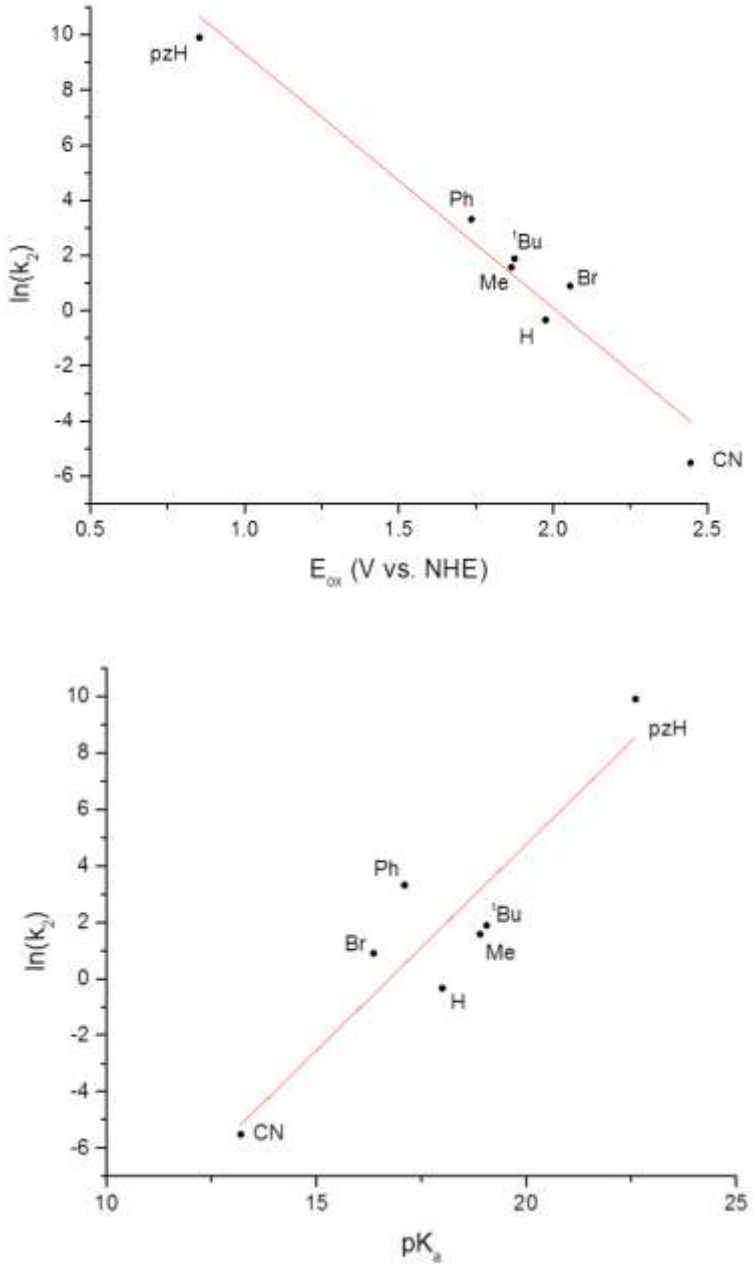

Figure 5.5: Dependence of the ln(k2) on the oxidation potential of the phenol and pKa of the phenolic proton. Conditions: [**1**] = 0.10 mM in CH_2Cl_2; [*p*-X-phenol] = 3.0 mM.

At 298 K, the entropy term is by far the dominant contributor to the activation energy ($-T\Delta S^{\ddagger}$ = 13.7 kcal/mol vs. $\Delta H^{\ddagger}$ = 2.8 kcal/mol for 4-MePhenol), indicating that the transition state is dominated by an increase in order rather than PhO-H bond breaking. This result is rationalized because H-atom transfer occurs via an inner-sphere mechanism; for the phenol to make van der Waals contact with a corner oxo, reordering of the phenyl rings of three phosphinate ligands is required to allow phenol access (Scheme 5.1A), as previously observed for bulky H donors[5]. Additionally, the presence of a small KIE ($k_H/k_D \sim 2.0$) is consistent with this result as it implies little O-H bond cleavage in the transition state[18]. Our data suggest an ordered transition state involving significant reorganization of the Ph ligands of **1** to allow close contact between the phenol and corner oxo of **1** which allows H-atom transfer (Scheme 5.1A illustrates the reactants approaching). This transition state has lower entropy than the separate reactants, likely a result of the additional steric congestion around the $[Mn_4O_4]^{6+}$ core of **1** created by the 12 phenyl rings from six facially bridging $Ph_2PO_2^-$ ligands. The X-ray structure of **1** reveals these rings pack to form a hydrophobic propeller-shaped cavity from three adjacent phenyl rings[19]. These phenyls must move apart to allow the phenol to reach the corner oxygen atoms of **1**.

We note that the linear dependence in Figure 5.5 of $\ln(k_2)$ vs O-H BDE is not in accord with simple Marcus theory which scales as $\log(k_{ET}) \sim (\Delta G)^2$ for adiabatic reactions governed by parabolic potential energy surfaces[10,20]. We find this outcome to be self-consistent with the kinetic model predicting a dominant and relatively constant entropy term contributing to the reduction of **1** by phenols.

The homolytic μ-(O-H) BDE determined herein for **1H** is stronger than for all $[Mn_2O(OH)]^{3+/3+}$ complexes in the literature that have been measured to our knowledge (76-84 kcal/mole, Table 5.2)[13,21,22]. This difference originates from the weaker Mn-O bonding in 1 (longer Mn-O bond lengths, $\Delta R \sim 0.2$ Å) vs the rhombohedral $[Mn_2O_2]^{4+}$ core complexes. This core expansion indicates greater 4s orbital and reduced 3d orbital character from Mn in the HOMO. Consequences for **1** include greater valence electron delocalization (reduced mixed valency Mn^{III}:Mn^{IV}) , higher symmetry (tetrahedral) core, and weaker electrochemical reduction potential (**1/1**$^-$) relative to comparable $[Mn_2O_2]^{4+}$ core complexes. The reduction of **1** involves loss of delocalization of the two highest valence electrons in the HOMO of the symmetrical core. Nature's choice of calcium in the $CaMn_4O_5$ core of Photosystem II may serve to suppress valence delocalization, in light of a recent report indicating that a $CaMn_3O_4$ heterocubane is more easily oxidized (has lower reduction potential) than the Mn_4O_4 core in the same ligand set[23].

Table 5.2. Comparison of μ-O-H BDE's for Mn complexes

Species	*Mn ox. state*	*O-H BDE*	*Ref.*
1H	Mn_4(3III,IV)	84-99	This work
$(Mn_2(L\text{-}X)_2(\mu\text{-}O)(\mu\text{-}OH))^{+a}$	Mn_2(III,IV)	76-79	12
$(Mn_2(\mu\text{-}O)(\mu\text{-}OH)(bpy)_4)^{3+b}$	Mn_2(2III)	84	12,22
$(Mn_2(\mu\text{-}O)(\mu\text{-}OH)(phen)_4)^{3+c}$	Mn_2(2III)	79	13
$(Mn_2(\mu\text{-}O)(\mu\text{-}OH)(bispicen)_2)^{3+d}$	Mn_2(2III)	76	31

a. L-X = 2-hydroxy-1,3-bis(3,5-X_2-salicylideneamino)propane (X= Cl, H or tBu)

b. Bpy= 2,2' bipyridine

c. Phen= 1,10-phenanthroline

d. Bispicen= N,N'-bis[2-methyl(pyridyl)ethane-1,2-diamine]

5.5 Conclusion

The mechanism responsible for controlling the rate of hydrogenation of the cubane **1** by a range of phenol derivatives has been examined by kinetics and KIE covering seven orders of magnitude in rate constant. The free energy barrier controlling the rate of this bimolecular reaction is composed of two terms: mainly an entropy penalty attributed to formation of the reactive complex upon insertion of the phenol between the geared rings of the diphenylphosphinate ligands (Scheme 5.1), and, by a smaller enthalpy term after forming the reactive complex that scales linearly with the O-H bond dissociation energy. The small BDE-independent KIE observed is consistent with this picture of the reaction coordinate. A small KIE is observed also for the various S-state transitions in PSII-WOC[24], which are likewise viewed as PCET processes in the early S-state transitions[4,25]. The O-H bond of water (119 kcal/mol) is substantially lowered by complexation as a bridging hydroxo between manganese atoms, considerably more so for di-μ-OH than for tri-μ-OH sites. These results show that the stronger tri-μ-OH bond in **1H** conserves a larger fraction of the available free energy of the phenol O-H bond, but at the expense of a much slower forward rate. As a result the reverse PCET step becomes important and this has important implications for the functioning of the PSII-WOC in photosynthesis. Indeed, a number of papers have reported reverse electron transfer (PCET) between the WOC and $Y_Z^{\bullet}$ from low temperature trapped S_i states, using infrared light absorbed by the Mn cluster to overcome activation barriers[26]. Hence, the state energy difference between these states is relatively small.

Scheme 5.3: The environment surrounding the tyrosine oxidant in Photosystem II[27].

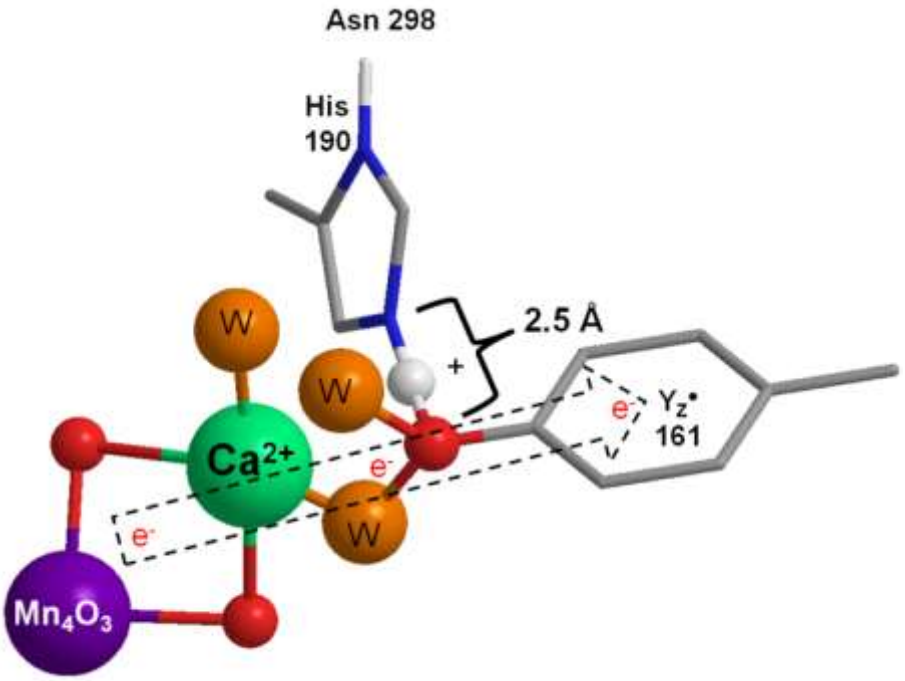

Scheme 5.3 shows the environment of D_1-tyrosine161 (Y_Z-OH) in photosystem II, derived from the 1.9Å X-ray structure[27]. With an O-H BDE of 86.5 kcal/mol[28] (E^o = 1.21 V)[29], $Y_Z^\bullet$ can oxidize the $CaMn_4O_5$ (WOC) when H^+ evolution is permitted. This reaction is blocked (reversed) if protons derived from water oxidation accumulate within the WOC[30]. The present work indicates that the rate of the analogous PCET reaction between **1** and PhOH in solution is controlled both entropically by attainment of a close encounter complex, **1H●**OPh, and enthalpically by the relative strengths of their O-H bonds. Oxygenic photosynthesis relies upon both strategies for creating selective oxidation of the WOC by specific associations of Y_Z-OH with its surroundings. As shown in Scheme 3, electrostatic activation of Y_Z-OH/$Y_Z^\bullet(H^+)$ is achieved by prevention of H^+ release via strong H-bonding to D_1His190 (denoted here by (H^+)), and by electrostatic polarization from coordinated Ca^{2+}. These charges help create both the high oxidation potential of Y_Z-OH/$Y_Z^\bullet(H^+)$ and provide a positive electrical potential gradient from $Y_Z^\bullet(H^+)(Ca^{2+})$ to the Mn_4O_5 subcluster that facilitates forward electron transfer (S-state transitions):

$$S_iY_Z^\bullet(H^+) \leftrightarrow S_{i+1}(+)Y_ZOH \rightarrow S_{i+1}Y_ZOH + H^+$$

Importantly, the reverse reaction is slowed greatly by proton transfer from (H^+)His190 that traps the electron, yielding neutral Y_ZOH. This PCET function of $Y_Z^\bullet(H^+)$His190 is often overlooked but is a critical function, as it keeps the site of oxidation within the Mn_4O_5 subcluster, $(S_{i+1})(+)$, rather than on $Y_Z^\bullet(H^+)$. This trapping slows the charge recombination reactions with the terminal acceptors (plastosemiquinones) Q_A^- and Q_B^- located in PSII[26]. The $Y_Z^\bullet(H^+)$His190 molecular diad is analogous to a pn-diode, designed foremost to prevent reverse electron flow and keep the accumulated holes in the Mn_4O_5 subcluster where O_2 evolution can be catalyzed.

5.6 Acknowledgments

This work was supported by the National Science Foundation (CLP-CHE1213772), an NSF IGERT fellowship (P.F.S.), and an NSF REU fellowship (J.D.).

5.7 References

1. S. Hammes-Schiffer, *Energy Environ. Sci.*, 2012, **5**, 7696–7703.
2. W. F. Ruettinger and G. C. Dismukes, *Inorg. Chem.*, 2000, **39**, 1021–1027.
3. T. G. Carrell, S. Cohen, and G. C. Dismukes, *J. Mol. Catal. A Chem.*, 2002, **187**, 3–15.
4. M. Maneiro, W. F. Ruettinger, E. Bourles, G. L. McLendon, and G. C. Dismukes, *Proc. Natl. Acad. Sci. U. S. A.*, 2003, **100**, 3707–3712.
5. T. G. Carrell, E. Bourles, M. Lin, and G. C. Dismukes, *Inorg. Chem.*, 2003, **42**, 2849–2858.
6. A. Al-Ajlouni, A. Bakac, and J. H. Espenson, *Inorg. Chem.*, 1993, **32**, 5792–5796.
7. R. Brimblecombe, A. M. Bond, G. C. Dismukes, G. F. Swiegers, and L. Spiccia, *Phys. Chem. Chem. Phys.*, 2009, **11**, 6441–6449.
8. We adopt the BDE's as determined from the thermodynamic cycle in: F. G. Bordwell and J. Cheng, *J. Am. Chem. Soc.*, 1991, **113**, 1736–1743. These solution-phase values match experimental gas-phase literature to ±3 kcal/mol, see Bordwell, Cheng and Harrelson, J. Am. Chem. Soc, 1988, 110, 1229-1231
9. W. F. Ruettinger, D. M. Ho, and G. C. Dismukes, *Inorg. Chem.*, 1999, **38**, 1036–1037.
10. J. M. Mayer, *Annu. Rev. Phys. Chem.*, 2004, **55**, 363–390.
11. G. Yin, A. M. Danby, D. Kitko, J. D. Carter, W. M. Scheper, and D. H. Busch, *J. Am. Chem. Soc.*, 2008, **130**, 16245–16253.
12. M. J. Baldwin and V. L. Pecoraro, *J. Am. Chem. Soc.*, 1996, **118**, 11325–11326.
13. K. Wang and J. M. Mayer, *J. Am. Chem. Soc.*, 1997, **119**, 1470–1471.
14. V. D. Parker, K. L. Handoo, F. Roness, and M. Tilset, *J. Am. Chem. Soc.*, 1991, **113**, 7493–7498.
15. M. A. Lockwood, K. Wang, and J. M. Mayer, *J. Am. Chem. Soc.*, 1999, **121**, 11894–11895.
16. A. S. Larsen, K. Wang, M. A. Lockwood, G. L. Rice, T.-J. Won, S. Lovell, M. Sadílek, F. Tureček, and J. M. Mayer, *J. Am. Chem. Soc.*, 2002, **124**, 10112–10123.
17. J. P. Roth and J. M. Mayer, *Inorg. Chem.*, 1999, **38**, 2760–2761.
18. A. Hazra, A. V Soudackov, and S. Hammes-Schiffer, *J. Phys. Chem. Lett.*, 2010, **2**, 36–40.
19. W. F. Ruettinger, C. Campana, and G. C. Dismukes, *J. Am. Chem. Soc.*, 1997, **119**, 6670–6671.
20. R. A. Marcus and N. Sutin, *Biochim. Biophys. Acta - Rev. Bioenerg.*, 1985, **811**, 265–322.
21. M. T. Caudle and V. L. Pecoraro, *J. Am. Chem. Soc.*, 1997, **119**, 3415–3416.
22. H. H. Thorp, J. E. Sarneski, G. W. Brudvig, and R. H. Crabtree, *J. Am. Chem. Soc.*, 1989, **111**, 9249–9250.
23. J. S. Kanady, E. Y. Tsiu, M. W. Day, and T. Agapie, *Science (80-.).*, 2011, **333**.
24. M. Karge, K.-D. Irrgang, and G. Renger, *Biochemistry*, 1997, **36**, 8904–8913.
25. H. Kühne and G. W. Brudvig, *J. Phys. Chem. B*, 2002, **106**, 8189–8196.
26. N. Ioannidis, G. Zahariou, and V. Petrouleas, *Biochemistry*, 2008, **47**, 6292–6300.
27. Y. Umena, K. Kawakami, J.-R. Shen, and N. Kamiya, *Nature*, 2011, **473**, 55–60.

28. C. Tommos, C. W. Hoganson, M. Di Valentin, N. Lydakis-Simantiris, P. Dorlet, K. Westphal, H.-A. Chu, J. McCracken, and G. T. Babcock, *Curr. Opin. Chem. Biol.*, 1998, **2**, 244–252.
29. M. Grabolle and H. Dau, *Biochim. Biophys. Acta - Bioenerg.*, 2005, **1708**, 209–218.
30. D. J. Vinyard, G. M. Ananyev, and G. C. Dismukes, *Annu. Rev. Biochem.*, 2013, **82**, 577–606.
31 Singhal, G.S. et. al. "Concepts in photobiology: Photosynthesis and Photomorphogenesis". 1999, Narosa Publishing House, New Delhi India.